ADA026346

# FINAL REPORT

# MAGNETIC FIELD ANNIHILATION

# OF
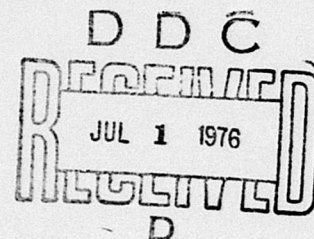
# IMPULSIVE CURRENT SHEETS

March 31, 1976

by

C. L. Dailey, H. A. Davis, and R. H. Lovberg

Prepared for
Air Force Office of Scientific Research
Bolling Air Force Base (Bldg. 410)
Washington D.C. 20332

Contract No. F44620-71-C-0031

DDC

RECEIVED
JUL 1 1976
D.

**TRW.**
SYSTEMS GROUP

ONE SPACE PARK · REDONDO BEACH · CALIFORNIA

Conditions of Reproduction

Reproduction, translation, publication, use and disposal
in whole or in part by or for the United States Govern-
ment is permitted.

18 AFOSR          19 TR-76-0698

9

# FINAL REPORT

# MAGNETIC FIELD ANNIHILATION

# OF

# IMPULSIVE CURRENT SHEETS.

March 31, 1976

by

10 C. L. Dailey, H. A. Davis, and R. H. Lovberg

11 31 Mar 76          12 102p.

Prepared for
Air Force Office of Scientific Research
Bolling Air Force Base (Bldg. 410)
Washington D.C. 20332

15

Contract No. F44620-71-C-0031

DDC
RECEIVED
JUL 1 1976
D

16 AF-9752          17 975202

**TRW.**
SYSTEMS GROUP

ONE SPACE PARK • REDONDO BEACH • CALIFORNIA

354 595

| REPORT DOCUMENTATION PAGE | | READ INSTRUCTIONS BEFORE COMPLETING FORM |
|---|---|---|
| 1. REPORT NUMBER | 2 GOVT ACCESSION NO | 3 RECIPIENT'S CATALOG NUMBER |
| 4. TITLE (and Subtitle)<br><br>MAGNETIC FIELD ANNIHILATION OF IMPULSIVE CURRENT SHEET | | 5. TYPE OF REPORT & PERIOD COVERED<br>FINAL |
| | | 6. PERFORMING ORG. REPORT NUMBER |
| 7. AUTHOR(s)<br>C L DAILEY<br>H A DAVIS<br>R H LOVBERG | | 8. CONTRACT OR GRANT NUMBER(s)<br><br>F44620-71-C-0031 |
| 9. PERFORMING ORGANIZATION NAME AND ADDRESS<br>TRW SPACE AND DEFENSE SYSTEMS GROUP<br>ONE SPACE PARK<br>REDONDO BEACH, CALIFORINA    90278 | | 10. PROGRAM ELEMENT, PROJECT, TASK AREA & WORK UNIT NUMBERS<br>681308<br>9752-02<br>61102F |
| 11. CONTROLLING OFFICE NAME AND ADDRESS<br>AIR FORCE OFFICE OF SCIENTIFIC RESEARCH/NA<br>BUILDING 410<br>BOLLING AIR FORCE BASE, D C    20332 | | 12. REPORT DATE<br>March 1976 |
| | | 13. NUMBER OF PAGES<br>99 |
| 14. MONITORING AGENCY NAME & ADDRESS(if different from Controlling Office) | | 15. SECURITY CLASS. (of this report)<br><br>UNCLASSIFIED |
| | | 15a. DECLASSIFICATION/DOWNGRADING SCHEDULE |

16. DISTRIBUTION STATEMENT (of this Report)

Approved for public release; distribution unlimited.

17. DISTRIBUTION STATEMENT (of the abstract entered in Block 20, if different from Report)

18. SUPPLEMENTARY NOTES

19. KEY WORDS (Continue on reverse side if necessary and identify by block number)

plasma generator
plasma accelerators
pulsed plasma thruster
magnetic field annihilation accelerator
impulsive accelerated plasmas

electric propulsion
space propulsion
satellite positioning and maneuvering

20. ABSTRACT (Continue on reverse side if necessary and identify by block number)
The acceleration mechanism has been studied experimentally in several plasma accelerators which have utilized the collision of a pair of oppositely moving current sheets to set up a plasma/field configuration in which magnetic field energy is converted to plasma energy by the annihilation of antiparallel magnetic fields. Two 40 cm diameter, planar, spiral coils were used to drive the plasma by an impulsive, inductive, discharge for the initial experiments. Detailed magnetic field mapping of the plasma volume during the discharge measurement of electric fields and current density and spectroscopic studies

incuding radial velocity measurement by Doppler shift showed conclusively that no wave mechanism occured in this accelerator in which magnetic field energy was converted to plasma kinetic energy. Magnetic field annihilation was an effective means for driving the argon plasma current after collision producing an 18-fold ion density increase and plasma conductivities as high as $2 \times 10^4$ per M at an electron temperature of about 5 ev. Acceleration efficiency was poor because of the relatively weak orthogonal magnetic field in the high current density region of the current sheet. Attemps to enhance this field component by altering the coil configuration through the use of adjustable coils having parallel wires in flat rectangular surfaces were not successful because of the slow rate of duffusion of the field into the highly conductive current sheet. The use of a strong bias field applied prior to the discharge in this accelerator was successful. Subsequent attempts to apply this principle in a coaxial configuration did not succeed because of strong currents induced in the shield rings that were required to decouple the bias and drive coils. This problem was not encountered in the rectangular geometry because the coils were orthogonal and did not require decoupling shields. This study showed that field annihilation is an effective technique for inductively driving plasma current but that acceleration by self-fields alone cannot be efficient. In addition, the use of bias fields to enhance the acceleration force is not feasible in a coaxial configuration.

## FOREWORD

CONTENTS

# ILLUSTRATIONS

ILLUSTRATIONS (Continued)

ILLUSTRATIONS (Continued)

# ILLUSTRATIONS (Continued)

INTRODUCTION

## 1.1 RELEVANCE TO AIR FORCE NEEDS

Low total impulse requirements for Air Force satellites are presently provided by small monopropellant rocket engines and resisto-jets. The growth in total impulse capability needed for the near future is being met by improving the useful lifetime of these engines. However, future satellites requiring much larger total impulse, either for attitude control and station keeping for long periods or for larger impulse maneuvers, such as orbit repositioning, will require the high specific impulse available with electric propulsion to avoid the unacceptable increases in propellant mass of the lower $I_{sp}$ chemical thrusters. Development of the pulsed ablative, solid propellant thruster and the colloid thruster is proceeding for the relatively low impulse stationkeeping missions. To perform orbit repositioning with lighter weight than the chemical systems now in use, and to provide the capability for future requirements of multiple orbit shift maneuvers, a compact, lightweight, reliable electric thruster is needed. A pulsed electromagnetic thruster employing a strong bias magnetic field is an attractive candidate for meeting this requirement with high efficiency.

## 1.2 COMPARISON OF ELECTRIC THRUSTERS

The performance of several nonthermal types of electric thrusters capable of greater than 1000 seconds $I_{sp}$ is summarized in Figure 1. The electrostatic types include the colloid and ion thrusters. [1,2] The electromagnetic types include the steady flow MPD arc thruster [3] and three pulsed types. These are the coaxial thruster using injected gas propellant, [4] the ablative Teflon thruster [5,6] and the pulsed inductive thruster. [7] The latter device is the only plasma thruster that does not use electrodes; the pulsed plasma current is driven inductively and flows in a closed circular path.

It is interesting that the performance data for all of the thrusters, except the colloid engine, group fairly well around a straight line passing through the origin. Furthermore, except for the low value of the
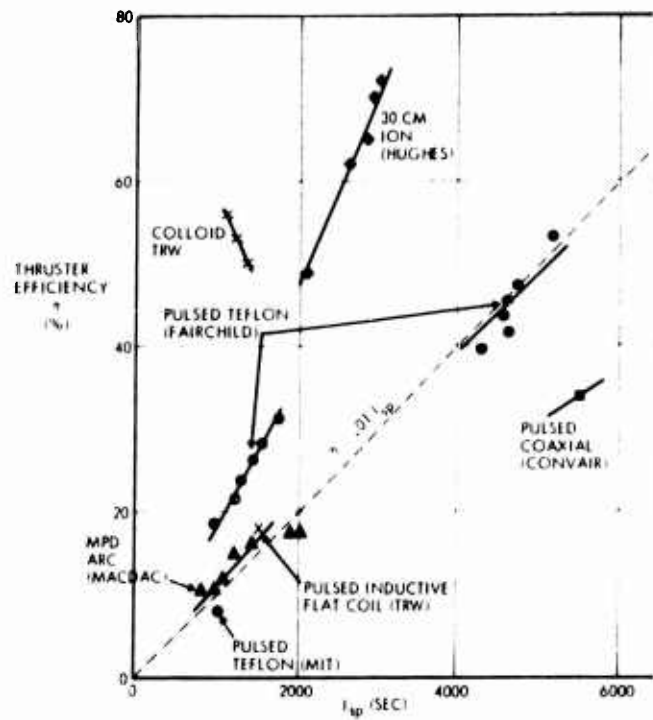
Figure 1. $\eta$ Versus $l_{sp}$ for Several High $I_{sp}$
Electric Thrusters

Convair coaxial device and the high values of one of the Fairchild Teflon thrusters, all of the plasma thrusters have an efficiency at any $I_{sp}$ that is about 1/100 of the $I_{sp}$. The slope of $\eta$ versus $I_{sp}$ is a little more than twice this value for the ion engine while the colloid thruster, at 1100 seconds $I_{sp}$, has five times this slope.

The practical importance of the ratio $\eta/I_{sp}$ is that it is proportional to the thrust per unit power. If $\dot{m}$ is the rate of mass flow leaving a thruster, then $1/2\,\dot{m}\,(g\,I_{sp})^2$ is the corresponding rate of beam kinetic energy, where the effective (thrust producing) velocity is $g\,I_{sp}$. The total power into the thruster is therefore

$$\text{Power} = \frac{1/2\,\dot{m}\,(g\,I_{sp})^2}{\eta}$$

or, since the thrust is

$$T = \dot{m}\,g\,I_{sp}$$

2

$$\frac{T}{power} = \frac{2}{g}\left(\frac{\eta}{I_{sp}}\right)$$

and the thrust available from a fixed power source increases directly
with $\eta/I_{sp}$.

For stationkeeping of present satellites, the thrust available from
the spacecraft power is of greater importance than the propellant con-
sumption which is considerably less than that for competitive chemical
thruster stationkeeping systems. The ion engine produces about half the
thrust of the colloid engine from the same amount of power but it is
capable of operating at both higher power levels and higher specific
impulse values. It is therefore a possible candidate for future space-
craft missions requiring higher power than is now available and larger
total impulse than the present stationkeeping requirements. Its principal
disadvantages are: (1) possible spacecraft contamination from the mer-
cury, or cesium, propellant, (2) large size relative to chemical or
plasma thrusters, and (3) complex power conditioning.

The motivation for the present plasma acceleration study has been
to demonstrate the feasibility of developing large thrust levels at high $I_{sp}$,
with a ratio of $\eta/I_{sp}$ comparable to the ion engine, with a noncontaminat-
ing gaseous propellant and with a relatively simple and compact power
conditioner, propellant system and thruster. An attractive system con-
cept is that it may be possible to operate the thruster on gaseous com-
bustion products obtained from an on-board chemical rocket propellant
system. Other attractive features of pulsed plasma propulsion systems
that are inherent in the pulse mode are the thrust variability, accurate
control of small impulse bits and accelerated testing of components at
high pulse rates.

The practical constraint of small physical size and weight and
low average power level limit the scope of accelerator possibilities,
especially the scale of the devices. The TRW thruster indicated in
Figure 1 was 12 inches in diameter and this was thought to be an upper
limit. The present investigation was undertaken in an effort to find a
more efficient acceleration mechanism than the pressure of a magnetic
field confined by the diamagnetic effect of a plasma current sheet.

3

It was hoped that acceleration by some form of magnetic field annihilation in the interaction in the collision of two current sheets might serve this purpose.

This report describes the results of a 5-year study of impulsive plasma acceleration with several devices that have used some form of magnetic field annihilation to produce the acceleration force.

# SECTION II
# BACKGROUND

The accelerator circuits used in all of the impulsive plasma accelerators investigated in this program have been inductively coupled to the current carried by the plasma. In these devices, charge stored at high voltage in an energy storage capacitor is conducted through a coil by closing a spark gap switch. During the discharge period of a few microseconds, the rapidly changing current in the coil induces an oppositely directed current in the plasma which is physically located as close as possible to the accelerator coil. The repulsive force between the two currents accelerates the plasma away from the accelerator coil. When two coils of this type are used, they can be arranged so that the magnetic fields in the individually accelerated current sheets are anti-parallel. Consequently the magnetic fields diffusing into the composite current sheet after collision are annihilated, giving up their energy to plasma heating and acceleration.

An earlier study of impulsive acceleration in an inductive device had been done using a single flat spiral coil that made one or two turns around the coil axis. By using many closely spaced wires the accelerator current approximated a uniform disc of current so that a sheet of nearly constant current density was induced in the plasma. The rising magnetic field surrounding the accelerator coil was prevented from expanding away from that coil by the highly diamagnetic plasma current sheet so that the resulting magnetic pressure was effective in accelerating the plasma. The acceleration mechanism in this type of accelerator was investigated in static fill operation by means of optical diagnostics and miniature probes which measured the plasma current density and electric and magnetic fields. It was shown that the plasma current was purely azimuthal and was carried predominantly by electrons.[8] The axial electromagnetic body force associated with this current, which provided the acceleration impulse, was balanced by a combination of electron pressure gradient and an axial charge separation electric field. Toward the front of the current sheet the negative electron pressure gradient represented a positive acceleration force acting to accelerate

the electrons ahead of the current sheet.  To preserve neutrality of the plasma, a charge separation electric field developed which transferred the pressure gradient force to the ions.  At the rear of the current sheet this effect was reversed but deceleration of the ions was prevented by the electromagnetic body force on the current carrying electrons. Toward the center of the current sheet the pressure gradient force was small and the more familiar situation was encountered where the body force on the electrons was transferred to the ions by the charge separation electric field.  The overall axial impulse imparted to the plasma was that produced by the electromagnetic force alone while the electron pressure gradient forces served only to distribute the impulse through the current sheet differently from the body force distribution.  This detailed knowledge of the current sheet structure influenced the selection of the two flat spiral coils for the first field annihilation accelerator. Also this configuration provided good accessibility of the plasma volume for optical and probe diagnostic measurements.

## SECTION III

## SELF-FIELD ACCELERATOR EXPERIMENTS

In a self-field accelerator the magnetic field that couples with the
plasma current to produce acceleration arises solely from the circuit
and plasma currents. These fields develop rapidly in a pulsed accelera-
tor, providing the local electric fields that drive the plasma current.
Thus this current is related to the rate of change of magnetic field.
Since the local acceleration force is the product of this rate of change
with the total magnetic field at any point, the local body force is related
to the local rate of change of magnetic pressure. This had not been found
to be large enough for efficient acceleration in the single flat spiral coil
accelerator and it was hoped that a significant improvement would result
from the two coil experiments.

A wave mechanism for conversion of magnetic field energy to
plasma kinetic energy was described theoretically by Petschek[9] and
subsequent experimental work by Bratenahl and Yeates,[10] particularly
schlieren photographs of the accelerated plasma, Figure 2, appeared to
confirm the theoretical model. Bratenahl's accelerator used two side-
by-side inverse Z-pinch discharges to produce two cylindrical sheets of
outward moving plasma. After collision of these sheets, the plasma and
field geometry resembled that depicted in Figure 3, which is reproduced
from Reference 9. The neutral line at $y = 0$ in Figure 3, is midway
between the axes of the inverse pinches  For the two flat spiral coil
accelerator, the neutral line is a circle at about 80% of the maximum
coil radius and the region outside of that radius also approximates
Petscheck's field configuration. The inner region is a shock preheated
$\theta$-pinch. This is illustrated in Figures 4 and 5 which show the accelera-
ted current sheets before collision and the field annihilation configuration
that developes after collision.

The second magnetic field annihilation self-field accelerator used
two flat sheets of parallel coil wires in place of the flat spiral coils.
Both of these self-field accelerators are described below.

7
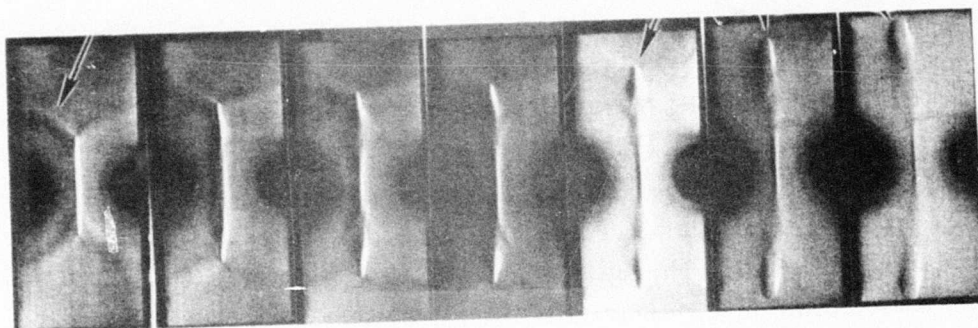
Figure 2. Schlieren Photographs of Argon Shock Collision in
Bratenahl's Double Inverse Pinch (Dark circles are
current rods spaced 10 cm apart)
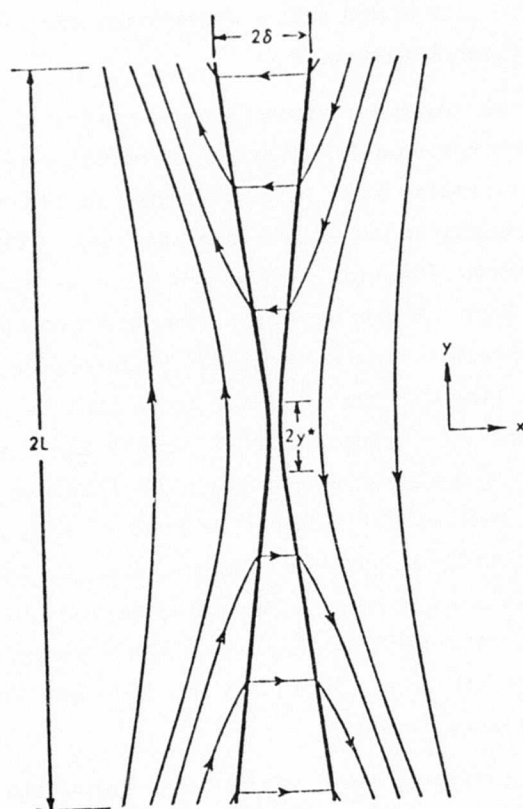


Figure 3. Petschek's Magnetic Field
Annihilation Configuration
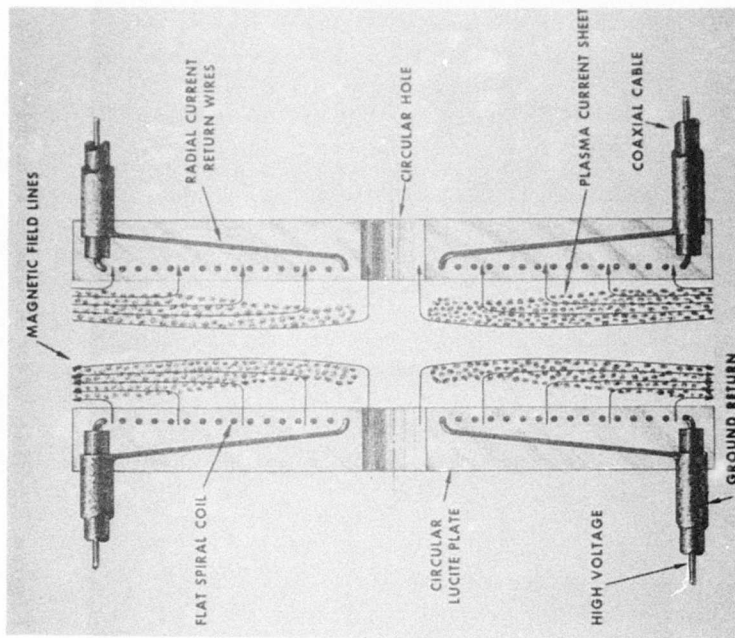
Figure 5. Magnetic Fields and Current Sheets During Field Annihilation
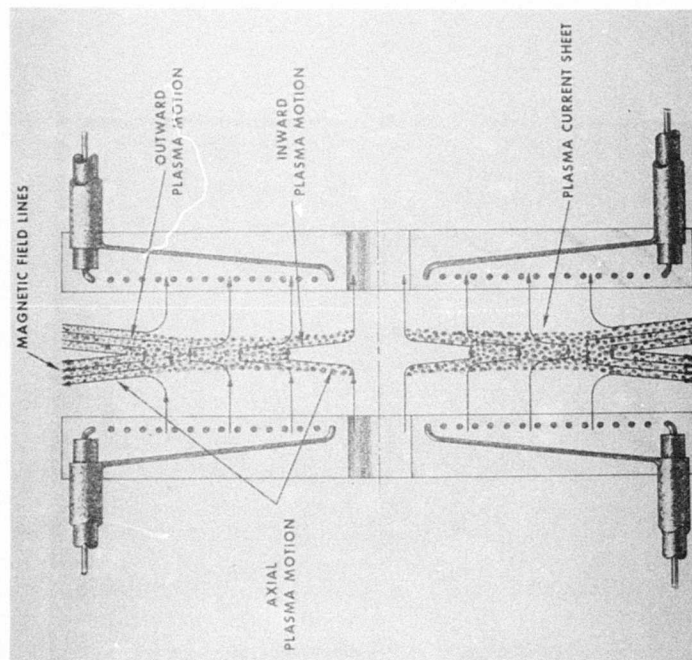


Figure 4. Magnetic Fields and Current Sheets Before Collision

Figure 7. Side View of Coil Assembly Mounted Above Capacitor Bank



Figure 6. Front View of One of the Accelerator Coils

## 3.1 FLAT SPIRAL COIL FIELD ANNIHILATION ACCELERATOR

The accelerator employed two 40 cm diameter flat spiral coils facing each other and spaced closely enough that each coil was inductively coupled to the plasma current at any location in the space between the coils. Each coil comprised 24, one-turn sprirals of No. 14 copper wire extending from an OD of 40 cm to an ID of 10 cm. The wires were returned radially from the inner edge of the spiral to the outer edge where connections were made to 2 meter long RG8-U coaxial cables that separated the coils from the capacitor bank. The bank consisted of six, 4.5 μf capacitors with a separate spark gap connected to each capacitor.

Figure 6 is a front view of one of the coils showing the spiral wires on the front surface and radial wires on the back side which are located 2 inches behind the spiral wires. The coil wires were covered with two 10 mil sheets of Mylar and a 1/16 inch thick annular glass disc with a 7.5 cm diameter hole at the center. The axial distance between the two glass covers was 3.62 cm, or about 9% of the coil diameter.

The coils were mounted in a small vacuum chamber. They were inserted through circular holes in square Lucite side plates as shown in Figure 6. These plates rested against an open steel framework with solid upper and lower steel plates and glass windows supported on O-ring seals on the sides. A side view of the assembly is shown in Figure 7. The glass covers are shown extending beyond the coil structure in this figure. They were later replaced by covers having the same OD as the coil.

As shown in Figure 7, the capacitors and spark gaps are located below the coils. A closer view, Figure 8, shows the cable connections. The white tubes shown in this figure circulated dry air through the gaps.

The accelerator was operated without preionization or crowbarring A static fill of argon gas was used at 500 millitorr pressure. The bank voltage was 20 kv (5400 joules). At this voltage and pressure, a diamagnetic plasma current sheet formed with no observed delay as can be seen from the circuit current (lower trace) in Figure 9. The initially large rate of current rise followed by a reduced rate of fall at the end of the first half-cycle is characteristic of close coupled inductive accelerators. Another characteristic feature of the circuit current in pinch
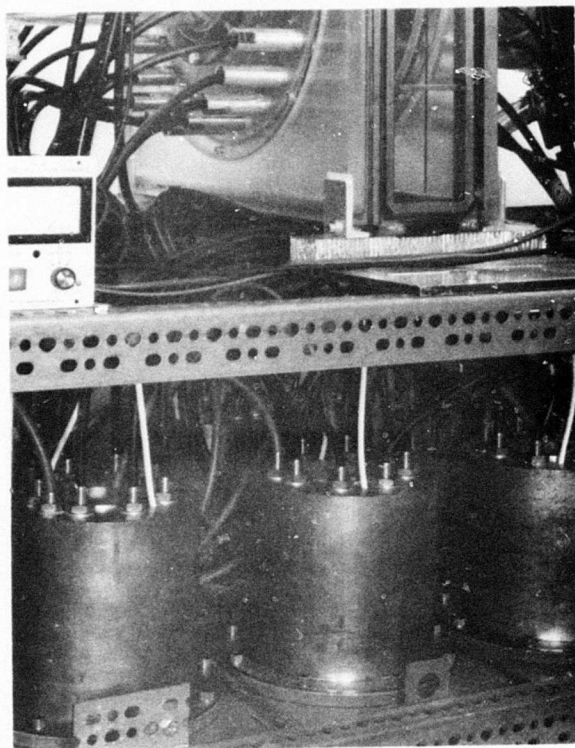
Figure 8.   View Showing Cable  Connections at
Coil and Spark Gap Housings

devices can also be seen in this figure.  At about 2 μsec after the current
starts rising in each half cycle there is a kink in the curve where dI/dt
suddenly increases.  At this time the individual planar plasma current
sheets have collided at the midplane between the coils and the impedance
due to the rate of inductance increase, which was positive,  suddenly goes
to zero.  The associated voltage drop, I(dL/dt) must then be supplied by
an increase in the other inductive voltage drop term,  L(dI/dt).  The upper
trace in Figure 9 is argon II light viewed along the axis of the accelerator
(three shot overlay).  A photograph of the accelerator firing, illuminated
by its own light, is shown in Figure 10.

The region of maximum brightness is a thin annular disc where the
sheets of accelerated plasma collide at the midplane.  This is seen in
the time exposure photographs shown in Figures 11 and 12.  This zone
appears to be 1 to 2 mm thick and has a radial extent nearly the same as
that covered by the coil wires.
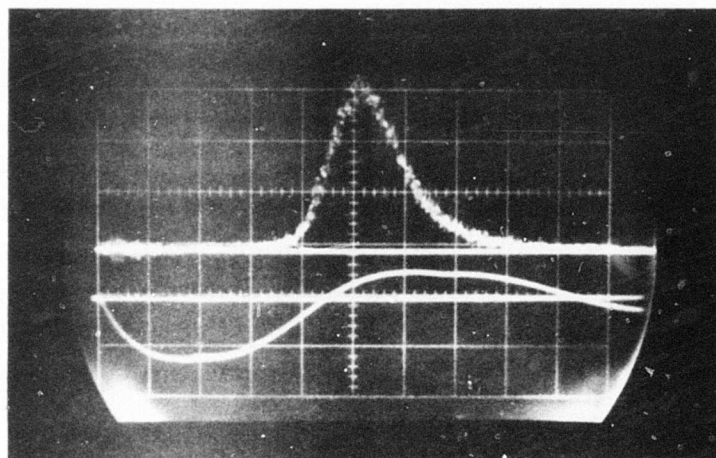
Oscillograph Traces Showing Circuit Current
(Lower) and Argon II Light (Upper). Three
traces overlay, 1 μsec/cm sweep speed.

Figure 10.   Time Exposure of Accelerator Firing
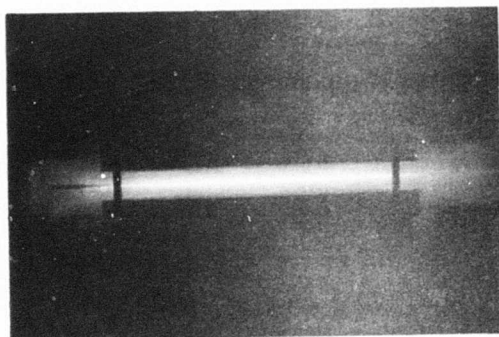


Figure 11.   Time Exposure of Dis-
charge—Side View   .
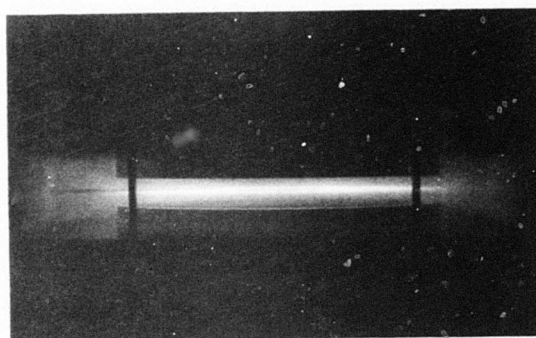


Figure 12.   Time Exposure of
Discharge—Inclined
View Showing Dark
Center Disc

13

### 3.1.1 Magnetic Field Mapping

Magnetic field memeasurements were made with miniature probes located at the tip of a glass tube that was introduced into the plasma from the top of the chamber and extended parallel to the coil surfaces. The probe shaft therefore ran parallel to the plane of the plasma current sheet. The probe carriage, which permitted continuous positioning both axially and vertically (radial) can be seen at the top of the vacuum chamber in Figure 6. The probe itself is visible in Figures 11 and 12 where it is located at the midplane in the thin region of maximum brightness.

A check on possible interference from the probe shaft was made by two sets of data, one with a 6 mm diameter glass tube and the other with a 3 mm diameter glass tube. The probes were individually calibrated and the measurements were made two months apart. Spot checks of the results showed agreement to within ±5%.

The probes used in the 6 mm diameter glass tubing consisted of 20 turns with a 2 mm diameter window. The second pair of probe coils were about half this dimension in the axial and circumferential directions. In order to retain sensitivity they were extended about 8 mm in the radial direction. This was felt to be acceptable since radial variations in this accelerator geometry are small compared to axial ones and there are no gradients in the circumferential direction.

The coil geometry of the axial magnetic field probe was a rectangle 1 mm wide in the circumferential direction and 9 mm long in the radial direction. The coil had 10 turns of #36 wire. The radial magnetic field probe was a one layer solenoid, 1 mm in diameter by 8 mm long in the radial direction, with 40 turns of #36 wire. The probes were calibrated with Helmholtz coils driven with a sinusoidal generator, the current being measured by a Hewlett-Packard Model 456 A current probe.

Magnetic probe data were recorded at a sweep speed of 0.5 μsec/cm. The probes were terminated in 52 ohms at the oscilloscope and their signals integrated passively with a time constant of 100 μsec. Data scans were made at 2 cm radial intervals and 2 mm axial intervals. The resulting oscilloscope traces were read and plotted directly as functions of time

14

with axial position as parameter for each radial station. Radial magnetic field plots are shown in Figure 13 through 16 for radial stations of 8, 12, 16 and 20 cm, respectively.

Axial distributions can be visualized in these figures as the intersection with the data plots of vertical planes passing through the constant time lines. For times up to about 1.5 μsec, the propagating magnetic field typical of the single coil accelerator can be seen. About 1 μsec is required for the toe of the field distribution to reach the midplane at 18.1 mm. At about 1.6 μsec the field lines begin to dip and reach a minimum at about 2 μsec. This time corresponds to the sudden rise in dI/dt, shown as the kink in circuit current in Figure 6, that occurs when plasma layers collide at the midplane.

Another interesting feature of the radial magnetic field plots is the linear decrease in $B_r$ with z after the separate current sheets have coalesced into a single one. Petschek's illustration in Figure 3 shows a finite region at the midplane where $B_r$ = o and the field energy stored in $B_r$ has already been converted to kinetic energy. The present data do not show such a region. $B_r$ decreases linearly with z all the way to the midplane.

The general magnitude of the radial magnetic field is comparable for radial stations of 8, 12, and 16 cm, but has decreased noticeably at the 20 cm station. The 16 cm radial station is the neutral point (or circular ring) where Bz = o. It is not only the neutral point of the fully developed field configuration (usually a consequence of being the locus of initial collision of the two sheets) but is also the location of Bz = o for the separate axially accelerating current sheets as a consequence of the coil geometry which produces a maximum radial magnetic field at this radius.

The magnetic field maps in Figures 13 through 16 provide a visualization of the current sheet development as time progresses. Spatial field distributions can be made for any time by erecting lines from the r-t plane to the corresponding contour plots and drawing a continuous curve through the intersection points. Flux plots, or maps of the magnetic field lines, are also helpful in conveying an intuitive feeling of the accelerator operation. For example, the vacuum field in the space between the coils is

15

Figure 14. Radial Magnetic Field as a Function of Axial Position and Time for 12-cm Radius ($R_{max}$ = 20 cm)



Figure 13. Radial Magnetic Field as a Function of Axial Position and Time for 8-cm Radius ($R_{max}$ = 20 cm)

16

Figure 16. Radial Magnetic Field as a Function of Axial Position and Time for 20-cm Radius ($R_{max}$ = 20 cm)



Figure 15. Radial Magnetic Field as a Function of Axial Position and Time for 16-cm Radius ($R_{max}$ = 20 cm)

17

essentially axial, so that deviations from an axial map of magnetic flux contour lines (i.e., lines of constant magnetic flux) are seen as the consequence of plasma currents. At early times, the plasma current sheets near the coil confine the magnetic field to the layer between each coil and its current sheet. Within this layer the resultant field is nearly radial and the thickness of the layer grows with time as the current sheet moves toward the midplane. Another interesting feature is the x-type neutral point which must appear at a radius of 16 cm and must have the same general appearance as Figure 3. The development of this x-type field configuration as time progresses, as well as the progress of the initial current sheets across the accelerator and the diffusion of field lines ahead of the current sheet can be seen in field line maps.

Such maps have been prepared from the experimental data using a time sharing computer with a Cal Comp plotter and existing subroutines that accept a matrix of experimental data points, read from hand faired curves, and fits curves to these points that have continuous first and second derivatives. This made it feasible to compute and plot current density contour maps from the magnetic field data in addition to the field contour maps.

The spatial intervals of the original probe measurements were 2 cm in the radial direction and 2 mm in the axial direction. This is a matrix of 110 test shots each for the radial and axial magnetic fields. These 220 oscilloscope traces were plotted and faired to make consistent families at each radial station like those shown in Figures 13 through 16. These data were then read at 0.1 μsec intervals and input to the computer. This was a total of 40 time steps for 220 plots or 8800 input data values. The final key punched values were then printed out, examined for inconsistencies and edited.

The three characteristic phases of this accelerator are: first, the period of axial motion when each current sheet is essentially unimpeded by the other and the rising inductance dL/dt describes the real load impedance in ohms, second, the collision phase beginning with the forward edge of the current sheets which carry little moving plasma and ending with the collision of the axially moving mass layers, and third, the period of radial mass motion of shock heated, highly conductive, plasma which

18

carries flux inward inside the neutral radius and expels it outward at larger radii. These phases are shown in the three groups of flux contour maps of Figures 17a, 17b and 17c, respectively. Figure 18 shows a series of 10 plots of both current density and magnetic flux contours for a time span of 4.0 μsec at 0.4 μsec intervals. The flux contour intervals are 0.0005 Webers for all frames and the current density intervals are $5 \times 10^6$ amps/$M^2$, with zero corresponding to the heavy lines. The upper plot in each frame is current density and the lower plot is magnetic flux.



Figure 17a. Magnetic Flux Lines from 0.2 to 1.2 μsec, $2 \times 10^4$ W/Line

Figure 17b. Magnetic Flux Lines from 1.4 to 2.4 μsec, $3 \times 10^4$ W/Line



Figure 17c

Magnetic Flux Lines from 2.5 to 3.0 μsec, $3 \times 10^4$ W/Line
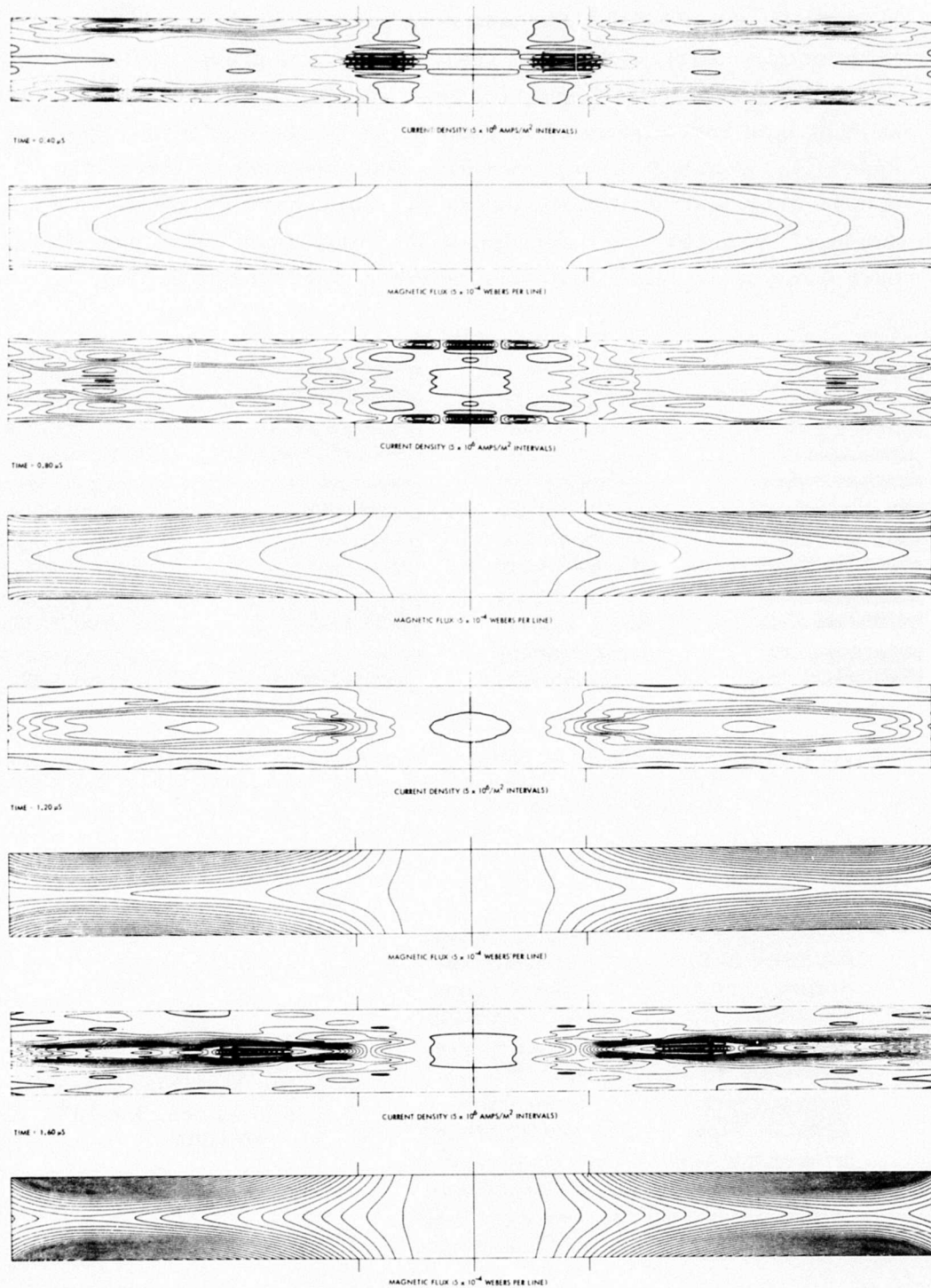
Figure 18. Plasma Current Density and Magnetic Flux
Contour Maps for the Time Intervals Shown

20

CURRENT DENSITY (5 x 10⁶ AMPS/M² INTERVALS)

TIME = 2.00 μS

MAGNETIC FLUX (5 x 10⁻⁴ WEBERS PER LINE)

CURRENT DENSITY (5 x 10⁶ AMPS/M² INTERVALS)

TIME = 2.40 μS

MAGNETIC FLUX (5 x 10⁻⁴ WEBERS PER LINE)

CURRENT DENSITY (5 x 10⁶ AMPS/M² INTERVALS)

TIME = 2.80 μS

MAGNETIC FLUX (5 x 10⁻⁴ WEBERS PER LINE)

Figure 18.   Plasma Current Density and Magnetic Flux
Contour Maps for the Time Intervals
Shown (Continued)

21

TIME - 3.20 μS       CURRENT DENSITY (5 x 10⁶ AMPS/M² INTERVALS )

MAGNETIC FLUX (5 x 10⁻⁴ WEBERS PER LINE)

TIME - 3.60 μS       CURRENT DENSITY (5 x 10⁶ AMPS/M² INTERVALS)

MAGNETIC FLUX (5 x 10⁻⁴ WEBERS PER LINE)

TIME - 4.00 μS       CURRENT DENSITY (5 x 10⁶ AMPS/M² INTERVALS)

MAGNETIC FLUX (5 x 10⁻⁴ WEBERS PER LINE)

Figure 18.    Plasma Current Density and Magnetic Flux
Contour Maps for the Time Intervals
Shown (Continued)

22
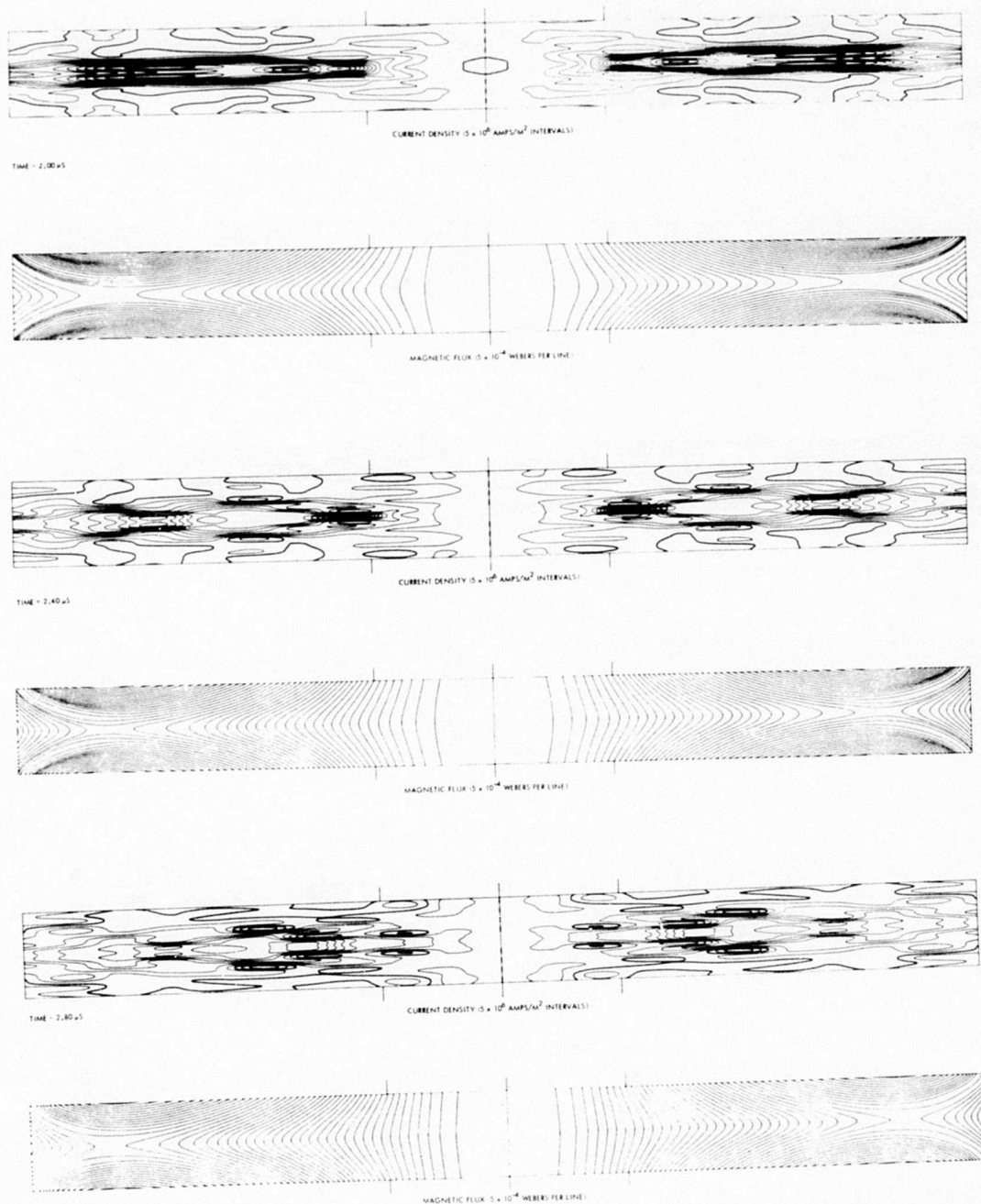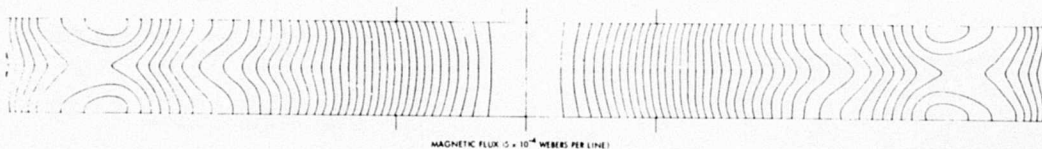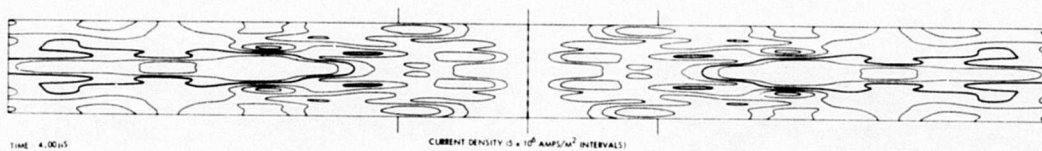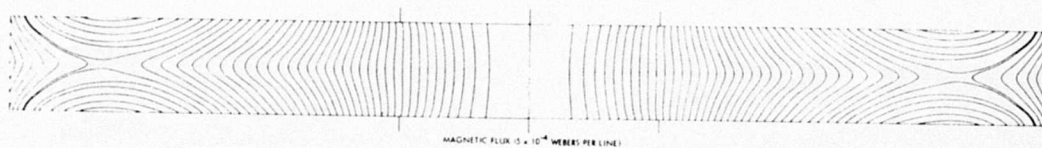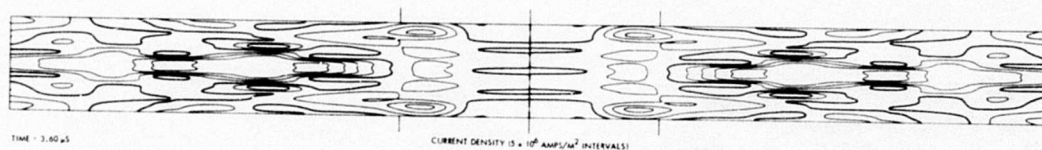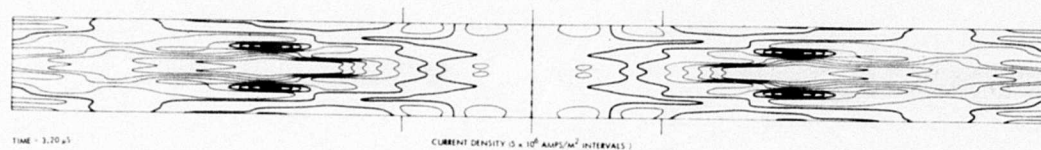
Plots of current density versus axial position for 16 cm radius, at several times, are shown in Figure 19. Except for the 4.0 μsec case, these plots correspond to the contour maps shown in Figure 18. At 1.2 μsec the sheets have begun to merge at the midplane and at 2.0 μsec the current density has risen to a maximum of 10,000 amps/cm$^2$, or about 50% more than the maximum of the individual current sheets. At this time the total current sheet thickness is a little more than one cm. The thickness increases slightly, but the current sheet remains concentrated near the midplane as it decays. It is interesting that the current density maximum has receded from the midplane at 2.4 μsec. This is discussed in more detail later.
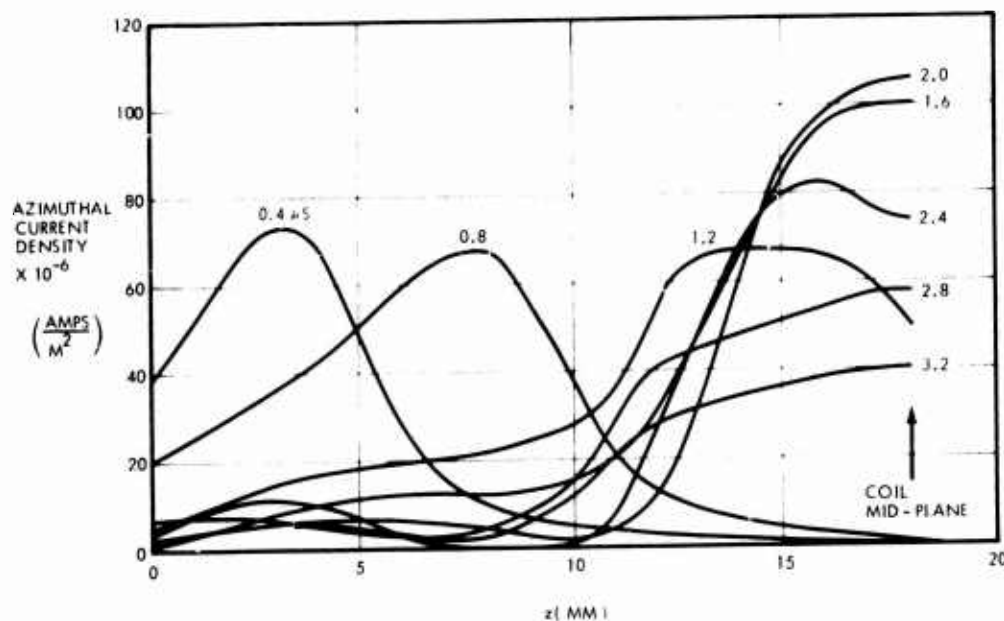


Figure 19. Plasma Current Density Distribution
at 16 cm Radius

### 3.1.2  Plasma Conductivity

The neutral line at 16 cm radius is a convenient location for an experimental determination of conductivity because the mass velocity and both magnetic field components are zero at all times so that the conductivity is simply

$$\sigma = \frac{j_\theta}{E_\theta} \tag{1}$$

23

The probe measurements already described determine both $j_\theta$ and $E_\theta$; the latter is the time variation of flux ($B_z$ probe) within the neutral radius. However rapid changes in both $j_\theta$ and $E_\theta$ occur during collision so that better time resolution is required for a good ratio determination than was possible from those data. Accordingly, the electric field was measured with a probe having a pair of exposed electrodes separated 1.2 cm in the $\theta$ direction. Each probe tip had a small wire (antenna) attached to it to increase the current collection area. This wire extended 2 mm from the probe tip in the positive and negative z directions (4 mm total length). This introduced some uncertainty in the $E_\theta$ structure because of possible averaging over the center 4 mm of the current sheet. As a check on the electric field probe data, $E_\theta$ was also determined from magnetic flux variation measured with the $B_z$ probe and the agreement was reasonably good.

The curl of the magnetic field is determined almost entirely by the radial component at the midplane. The spatial variation of the current density can therefore be accurately determined by $B_r$ probe measurements. Figure 20 shows the current density distribution over the central 4 mm of the current sheet for times ranging from 1.2 to 3.4 µs in 0.2 µsec steps. As a check on consistency, the average current density over the Rogowsky window area was determined from these distributions and found to be satisfactory, as shown in Figure 21. Also shown in Figure 21 is the high resolution current density at the midplane (z=o in Figure 19). The sudden drop at 2.3 µsec is related to the collision of the plasma masses. This effect also appears in the electric field which is compared with $j_\theta$ in Figure 22. The maximum current density at 2.2 µsec is related to the maximum electric field at that time.

The conductivity, determined from Equation (1) is also shown in Figure 22. It increases about 50% when the plasma masses collide and remains at the higher level as radial motion develops.
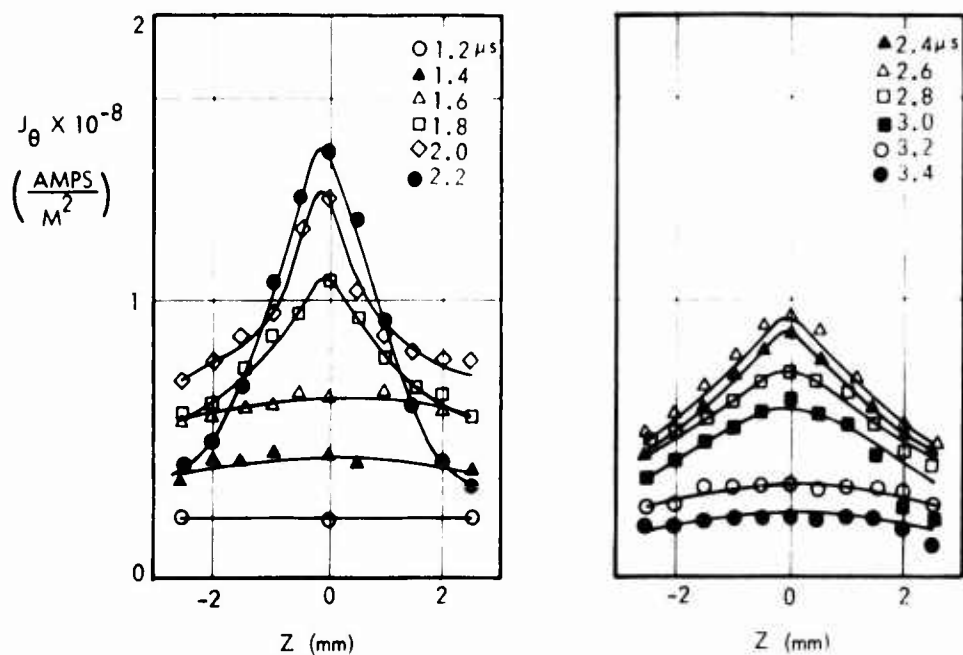
Figure 20. Axial Distribution of Current Density Near Midplane
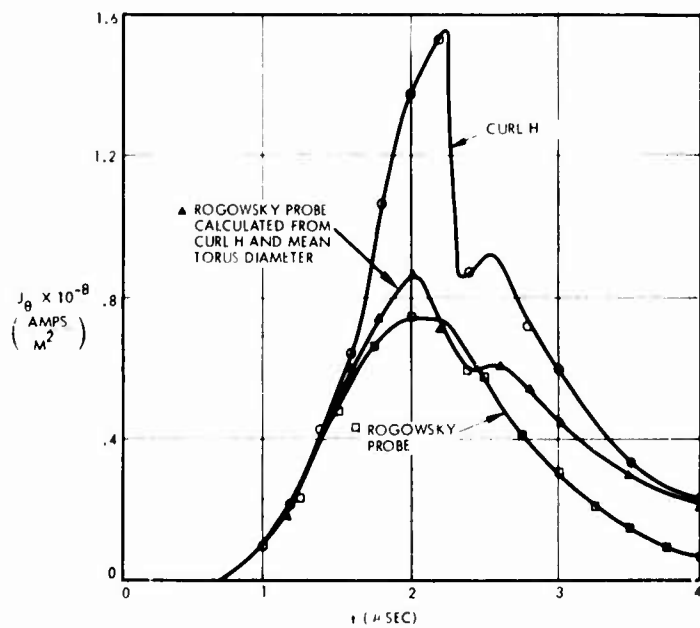


Figure 21. Comparison of Current Density at Midplane for Rogowsky and Curl H Measurements
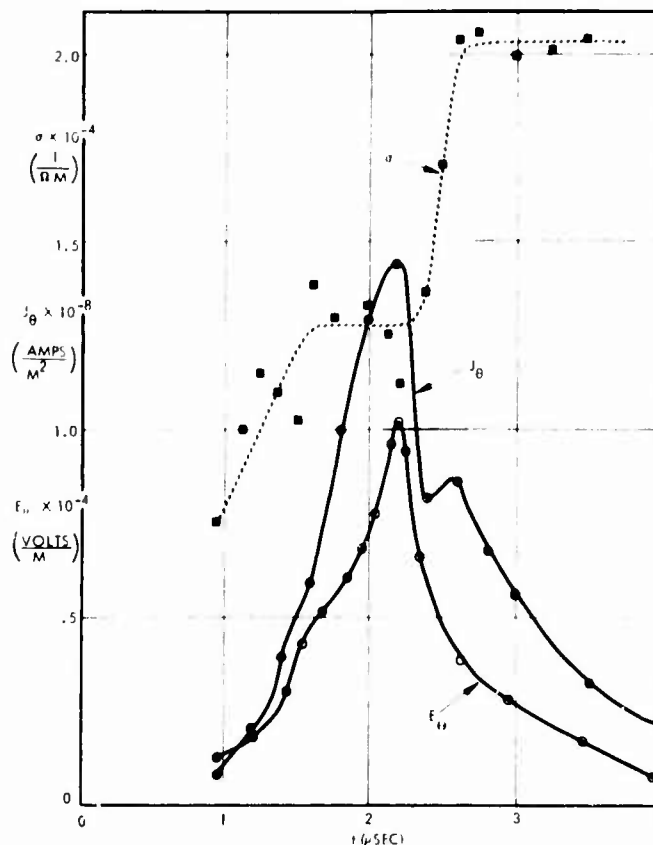
Figure 22. Time Variation of Conductivity Determined by $E_\theta$ and $J_\theta$ at Coil Midplane

### 3.1.3 Spectral Measurements

### 3.1.3.1 Electron Temperature at Discharge Center

The intensities of several argon II (once ionized argon) spectral lines were used to measure the electron temperature at the axis of the coils. For the relatively high densities typical of this experiment, the populations of the higher lying atomic levels are to a good approximation controlled by electron collisions with radiative processes being relatively unimportant.[11] Since electron collisional excitation is balanced by its inverse process, electron collisional deexcitation, and since the collision times are much shorter than the time scale of the experiment, these atomic levels are populated according to a Boltzmann distribution. Hence, the intensity of line radiation from these levels is given by

26

$$I = Ch\nu g A e^{-\frac{E}{KT_e}}$$

or

$$\ln\left(\frac{I}{g A \nu}\right) = -\frac{E}{KT_e} + \ln(Ch) \qquad (2)$$

where

I  = line intensity

C  = constant

h  = Planck's constant

$\nu$  = frequency of the transition

g  = multiplicity of the upper state

A  = atomic transition probability

E  = upper state energy

K  = Boltzmann's constant

The slope of the line determined by plotting $\ln\frac{I}{g A \nu}$ versus E, using experimental values for I, is $-\frac{1}{KT_e}$.

The intensities of seven argon II lines from the 4S-4P, 3D-4P, and 4P-5S arrays were measured. These lines originate from levels having energies varying from 19.2 (above the ion ground state) to 24.6 ev and range in wavelength from about 4000 to 5000 Å. Light from the plasma was imaged onto the input slit of a half meter Jarrel-Ash monochromator by a 200 mm telephoto lens. The line of sight was axial and passed through the center of the discharge. A photomultiplier, whose output was recorded on an oscilloscope, detected light at the exit slit.

The result of the measurement for t = 5.5 μsec, the time of peak continuum emission at the discharge axis, is displayed in Figure 23. Transition probabilities listed by Wiese et al.[12] were used to produce this graph. The experimental points are a reasonable fit to a straight line with $T_e$ equal to 3.8 ev.
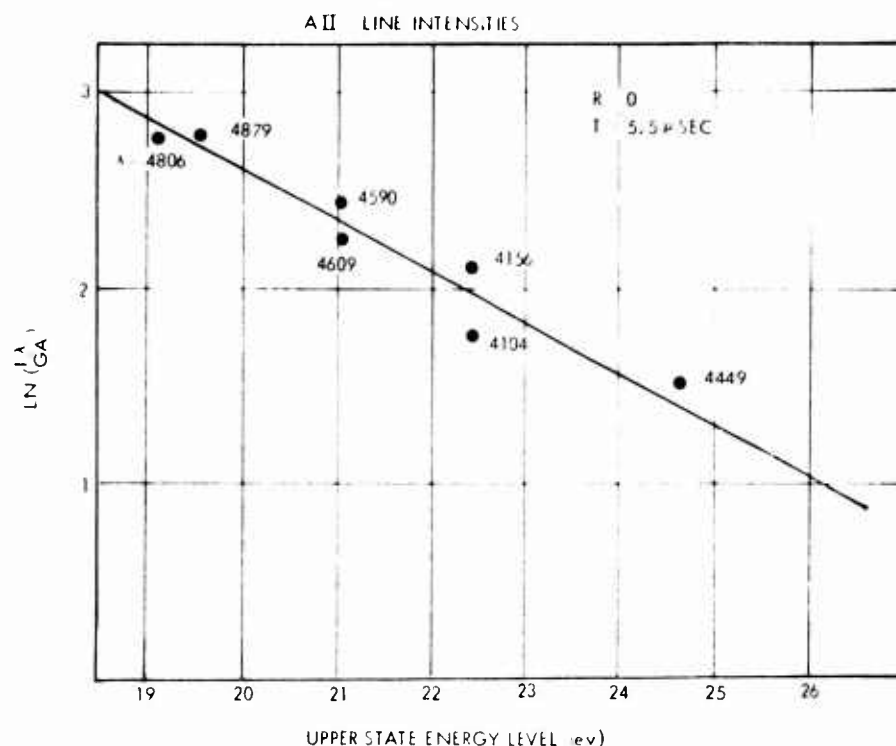
Figure 23. Spectral Line Intensity Measurement

3 1.3.2 Spectral Line Profile Measurements at r = o

The measurement of an argon II line profile at the discharge center was undertaken to determine either the ion temperature or electron density. In the limit of low electron density and high ion temperature, the principal line broadening mechanism is Doppler broadening caused by the thermal motion of the emitting ions; if the ions are in thermal equilibrium, the profile has a Maxwellian shape whose width is given by the ion temperature. In the other limit where the electron density is high and the ions are cold, the dominant broadening mechanism is Stark broadening caused by the perturbation of the emitting ions by the fields of nearby particles. The Stark broadened line shapes of heavy elements can be closely approximated by the Lorentzian function[13]

$$I(\Delta\lambda) \propto \frac{1}{1 + \left(\dfrac{\Delta\lambda}{\Delta\lambda_{\frac{1}{2}}}\right)^2}$$
(3)

The half-width, $\Delta\lambda_{\frac{1}{2}}$, depends strongly on electron density and very little on temperature.

Profile measurements of the argon II line at 4806 Å were made. The experimental setup was the same as that for the line ratio measurement at the axis except that the entrance slit was adjusted for 0.2 Å resolution. The line was scanned by recording data from two shots of the machine at each wavelength setting, which was varied by 0.2 Å steps.

Figure 24 shows the results of this measurement plotted for 4, 5, 6 and 7 μsec. The peak line intensity and maximum width occur at
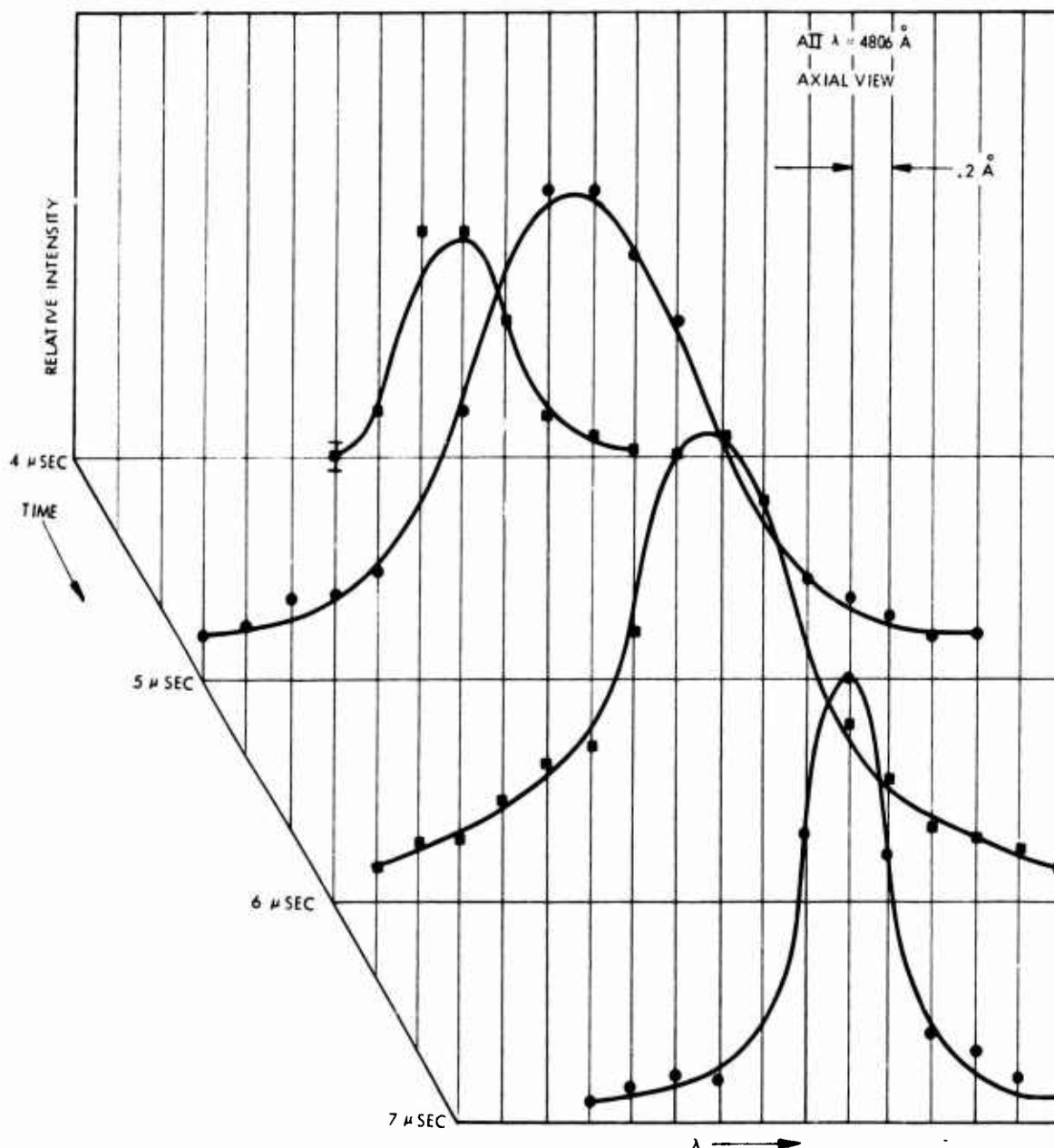
Figure 24. Argon II Spectral Line Profiles

5.4 μsec, which is coincident with the maximum continuum emission. Figure 25 shows the profile at 5.4 μsec compared with a Lorentzian having a full width of 1.12 Å at half of maximum intensity. The excellent agreement is strong evidence for Stark broadening. The possibility that the line profile is Doppler broadened but that the ions are not in thermal equilibrium, is unlikely but cannot be entirely ruled out. Assuming an average ion energy given by the half width of the profile and the electron density equal to the atomic fill density, the energy equipartition time for ions is about 2 μsec. The observed magnetic field compression along with the continuum peak implies that the plasma is compressed so that the energy equipartition time is probably less than 2 μsec.

Assuming Stark broadening as the most likely mechanism, it is possible to infer an electron density from the theoretical line broadening parameters, given by Griem,[14] and the measured half width and electron temperature. Taking $\Delta\lambda = 1.12$ Å yields $n_e \approx 4.0 \times 10^{23}/M^3$ at $r \approx 0$ and $t = 5.4$ μsec. An electron density this high would require a strong compression at the center of the discharge or a more modest compression and
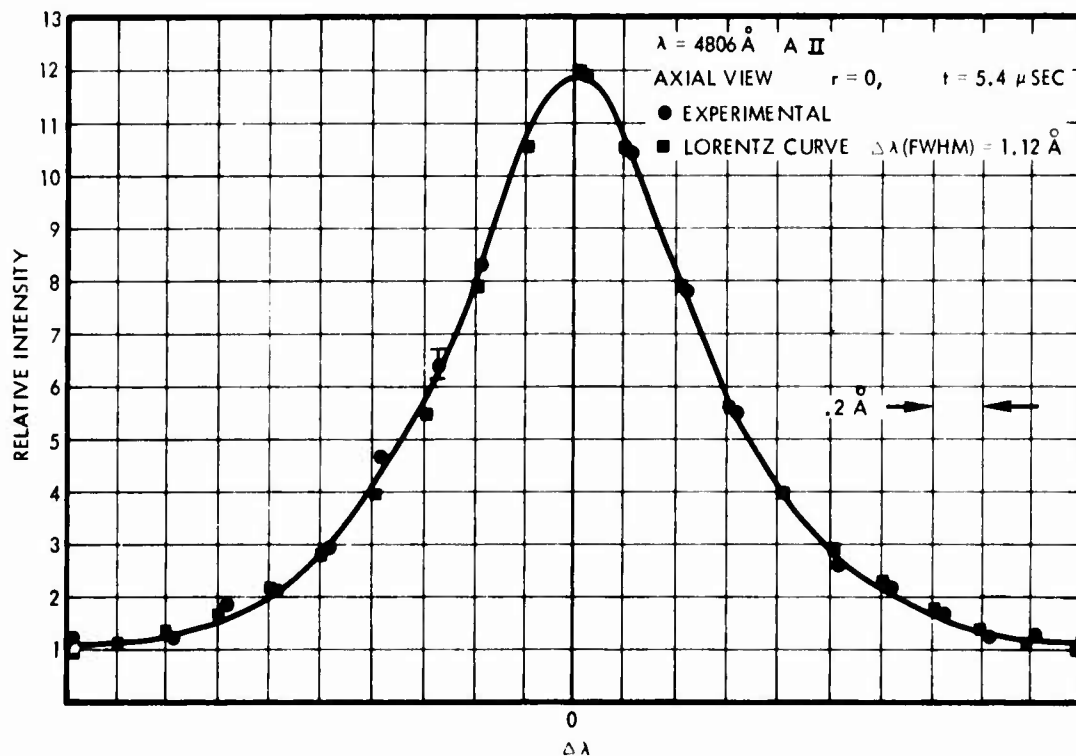


Figure 25. Argon II Spectral Line Profile at 5.4 μsec

30

multiple ionization. Since multiple ionization would probably produce A
III line emission, a search for the A III line at 3858 Å was undertaken;
however, line emission at 3858 Å could not be detected. For single ioniza-
tion and $n_e \simeq 4 \times 10^{23}/M^3$ , it would be necessary to compress the plasma
initially in the region inside of the neutral radius into a disk about 2 cm
wide by 3 cm in radius. Framing pictures showed a luminous region with
similar dimensions but with a 1 cm radius hole or dark region at the
center.

To reiterate, the observed argon II line broadening is most likely
caused by Stark broadening. The density implied by the half width is
$4 \times 10^{23}/M^3$. Doppler broadening from non-Maxwellian ions seems
unlikely because of the short energy equipartition times.

### 3.1.3.3 Spectral Line Profiles at the Midplane

In an attempt to observe directed radial motion of the plasma, by
means of Doppler shifts of spectral lines, line profiles were measured
along a radial line of sight in the midplane of the discharge. The line of
sight through the center was blocked at $r = 0$ so that light from only the
half diameter towards the observer was accepted. If this were not done,
outward radial motion for example, would be observed as both a blue
shift of light emitted by ions closest the observer and a red shift of light
emitted by ions on the far side of the plasma. The unavoidable perturba-
tion of the obstructing object made the data for the time of the compres-
sion at the center not valid.

The experimental procedure was similar to that described for the
line profile measurements at $r = 0$. In addition, the center wavelengths
of the lines measured at the midplane were compared with the wavelengths
of the same lines originating near one coil face at the beginning of the
discharge. Such line radiation emanating from near the coils during the
initial gas breakdown should not be Doppler shifted because plasma motion
does not have time to occur. The positions of the line centers of the two
sets of lines agreed within instrumental precision or about 0.1 Å.

Figure 26 presents profiles for the argon II line at 4848 Å while
Figure 27 shows the profiles for the argon III line at 3858 Å. A salient
feature of these spectra is the drop in line emission at the time the cur-
rent sheets collide. The continuum radiation shows a burst at this time.
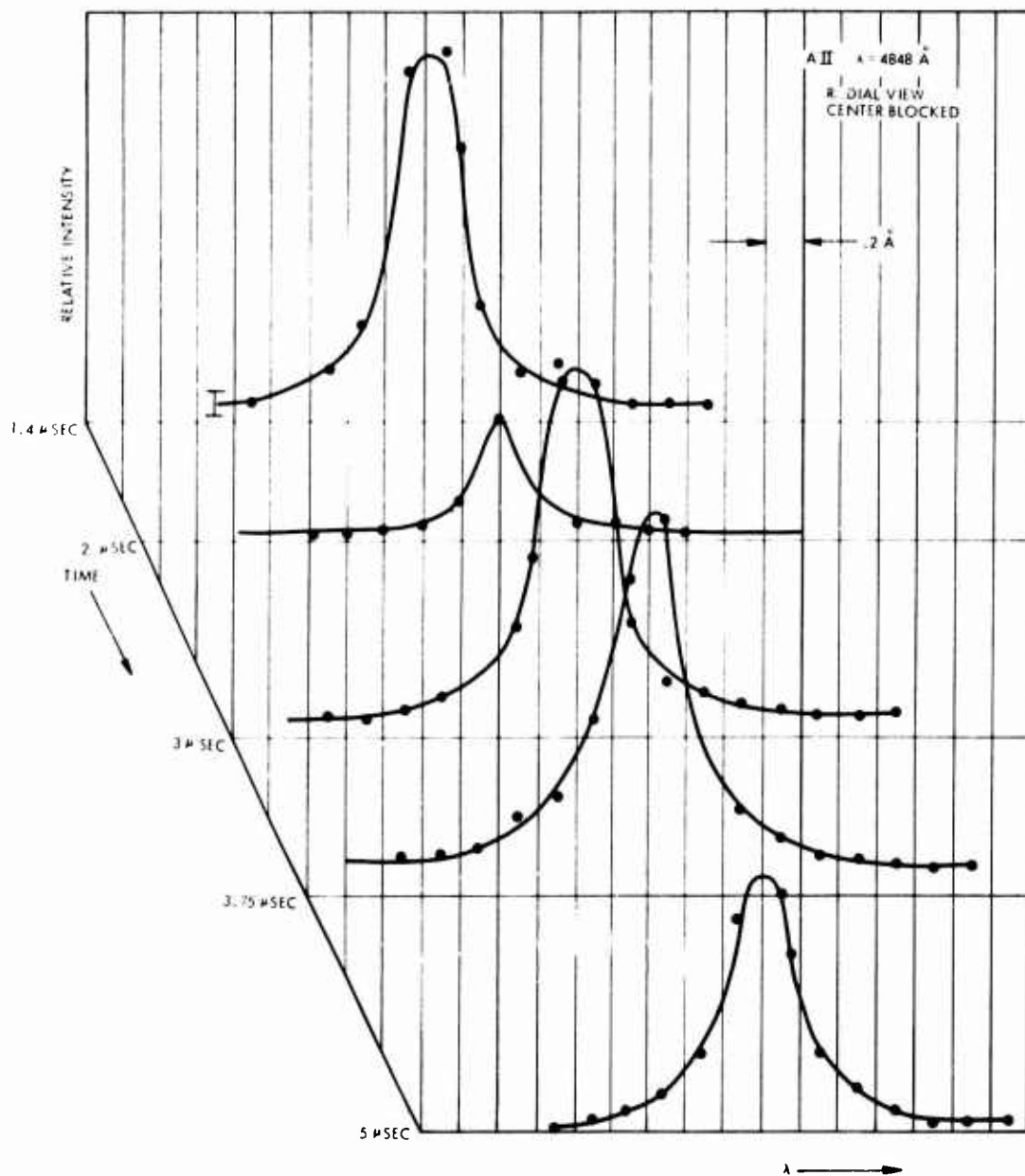
Figure 26. Argon II Spectral Line Profiles

One possible explanation is that when the current sheets collide the ions
are excited to the higher levels of ionization (i. e. , triple ionization or
higher) causing the argon II and III line emission to be quenched.   It would
be simple to test this hypothesis by searching for argon IV line emission;
however, no argon IV lines are available in the visible spectrum.   The
argon III line peaks at 2.5 μsec while the argon II maximum emission

32
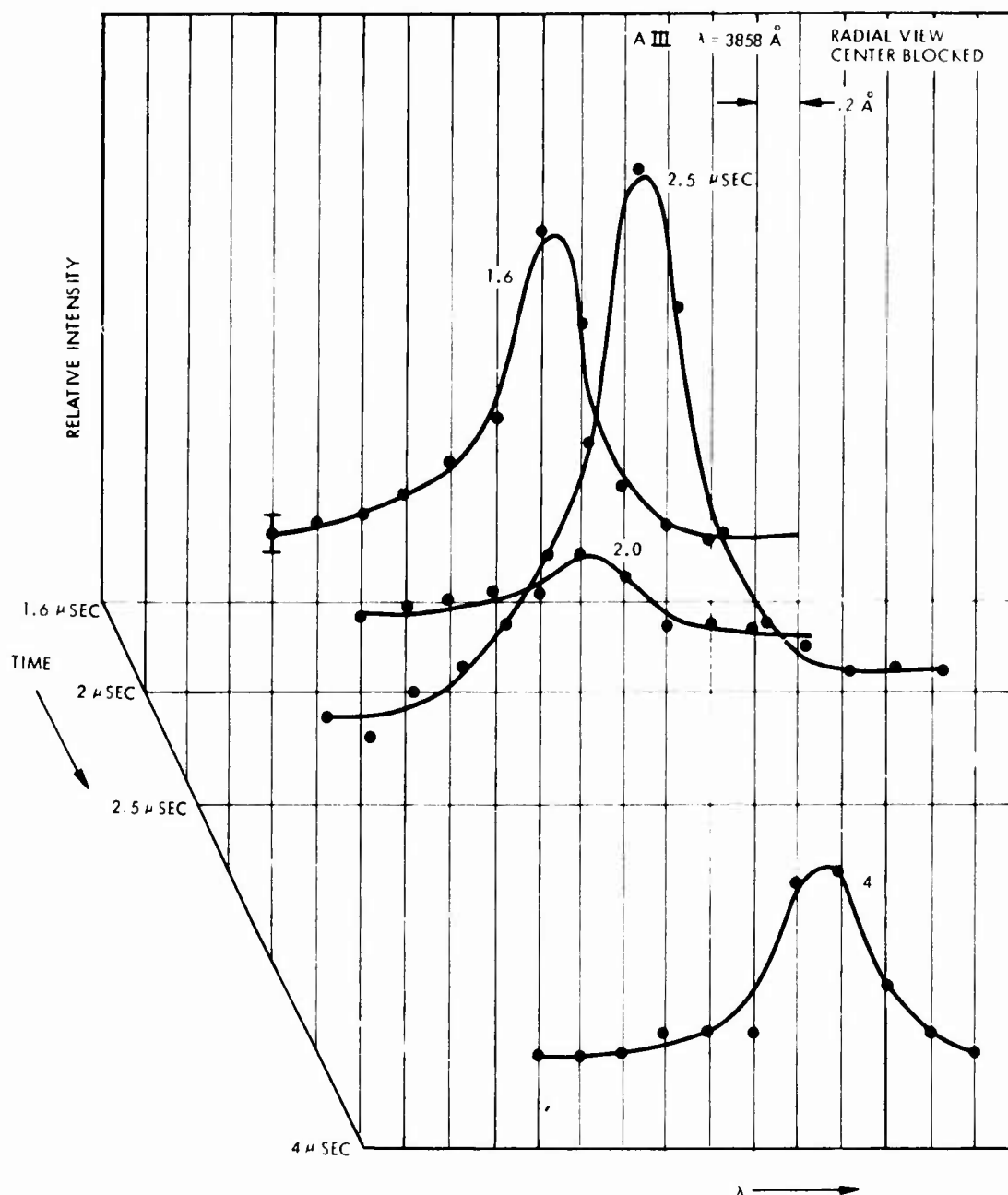
Figure 27. Argon III Spectral Line Profiles

occurs at 3 to 4 μsec. The plasma is probably twice ionized at 2.5 μsec since the 3858 Å argon III line emanates from a level 29.7 ev above the argon III ground state or 56.1 ev above the argon II ground state. For an electron temperature of about 4 ev it is unlikely that this level would be populated enough for observable emission if the ions were singly ionized.

Figure 28 shows the profile of the 4848 Å argon II line at 3 μsec along with a Lorentzian with a half width of 0.34 Å for comparison. The close agreement between the experimental points and the comparison curve is strong evidence for Stark broadening. If the broadening parameters given by Griem[14] are used the inferred electron density is 1.2 x $10^{23}/M^3$. This is consistent with a compression of the initial neutral fill density into an 8 mm wide band at the midplane with twice ionized ions. The framing pictures show that the luminous region of the discharge (the luminosity of heavy ion plasmas is usaully associated with electron density), is confined to such a band.
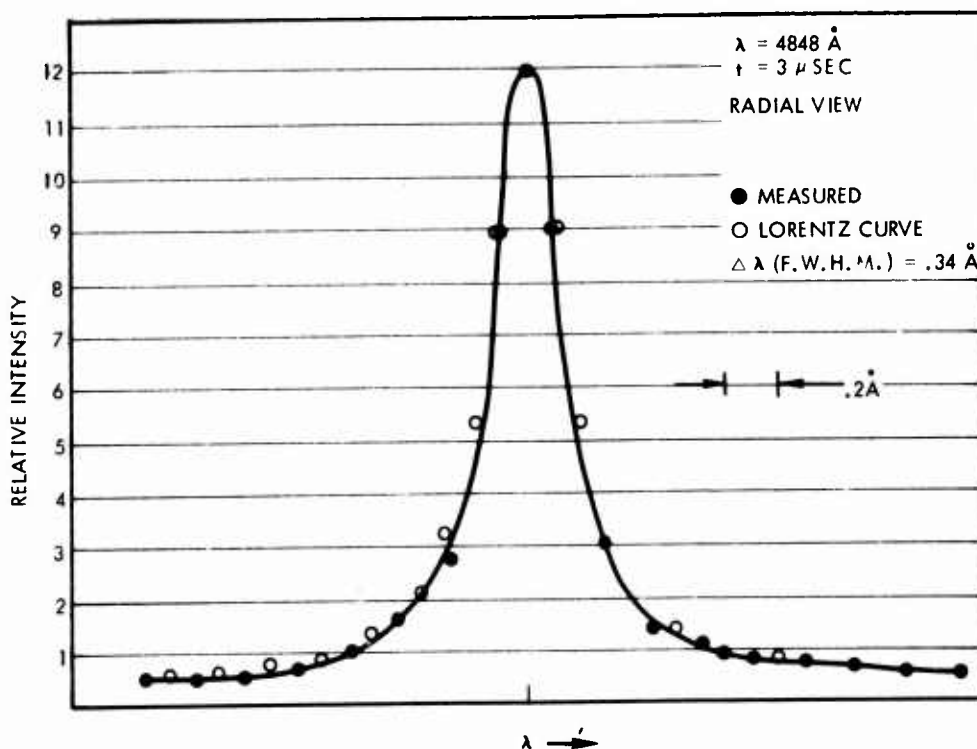


Figure 28. Argon II Spectral Line Profile at 3 μsec

## 3.1.3.4 Electron Temperature Determination at the Neutral Radius

Measurement of the electron temperature at the neutral radius allows a comparison of the measured conductivity with that inferred from the classical (Spitzer) relation.[15] Anomalously low conductivity may result from micro-instabilities having electric fields which scatter electrons and produce a large effective electron collision rate. Since

nonclassical conductivity has been observed in the earlier field annihila-
tion experiment,[10] it is important to compare the conductivity in this
experiment with that inferred from classical theory.

Again, the electron temperature was determined from measured
argon II line intensities. The high electron diensities (about $10^{23}/M^3$)
typical of this plasma at the midplane after the sheets collide insure that
partial thermodynamic equilibrium holds for the atomic transitions used.
That is, collisional processes as opposed to radiative processes deter-
mine the populations of the upper states of the optical transitions mea-
sured. Five argon II lines were measured along a line of sight in the
midplane of the discharge passing through a minimum radius equal to
9 cm. This line of sight sampled light emitted from plasma with an
average radial position equal to that of the neutral radius. Poor optical
access through the coils precluded a measurement in the axial direction
which would have given better radial resolution. Time did not permit
measurement at several radii which would be needed for an Abel inversion
to obtain radial resolution.

The monochromator entrance slit width was set for an instrumental
resolution of 1.3 Å. This was adequate since the most broadened lines
had widths which were typically 0.4 Å. If the slit width had been made
wider to include the far wings of each line, the increased continuum radi-
ation, falling within the instrument band width would have made the line
intensity measurement more difficult. As it was the strong continuum
level made it impossible to measure the line intensities accurately enough
to infer electron temperature for the times of peak continuum emission,
i.e., from 2 to 2.7 μsec.

Figure 29 shows the results of the temperature measurement as a
function of time. The temperature at 1.5 μsec is about 3.7 ev, slowly
increasing to approximately 5 ev at 4 μsec.

Figure 30 shows the calculated value of $\sigma$, using $T_e$ and the Spitzer
relation, compared with the value measured from $E_\theta$ and $j_\theta$. The ion
density has been taken to be $10^{23}/M^3$. From 1 to 2 μsec the agreement
is excellent, while at 3 μsec the calculated value is about 25% less than
the measured value. No temperature measurement was possible for the
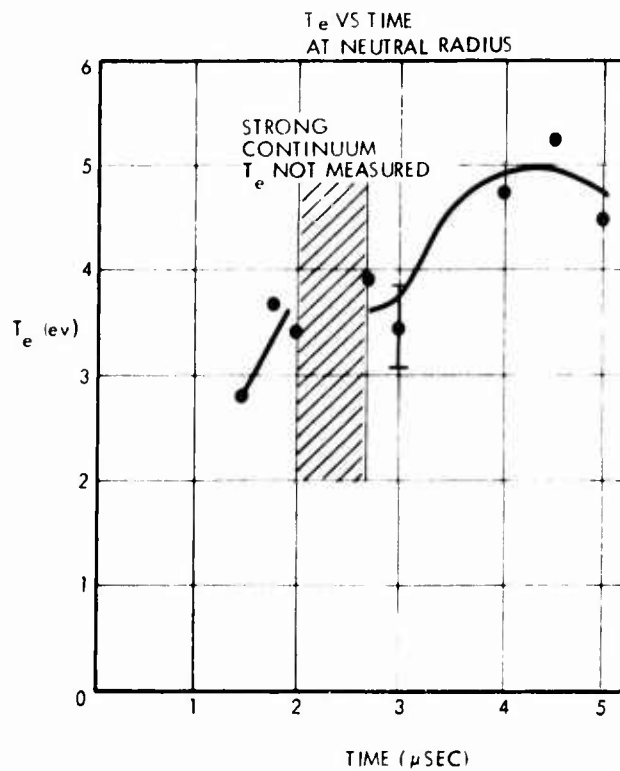
Figure 29. Electron Temperature at the Neutral Radius
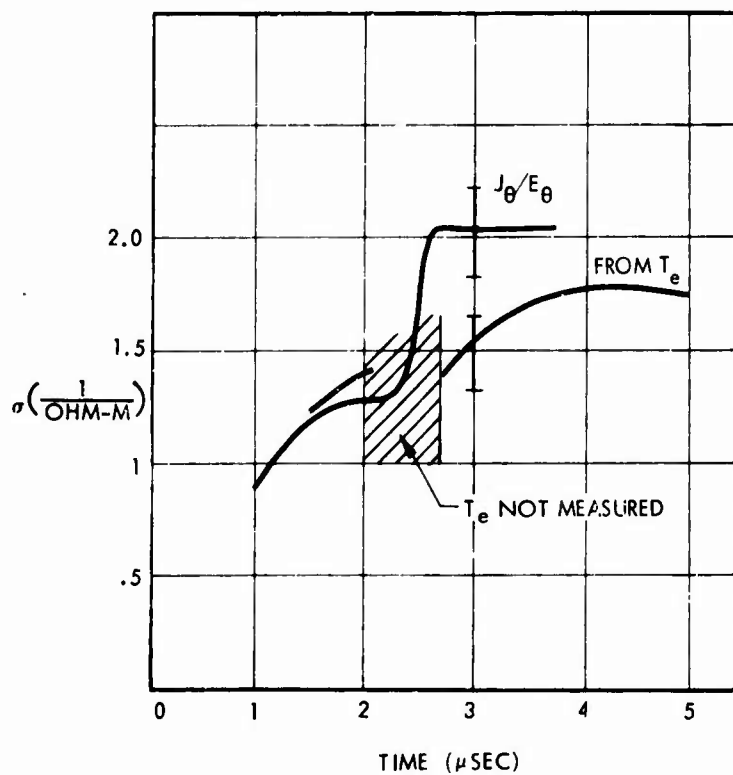


Figure 30. Conductivity at the Neutral Radius

36

interval from 2 to 2.7 μsec. It is important to note that the measured conductivity after collision is larger than the Spitzer value. If there were an additional resistive mechanism, the measured value would be smaller, not larger, than the classical value. Thus the comparison demonstrates that, in this experiment, the conductivity is determined solely by classical Coulomb collisions.

### 3.1.4 Time Resolved Photography

### 3.1.4.1 Center Region

Figure 31 shows image converter framing camera pictures at the discharge center. The line of sight is axial and the region seen has its maximum radius equal to 4.1 cm.

For heavy ion plasmas, such as this one, the plasma luminosity is closely identified with plasma density. At 3.5 μsec the plasma has moved into the central region and has an inner radius of 2.5 cm. At 5.5 μsec the plasma is fully compressed into an annular region bounded by 0.6 and 3 cm radii. Magnetic probe measurements show that $B_z$ flux which leaks through the poorly conducting gas at the center at early times is strongly compressed by the inward moving plasma, seen in these photographs. The exclusion of the moving plasma by this compressed field produces the hole seen at the center. Subsequent to this time the plasma decays away as can be seen in the pictures for 6.5 and 7.5 μsec.

Figure 32 shows a streak photograph of the center of the discharge using a mask aligned horizontally and the line of sight parallel to the axis of the device. The time axis is up, and the streak duration is from 0 to 10 μsec. The implosion can clearly be seen. The inward velocity of the plasma front is inferred to be about 1 cm/μsec.

t = 3.5 μ seconds

t = 4.5 μ seconds

t = 5.5 μ seconds

t = 6.5 μ seconds

t = 7.5 μ seconds

t = 10 μ sec

t

t = 0 μ sec
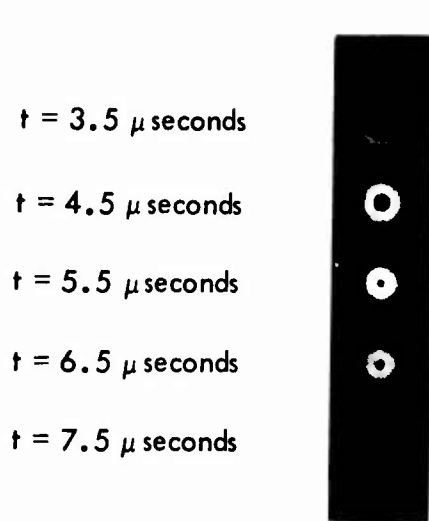
Figure 31. Framing Pictures of
the Discharge Center
Viewed Axially
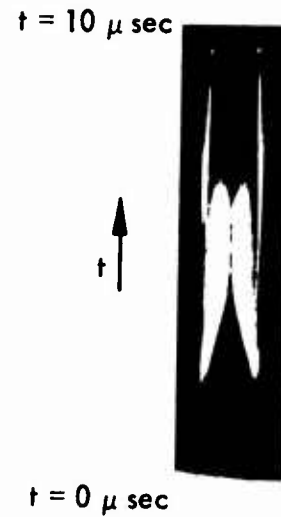
Figure 32. Streak Picture of the
Discharge Center
from t = 0 to 10 μsec

Figure 33 shows a streak for the interval 1.5 to 3.5 μsec after the
discharge is initiated. At about 2 μsec a burst of light (seen on the origi-
nal polaroid photograph) is emitted by the plasma which persists for about
0.2 μsec. This is at the same time and duration as the intense continuum
emitted as a result of the current sheet collision. There are two possible
explanations. First, a small fraction of the continuum is scattered by

t = 3.5 μ sec

LIGHT

t

t = 1.5 μ sec

8.5 m
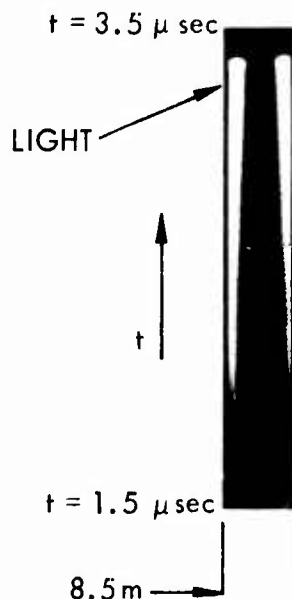
Figure 33. Streak Picture of the
Discharge Center
t = 1.5 to 3.5 μsec

solid surfaces along the line of sight of the camera. This seems unlikely because both surfaces are far removed from the plasma volume. Second, the plasma at the center is excited or photoionized by the UV component of the continuum and subsequently emits line radiation as it is deexcited. Strongly accelerated argon plasmas have been observed to be excellent UV sources for photoionizing argon. For example, 30% photoionization of neutral argon by an inverse pinch discharge was observed by one of the authors in an earlier study. It should be noted that Rayleigh or Thompson scattering of the continuum by the plasma at the center (probably not fully ionized) is highly unlikely because of the small Thompson and Rayleigh scattering cross sections ($\sigma_T \sim 10^{-24}$ while $\sigma_R \sim 10^{-26}$ cm$^2$).

### 3.1.4.2 Edge View

Figure 34 shows the center region of the discharge viewed along a radial line of sight. The center is necessarily viewed through the outer region of plasma. At 1.25 μsec the two current sheets have lifted off the coils and are approaching the midplane while at 2.25 μsec they have fully coalesced and the luminosity is confined to a region about 4.5 mm wide.

At 3.25 μsec the current layer has broadened, and its visible output has diminished considerably. The radial compression has become apparent by 4.25 μsec while 5.25 μsec is close to the time of peak compression. The luminous area near the coils is the second current sheet which forms as the voltage at the coils changes sign.
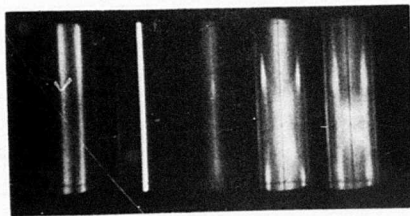


Figure 34

Framing Pictures of the
Discharge Center
Viewed Radially

## 3.1.5 Radial Impulse

An estimate of radial impulse was made by using the midplane measurements of $j_\theta$ and $B_z$ and assuming that the corresponding force density acted over a 1 cm wide region around the midplane.

Figure 35 shows radial distributions of $B_z$ at different times. The corresponding current density map is shown in Figure 36. The resulting force density distribution is plotted in Figure 37. The total radial force for the inner and outer regions is plotted in Figure 38 as a function of time and the corresponding impulse values are shown.
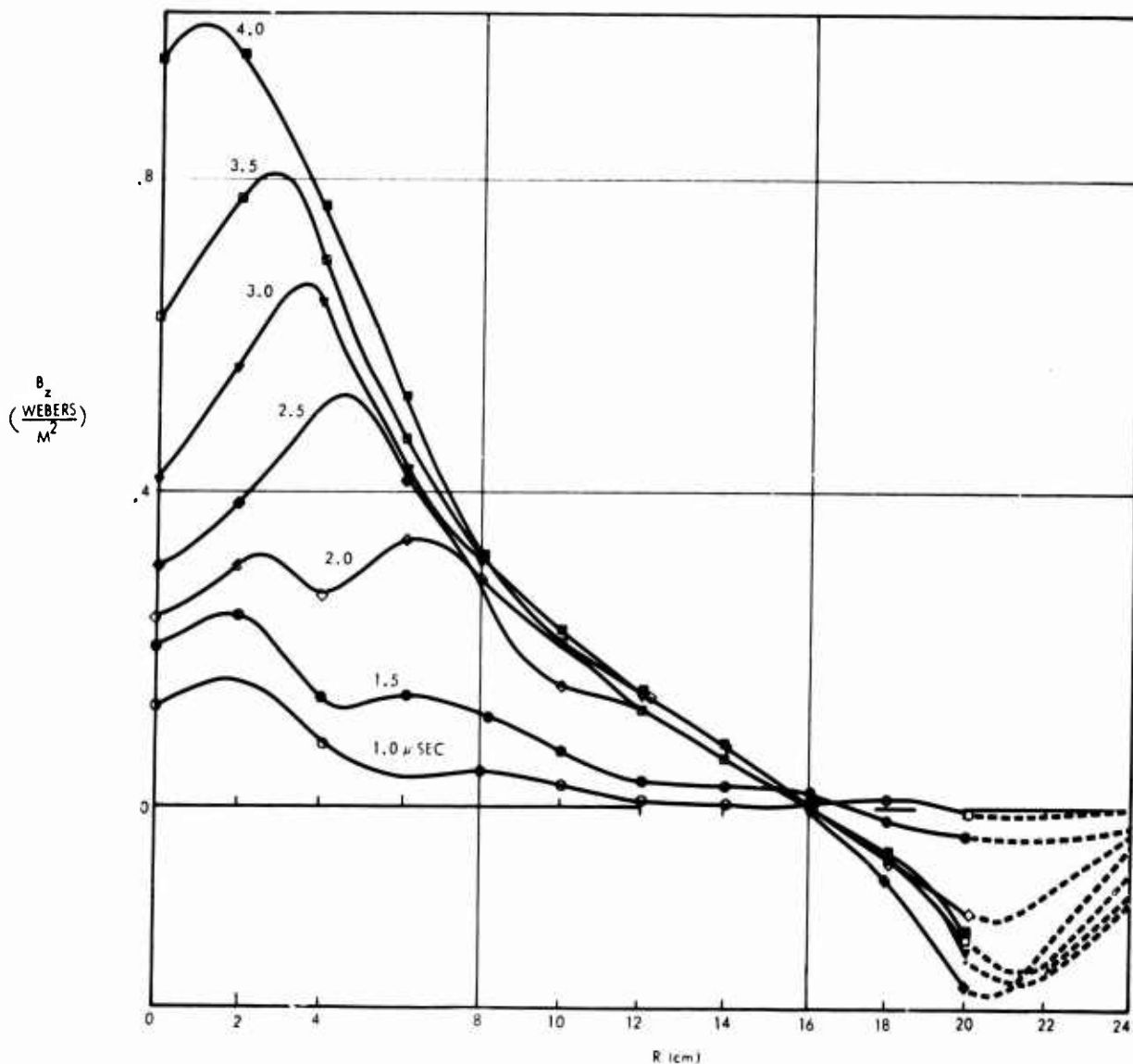


Figure 35. Axial Magnetic Field at Coil Midplane
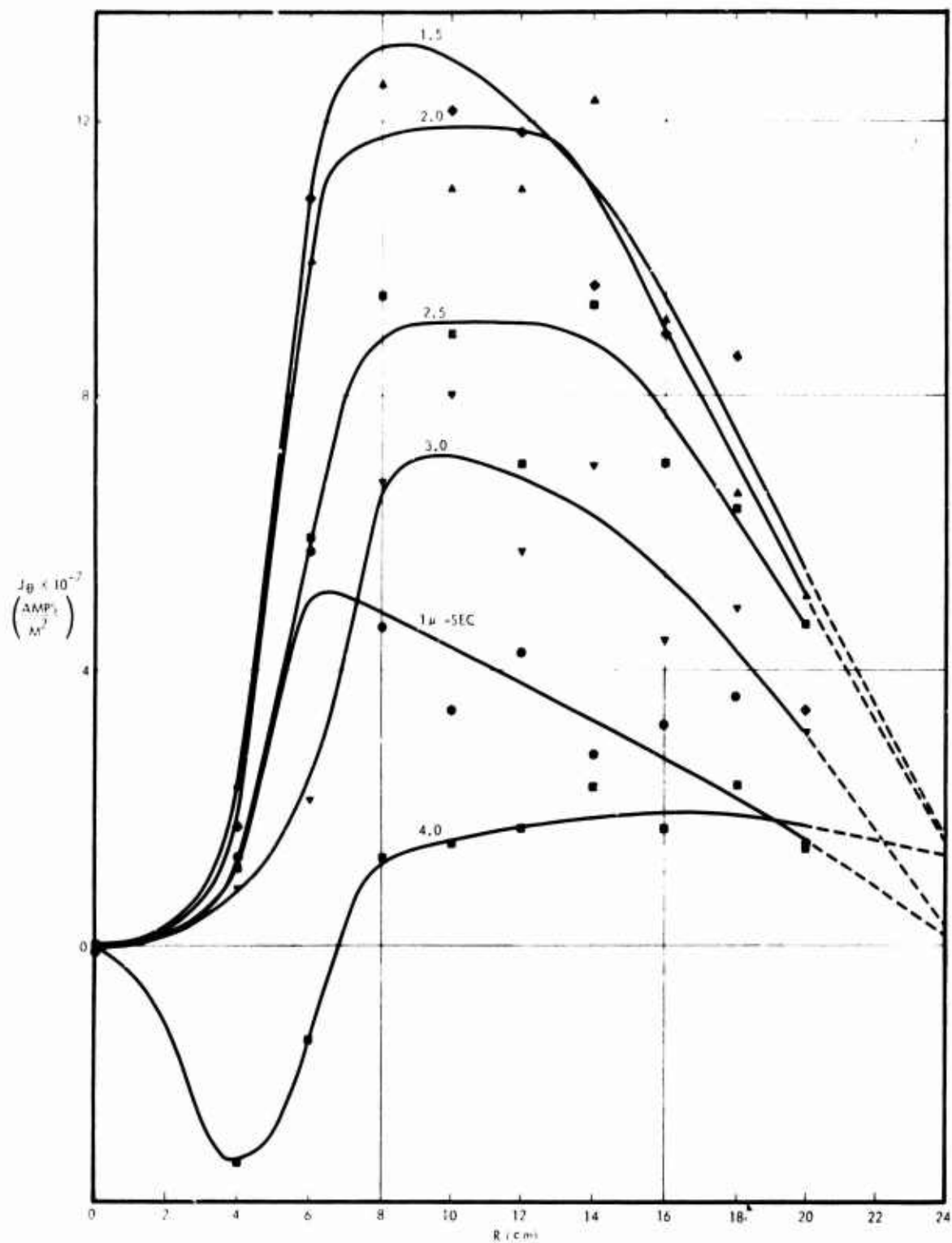
Figure 36. Current Density at Coil Midplane

41
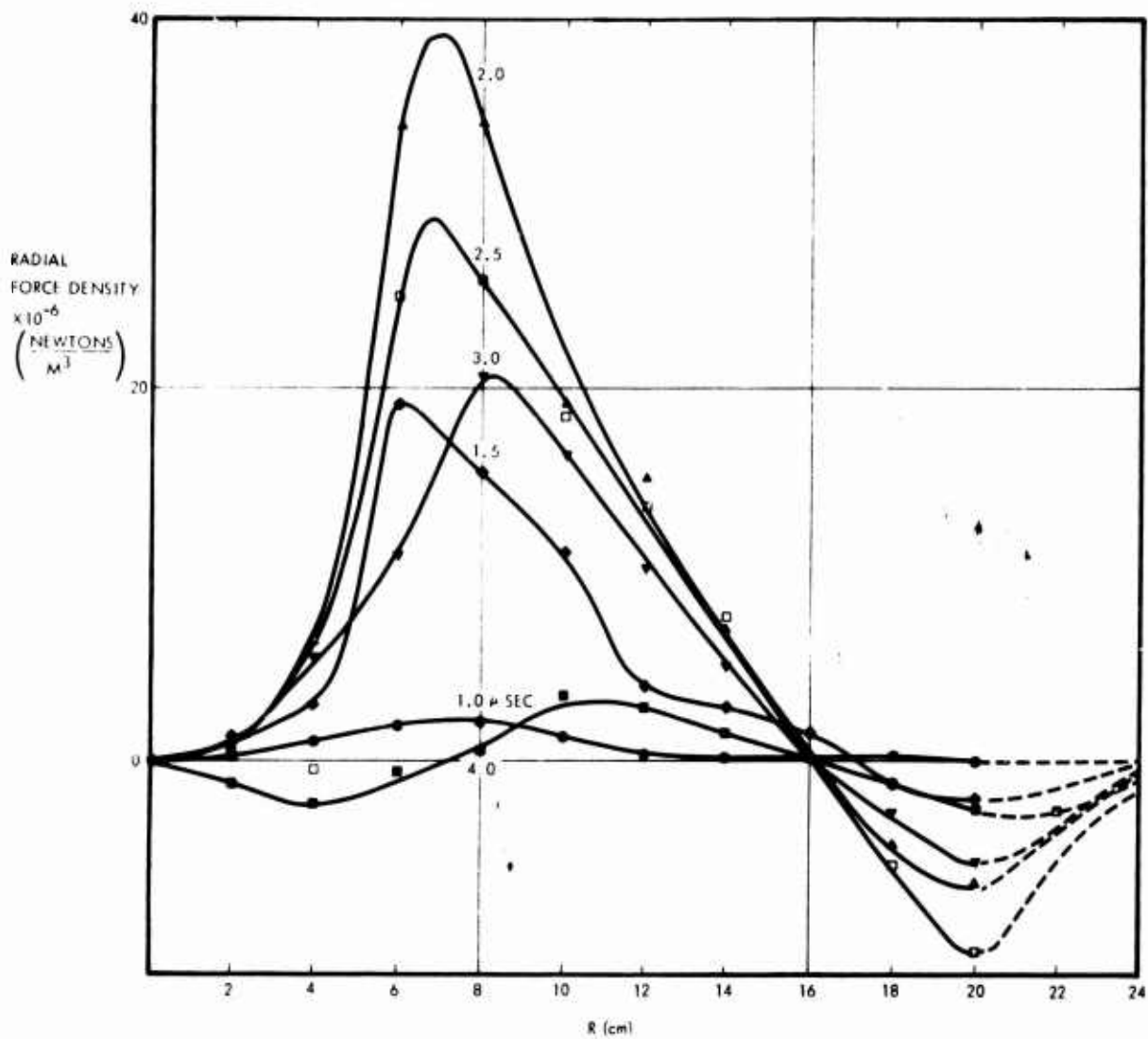
Figure 37.  Radial Force Density Distribution

If the impulse estimated in this manner is assumed to be delivered to the initial mass of gas between the coils,  an efficiency can be calculated as

$$\eta = \frac{I^2}{2M\,J}$$

where I is impulse,  M is mass and J is the capacitor bank energy.  The corresponding specific impulse is

$$I_{sp} = \frac{I}{Mg} \text{ (seconds)}$$

The mean plasma velocity is $V = gI_{sp}$.

42
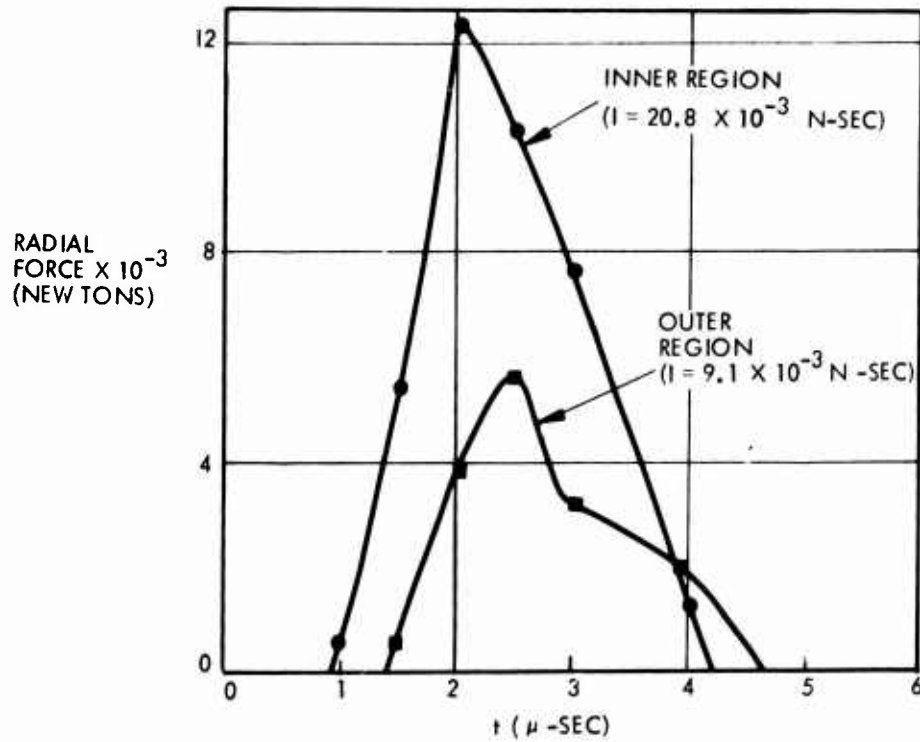
Figure 38. Time Variation of Radial Force

The efficiencies and mean plasma velocities were low. The highest velocity was $0.7 \times 10^4$ M/sec for the inner region. This was about half of the axial velocity before collision. For the outer region the velocity was $0.55 \times 10^4$ M/sec. The corresponding efficiencies were 2.1 and 1.4% respectively.

### 3.1.6 Plasma Collision at Neutral Radius

The neutral radius, where the axial magnetic field is zero, is about 16 cm. The radial variation of this magnetic field component is plotted for different times in Figure 39. For very early times, the neutral radius is near the outer edge of the coil (20 cm). It moves rapidly inward to 16 cm at 2.0 μsec and then moves out to nearly 17 cm after 2.6 μsec.

Figure 40 shows the variation of the radial magnetic field with axial position at different times for the same radius. At 1.8 and 2.0 μsec the curves show a structure which seems to correspond to the trailing edge of the mass layer. The slope at the midplane determines the current,

$$j_\theta = \frac{\frac{\partial B_r}{\partial z}}{\mu} \qquad (4)$$
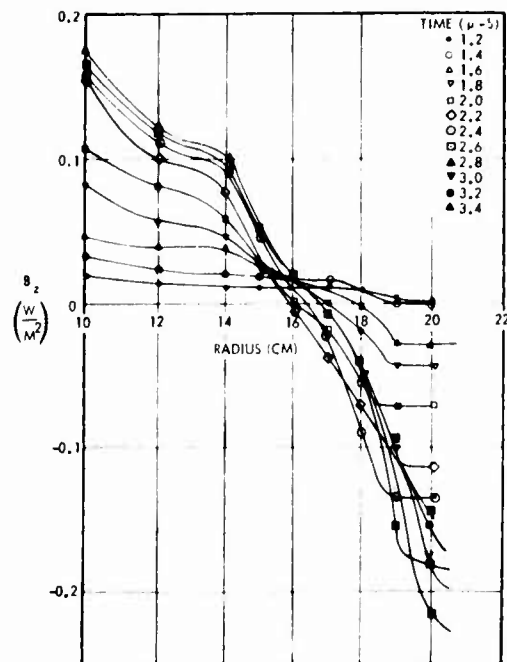
Figure 39.   Radial Variation of Axial Magnetic Field at 16 cm
Radius for Different Times
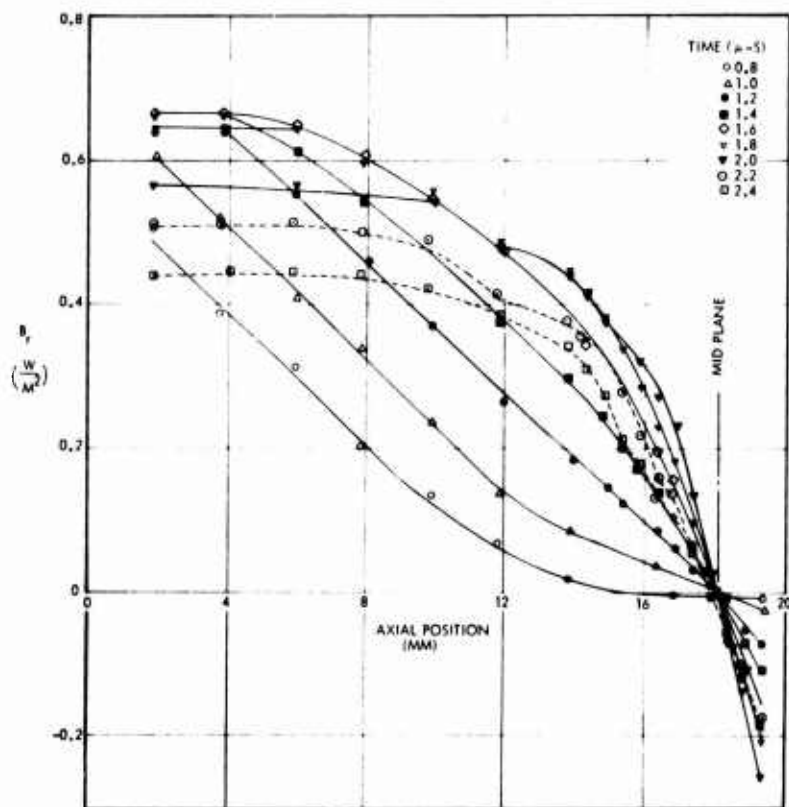


Figure 40.   Axial Variation of Radial Magnetic Field at 16 cm
Radius for Different Times

44

which is plotted as a function of time in Figure 41. The contribution from the other component of the curl has been omitted since it is less than 3% at all times.

Figure 41 also shows the time variation of the azimuthal electric field and the conductivity determined from the ratio of the current density to the electric field.

Oscilloscope traces of the radial magnetic field are shown in Figures 42 and 43 for axial positions at 0.5 mm intervals near the midplane.

All of the traces in Figures 42 and 43 have the same characteristic feature. The rising magnetic field seen at any fixed axial position reaches a maximum after which it rapidly decreases. A few tenths of a microsecond later the field abruptly stops falling and remains nearly constant. Careful examination of the traces shows the first abrupt change to be propagating inward toward the midplane while the second one propagates outward away from the midplane.

A cross plot of the inward moving feature shows its velocity to be $1.3 \times 10^4$ M/sec, which is a reasonable value for the axially moving plasma before collision. Thus the rising field before the maximum is reached, is due to motion of the radial magnetic field which accumulates within the mass layer because of the high conductivity (the diamagnetic effect) and the subsequent rapid decay corresponds to arrival of the region behind the mass layer where the curl of the magnetic field is very low. The fact that the peak is sharply defined implies a clean separation between the trailing edge of the mass layer and the low current region behind it.

The outward moving feature propagates more rapidly than the earlier inward motion of the mass layer. For example, the end of the period of rapidly decaying field for the lower trace in Figure 43 occurs only 0.1 $\mu$sec before the corresponding event for the upper trace in Figure 42. This feature is believed to be a magnetoacoustic wave whose speed is given by the relation

$$a^2 = \frac{\dfrac{B_r^2}{\mu} + \gamma k T_e (n_i + n_e)}{n_i M_i} \tag{5}$$

45
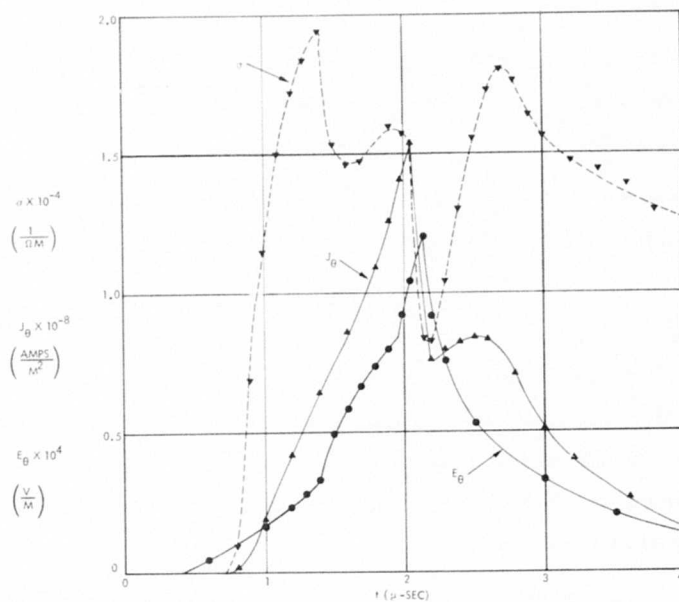
Figure 41. Variation of Current Density, Azimuthal Electric Field and Conductivity with Time at 16 cm Radius
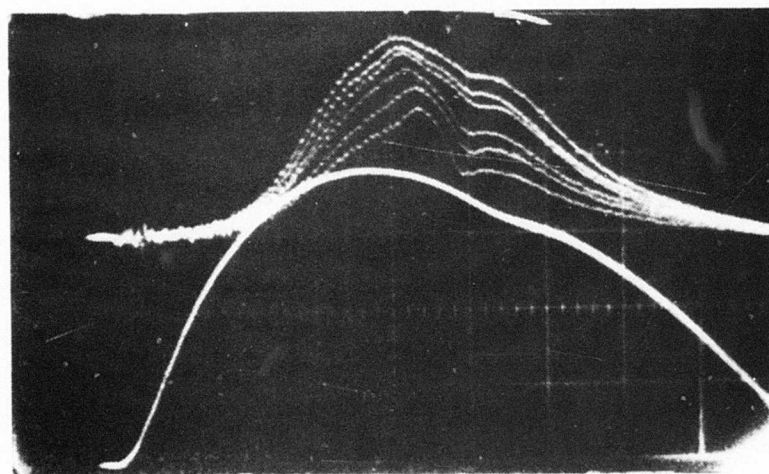


Figure 42. Radial Magnetic Field vs Time at 16 cm Radius
(z = 2, 2.5, 3, 3.5, 4 and 4.5 mm from midplane,
0.5 μsec/cm sweep, lower trace is circuit current)

46
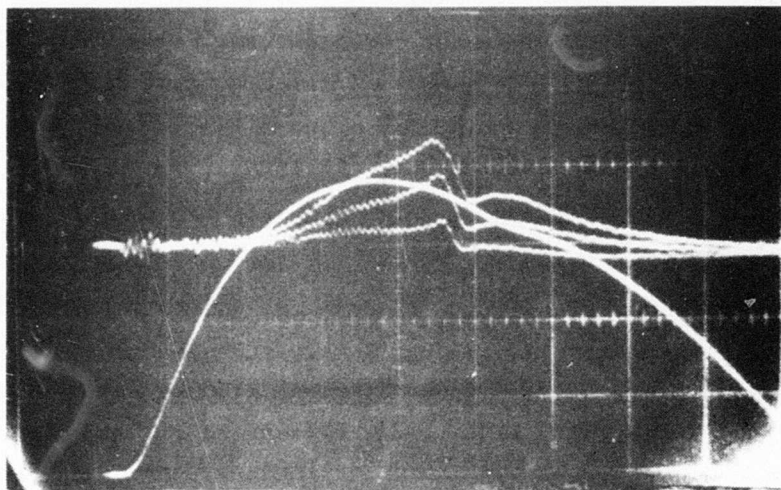
Figure 43.  Radial Magnetic Field vs Time at 16 cm Radius
(z = 0.5, 1, 1.5 mm, 0.5 μsec/cm sweep,
lower trace is circuit current)

where γ is the specific heat ratio 5/3 and k is Boltzmann's constant.

A cross plot of the outward moving feature shown in Figure 44 gives a velocity variation with axial position which, with the corresponding magnetic field values from Figure 40 gives a constant ion density of about $0.5 \times 10^{20}$ per $M^3$ for all positions more than 0.5 mm away from the midplane.
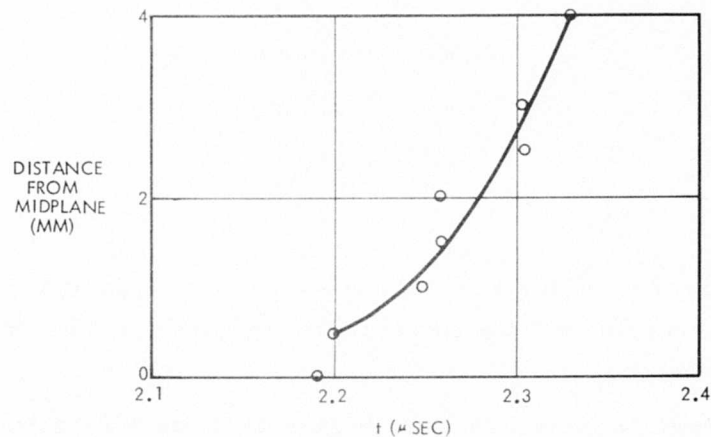


Figure 44.  Arrival Time for Outgoing Waves (R = 16 cm)

Thus nearly all of the mass corresponding to the initial fill density of $1.6 \times 10^{22}$ is compressed within a 1 mm thick disc at the midplane at an average density of

$$n_i = \frac{3.6 \text{ cm}}{0.1 \text{ cm}} \times 1.6 \times 10^{22} = 5.8 \times 10^{23} \text{ per M}^3$$

A rough check on electron temperature and wave speed can be made from the curve drawn in Figure 44. The minimum slope of the arrival curve is the thermal acoustic speed given by Equation (5) with $B_r = 0$. The value shown is $0.5 \times 10^4$ M/sec, or 0.5 mm per 0.1 μsec. This is consistent with an ionization level of 2.8 and $T_e = 2.8$ ev.

The detailed features shown in Figure 41 for both $E_\theta$ and $j_\theta$, and consequently $\sigma$, were accurately determined by the oscilloscope traces. The current density was determined by cross-plotting the traces shown in Figures 42 and 43 and $E_\theta$ was recorded directly as illustrated in Figures 45 and 46 for two radii.

As an aid in interpreting the events at the midplane which are shown in Figure 41, the conductivity and the plasma state relation (ion density, plasma temperature and degree of ionization Z) were calculated for local thermodynamic equilibrium and using the following recent data for incremental ionization energies:

$$V_1 = 15.75 \text{ ev}$$
$$V_2 = 27.62 \text{ ev}$$
$$V_3 = 40.90 \text{ ev}$$
$$V_4 = 59.79 \text{ ev}$$

The result is plotted in Figure 47. Also shown in Figure 47 is a grid of recombination rates calculated according to Spitzer's relation for radiative recombination.[15]

The most striking feature of Figure 41 is the abrupt drop in conductivity associated with the collision of the incoming mass layers at 2.1 μsec. The 0.1 μsec delay between $j_\theta$ maximum and $E_\theta$ maximum is real and must be accounted for in an explanation of the event. It should also be

48
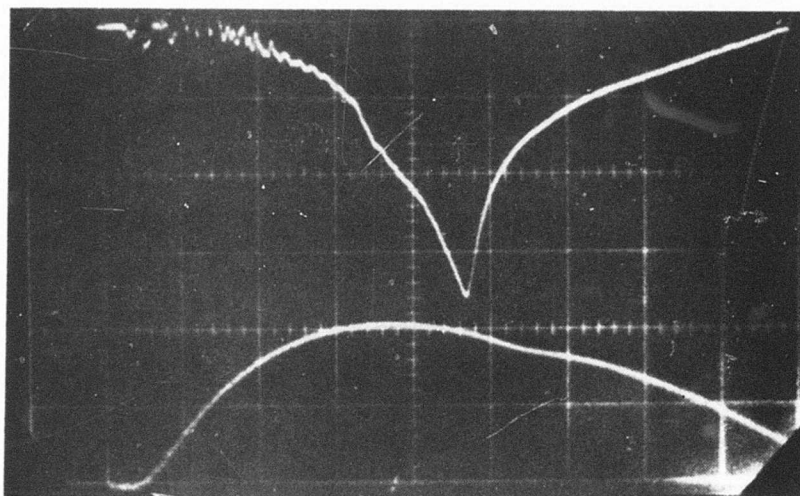
Figure 45. Time Variation of $E_\theta$ at Midplane (Upper Trace) and Circuit Current for 16 cm Radius - 0.5 μsec Sweep
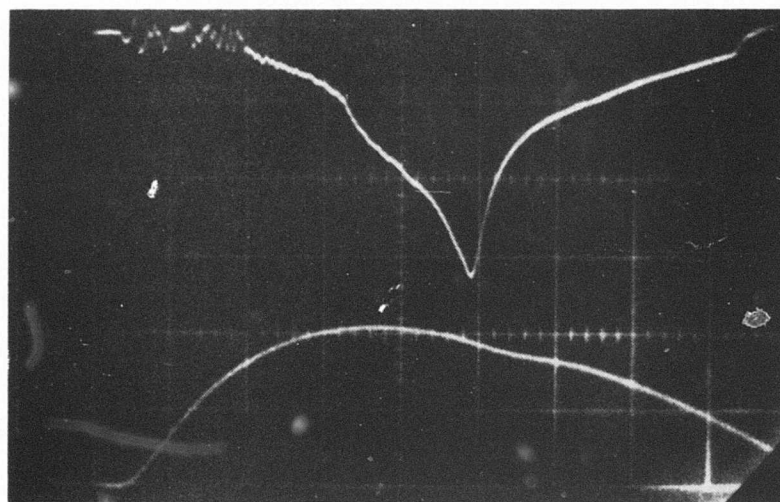


Figure 46. Time Variation of $E_\theta$ at Midplane (Upper Trace) and Circuit Current for 17 cm Radius - 0.5 μsec Sweep
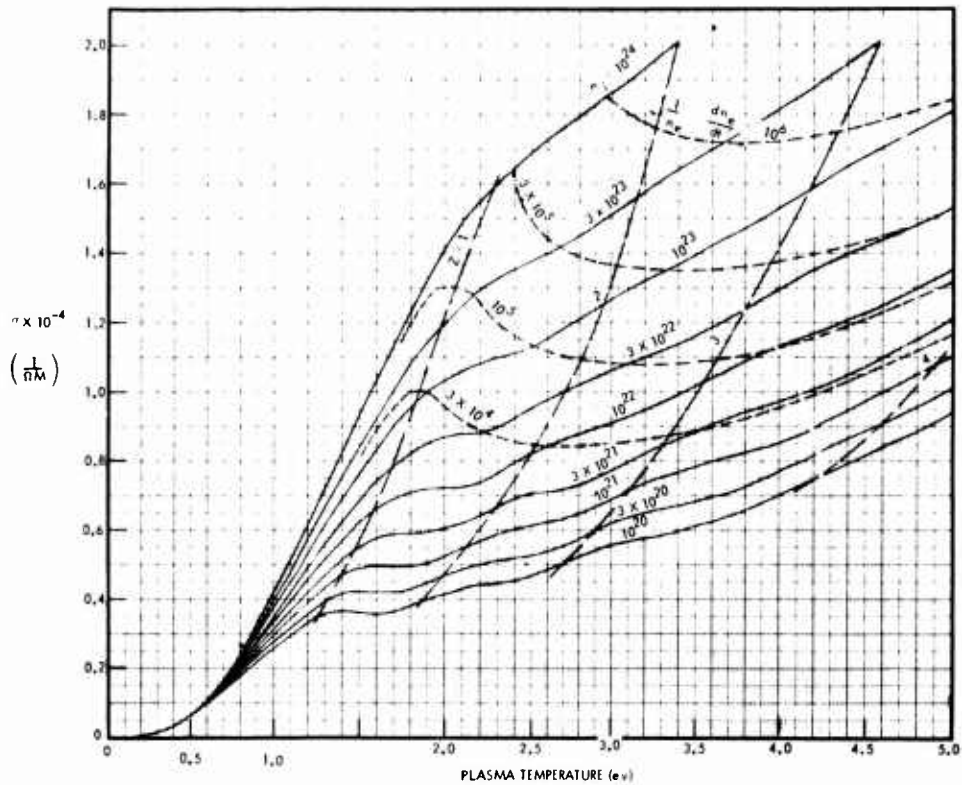
Figure 47. Equilibrium Properties, Radiative Recombination
Rate and Conductivity for Argon

noted that the outward traveling magnetoacoustic wave originates at
2.2 μsec when $j_\theta$ reaches a minimum and the break in the downward
slope of $E_\theta$ occurs. It is also noted that there are two events (1.4 and
2.1 μsec) producing abrupt loss in conductivity and each is accompanied
by an abrupt increase in the slope of $E_\theta$.

The highest conductivity occurs at 1.4 μsec, just before the first
sudden drop. The value at this time is $\sigma = 1.95 \times 10^4$ per $\Omega M$. According
to Figure 47 this requires both high temperature and high density.

The spectroscopic determination of temperature indicated values as
high as 5 ev at later times. Values at least this high must also exist near
1.4 μsec to explain the measured conductivity. If the midplane density is
assumed to increase from the fill density ($1.6 \times 10^{22}$) to $10^{23}$, the temper-
ature would be 5.5 ev and the plasma would be 3.5 times ionized. This
density increase represents a six-fold compression.

The events at 1.4 and 2.1 μsec are regarded as the arrival of two different mass layers corresponding to doubly and singly charged ions. The ratio of arrival times is about $\sqrt{2}$ as would be expected according to this argument.

After collision the conductivity can be decreased by cooling and by rarefaction (density reduction due to bounce-back after collision). It is interesting to examine these possibilities for the two collisions.

It is assumed on the basis of the relative losses of conductivity in Figure 41 that the mass involved in the second collision is twice that involved in the first one. A six-fold density increase at 1.4 μsec corresponds to compression of the fill gas within 6 mm of the midplane to a final thickness of 1 mm. Since the coil-to-coil spacing was 36 mm, this means that 1/6 of the initial mass has arrived to within 1 mm of the midplane at 1.4 μsec. At this time 1/3 of the remaining mass, carried by the fast mass layers, reaches the midplane and the other 2/3 arrives at 2.1 μsec. In terms of the total mass initially between the coils at 16 cm radius, 17% is compressed to the midplane by 1.4 μseconds, 28% more collides with this 17% at 1.4 μsec and the remaining 55% arrives at 2.1 μsec.

From Spitzer's equilibration times, ion-ion equilibration occurs in less than 1 nanosecond and ion-electron equilibration in less than 10 nanoseconds. Consequently equilibrium can be assumed for all of the data.

The equilibrium properties just after collision at 1.4 μsec are calculated from an energy balance that equates the thermal and ionization energies of both the initial and incoming masses, plus the kinetic energy of the incoming mass, to the thermal and ionization energies of the mass after collision. The results in Table 1 were obtained from this calculation:

Table 1. Plasma Properties at Midplane for 16 cm Radius and 1.4 μsec

|  | $n_i$ (per $M^3$) | T (ev) | Z | $\sigma$ (per $\Omega M$) |
|---|---|---|---|---|
| Incoming mass | $10^{23}$ | 3.0 | 2.0 | $1.3 \times 10^4$ |
| Before collision | $10^{23}$ | 5.5 | 3.5 | $1.95 \times 10^4$ |
| After collision | $1.5 \times 10^{23}$ | 5.2 | 3.5 | $1.95 \times 10^4$ |
| After rarefaction | $4 \times 10^{22}$ | 4.6 | 3.0 | $1.5 \times 10^4$ |

The ion density is found as a dependent variable in this calculation. The energy conservation approach defines a relation between plasma temperature and ionization level after collision. This relation, with the one specified by Figure 47, determines unique values of Z and T for the observed conductivity of $1.5 \times 10^4$. The ion density is then read from the location on the map determined by Z and T.

The ion density after collision is 25% of that before collision in spite of the additional mass carried by the colliding layers. This is consistent with the picture of a strong rarefaction, due to bounce back after collision, which launches the magnetoacoustic wave detected by the magnetic field probe.

The reduction in midplane temperature shown in Table 1 occurs without energy loss (i.e., without radiative cooling). It results principally from the increased ionization level of the incoming mass.

The same analysis was made at 2.1 μsec with the results shown in Table 2.

For this case the ion density is very low after collision indicating a much stronger rarefaction, which is consistent with the appearance of a stronger outgoing Alfvén wave at this time than at 1.4 μsec. It is this rapid decrease in ion density caused by the bounce-back after collision that accounts for the large and sudden loss in conductivity.

The current density maximum in Figure 41 is reached just before the rarefaction begins. The sharpness of the peak indicates a sharp

Table 2. Plasma Properties at Midplane for 16 cm Radius and 2.1 μsec

|  | $n_i$ (per $M^3$) | T (ev) | Z | σ (per $\Omega M$) |
|---|---|---|---|---|
| Incoming mass | $10^{23}$ | 3.0 | 2.0 | $1.3 \times 10^4$ |
| Before collision | $2.6 \times 10^{23}$ | 3.5 | 2.3 | $1.6 \times 10^4$ |
| After collision | $1.5 \times 10^{23}$ | 3.6 | 2.5 | $1.5 \times 10^4$ |
| After rarefaction | $4.5 \times 10^{21}$ | 3.0 | 2.6 | $0.8 \times 10^4$ |

density gradient at the trailing edge of the mass layer. The reason for this is that the mass arriving from 1.95 to 2.05 μsec supplies the momentum influx needed to maintain high density at the midplane during collision. When this momentum influx ceases the rarefaction develops radidly. The maximum in $E_\theta$ occurs later than the $j_\theta$ minimum because of increased magnetic field diffusion speed at the lower conductivity in the rarefied plasma.

After the rarefaction is over, conditions at the midplane from 2.2 to 2.7 μsec resemble those during the initial compression from 0.8 to 1.4 μsec. The conductivity again rises resulting in an increase in current density even though $E_\theta$ continues to decrease. The plasma is ohmically heated to about 3.8 ev according to the spectroscopic data and the rising conductivity indicates one and one-half decades increase in ion density to about $3 \times 10^{23} M^3$ at 2.7 μsec. As the ion density increases the electron density e-fold rate rises to about

$$- \frac{1}{n_e} \frac{dn_e}{dt} = 10^6 \text{ per second}$$

Therefore

$$\frac{dn_e}{dt} = - n_e 10^6$$

and assuming an average radiated energy of 30 ev per recombination, the power radiated in the free-bound continuum is

$$P = 30 (1.6 \times 10^{-19}) 10^6 n_e = 4.8 \times 10^{-12} n_e$$

or for $n_e = 3 \times 10^{23} M^3$ at maximum compression,

$$P = 1.44 \times 10^{12} \text{ watts/} M^3$$

This is four times the ohmic power at this time.

The radiating volume at this time is a 1 mm thick annulus with a 15 cm ID and a 35 cm OD, or $8 \times 10^{-5}$ $M^3$. The radiant power is therefore $113 \times 10^6$ watts at 2.7 μsec when the recompressed plasma reaches maximum conductivity.

According to Table 1 and Figure 47, the e-fold rate at the first conductivity peak (1.4 μsec) is also about $10^6$ indicating a comparable continuum radiation at that time. However, when the more massive current sheet arrives, the estimated conditions shown in Table 2 indicate a recombination rate less than half the values at 1.4 and 2.7 μsec. Yet it is at this time (close to 2 μsec) when the intense continuum radiation was observed in the spectroscopic and streak data.

It follows that the ion density immediately after collision must be about a decade larger than the value shown in Table 2, with an e-fold rate of about $3 \times 10^6$ per second. This suggests that the bounce-back following the fast ion collision at 1.4 μsec returns in phase with the slower ion collision at 2.1 μsec to produce a higher density than was estimated by the steady inflow model used to calculate the conditions listed in Table 2.

### 3.1.7 Radial Plasma Motion

Radial plasma motion, inferred from arrival times, was detected by both the azimuthal and axial electric field probes. The $E_\theta$ feature consisted of a propagating step and the latter was a sharply defined spike in $E_z$ as illustrated in Figure 48. Arrival times for both features, plotted in Figure 49, indicate that they belong to the same radially propagating structure. This structure is defined at a radius as small as 17.5 cm (only 1.5 cm outside of the neutral radius) where it already has a high initial velocity. This velocity is constant over a 2 cm wide annular region (from 16.5 to 18.5 cm radius) and for 0.3 μsec (from 1.6 to 1.9 μsec).

The possibility of this event being an Alfvén wave is ruled out by a consideration of the axial magnetic fields shown in Figure 39. For a constant wave speed from 17.9 to 18.6 cm radius, the ion density would be
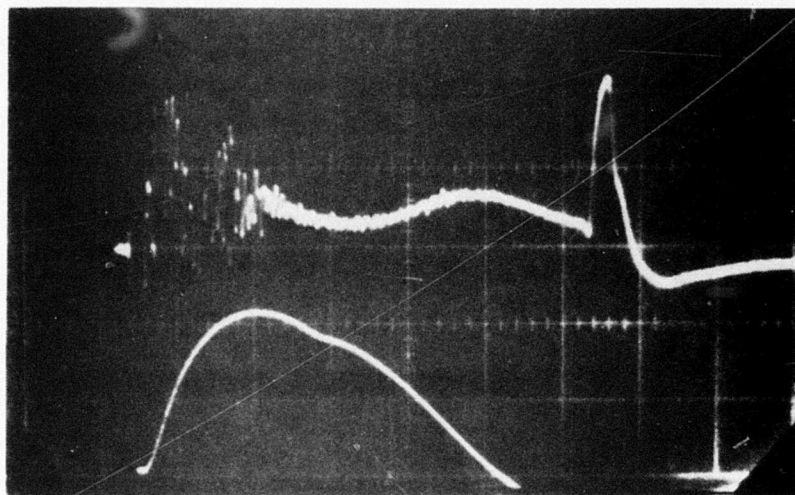
Figure 48. Radially Propagating $E_r$ Structure, R = 24 cm, 1.0 $\mu$sec/cm Sweep



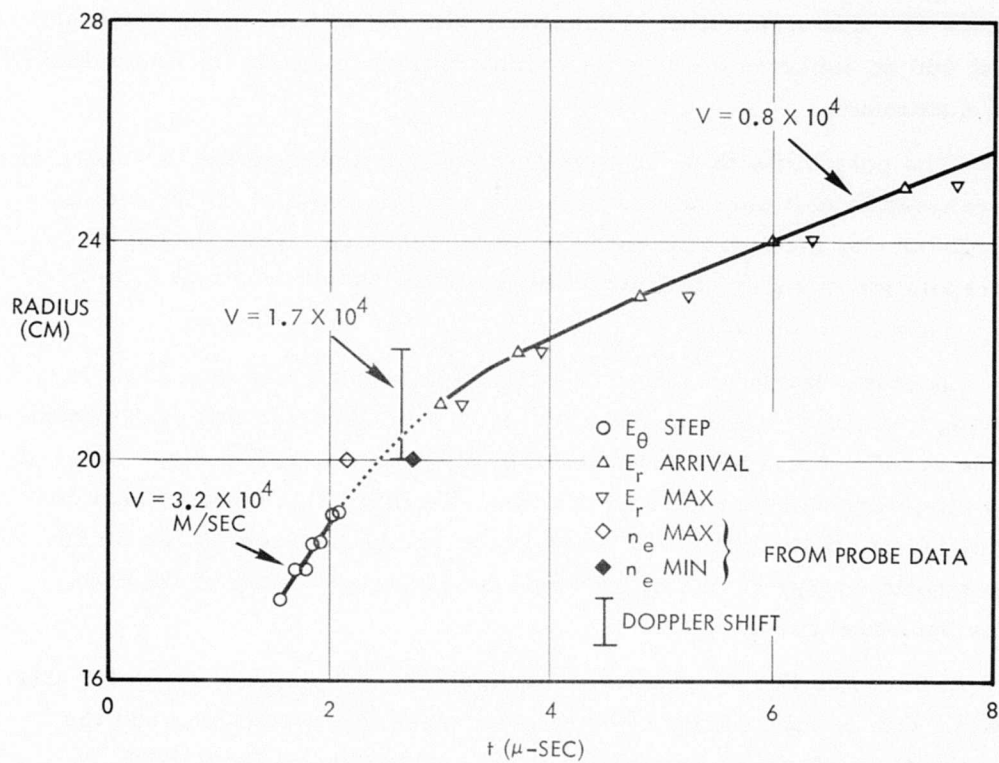Figure 49. Arrival Time for Azimuthal and Axial Electric Field Features

required to increase from $4 \times 10^{18}$ to $1.5 \times 10^{20}$ per $M^3$. Both the magnitude and the radial variation are far from plausible. Evidently this radially propagating feature represents a mass motion of substantial velocity that develops before collision of the slow more massive layers.

An estimate of the radial density distribution can be obtained from the relation

$$n_e = \frac{j_\theta \, B_z}{e \, E_r}$$

The probe data required for this calculation are plotted in Figure 50 at 20 cm radius and the resulting electron density distribution is shown in Figure 51.

The times for maximum and minimum electron density are plotted in Figure 49. The latter time agrees well with the arrival of $E_r$ maximum as should be expected since $n_e$ is a minimum when $E_r$ (in the denominator) is a maximum.

The possibility that the maximum and minimum events in Figure 51 correspond to collision and bounce-back, as observed at 16 cm radius, is ruled out by the fact that collision of the massive layers (based on extrapolation of collision times at other radii) should occur at 2.6 $\mu$sec i.e., near $n_e$ minimum.

It seems fairly certain that a thin high density ring of plasma is moving radially outward at $3.2 \times 10^4$ M/sec in the outer few centimeters of the accelerator. It is about 3.3 mm thick (in the radial direction). If this ring were 3.3 mm thick in the axial direction also it would contain about 1/4 of all the initial fill mass in the region between 16 and 20 cm. The kinetic energy of this mass would be 56 joules, or 4% of the capacitor bank energy.

There are two acceleration mechanisms that might account for this effect. One is the radial pressure gradient of the heated ions and the other is the $j_\theta \, B_z$ electromagnetic force. An order of magnitude
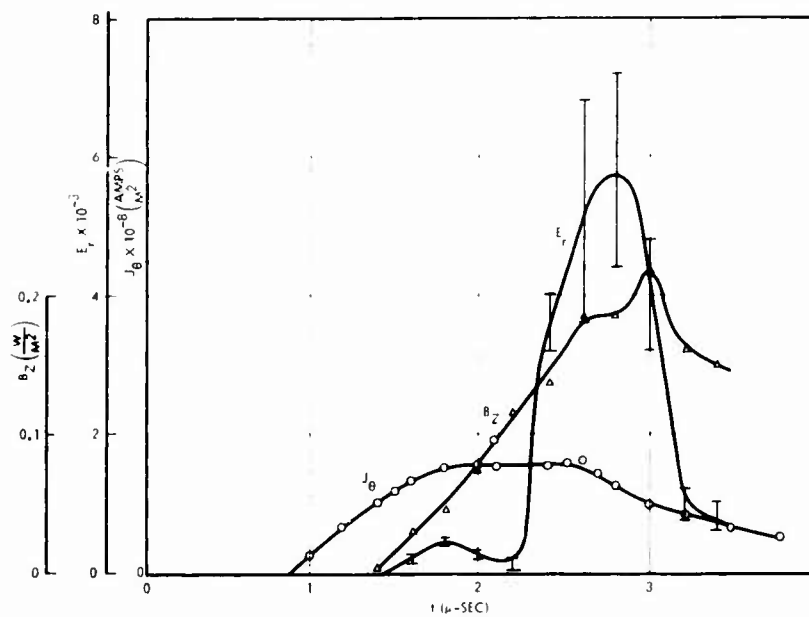
56

Figure 50.   Time Variation of $j_\theta$,  $B_z$  and $E_r$  at 20 cm Radius
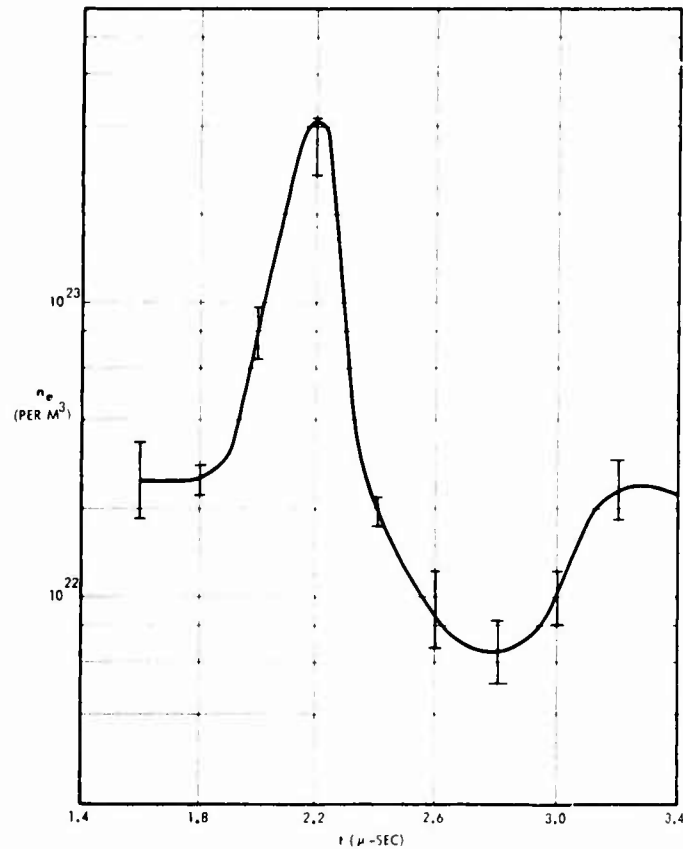


Figure 51.   Electron Density Variation with Time at 20 cm Radius

estimate can be made to determine whether either of these mechanisms is large enough to account for the observed radial velocity.

For the electromagnetic force to produce the observed velocity at a radius as small as 17.5 cm, the acceleration would have to occur between 16 and 17.5 cm where $B_z$ has the required direction. However, $B_z$ is nearly zero in that region for the first μsecond at which time the plasma has advanced about 1 cm axially. Therefore only 0.4 μsec is available for outward acceleration while the plasma moves from Z = 1 cm to the midplane at Z = 1.8 cm at a speed of 1.8 cm/μsec. An upper limit of 0.04 for $B_z$ is assumed based on data at 18 cm, and a corresponding upper limit for $j_\theta$ of $10^8$ is used based on data at 16 cm. Assuming the ion density to be equal to the fill density, $n_i = 1.6 \times 10^{22}/M^3$, the radial acceleration cannot be greater than

$$a = \frac{j_\theta \, B_z}{n_i \, M_i} = \frac{0.04 \times 10^8}{(1.6 \times 10^{22}) \, 6.7 \times 10^{-26}} = 3.7 \times 10^9 \text{ M/sec}^2$$

At the end of 0.4 μsec, this produces a velocity of only $0.15 \times 10^4$ M/sec, or about 20 times less than the observed velocity. Consequently the electromagnetic contribution to radial acceleration is ignorable for a time as early as 1.6 μsec.

An upper limit can be placed on thermal pressure gradient acceleration by using values from Table 1 just before collision where $n_i = 10^{23}/M^3$ and the electron density is $3.5 \times 10^{23}/M^3$, giving a total particle density of $4.5 \times 10^{23}/M^3$. This electron density compares well with value calculated from the probe data at 20 cm radius, shown in Figure 51.

An estimate of the density gradient can be made by assuming it to equal to that corresponding to the forward slope of the distrubution in ure 51. The leading edge passes a fixed position (i.e., the density creases from 0.4 to $4.0 \times 10^{23}$) in 0.1 μsec at a velocity (from Figure 49) of $3.2 \times 10^4$ M/sec. The corresponding thickness is therefore

$$\delta = Vt = 3.2 \times 10^4 \, (10^{-7}) = 0.32 \text{ mm}$$

The pressure gradient is therefore

$$-\frac{dP}{dr} = kT \frac{dn}{dr} = (1.38 \times 10^{-23})(5.5 \times 11605) \frac{4.5 \times 10^{23}}{0.32 \times 10^{-3}} = 1.24 \times 10^9$$

The radial acceleration is

$$a = \frac{-\frac{dP}{dr}}{n_i \, M_i} = \frac{1.24 \times 10^9}{10^{23} \, M_i} = 1.85 \times 10^{11}$$

giving a velocity of $1.85 \times 10^4$ after $10^{-7}$ seconds.

This is about 60% of the observed radial velocity, indicating that the radial plasma expulsion is due to thermal pressure stresses and not to electromagnetic forces.

The appearance of the pressure gradient force as the important accleration mechanism for early times in this magnetic field annihilation experiment was unexpected. Ordinarily electromagnetic forces in plasmas are much greater than pressure forces. In this device, however, two features combine to produce an acceleration similar to a shaped charge explosion. One is the high density produced in the axial pinch near the coil midplane and the other is the progressively slower axial speed of the plasma outside of the neutral radius. The first feature produces high density and the second produces a high radial density gradient.

An independent measurement of the plasma radial velocity was made by observing the Doppler shifted wavelength of the 4806 Å line. The results are shown in Figure 52 and the arrival time and velocity are plotted in Figure 49. The agreement with the other data is satisfactory.
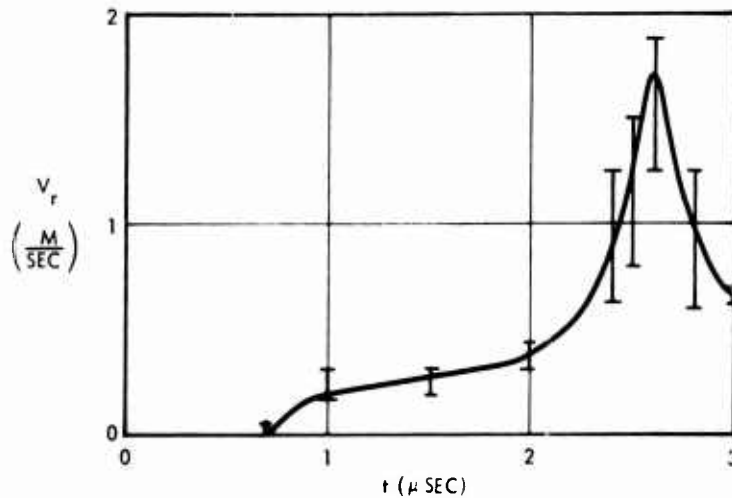
Figure 52. Radial Velocity at 22 cm Measured by
Argon 4806 Doppler Shift

An autocollimator was used for this measurement with the line of
sight tilted 20 degrees from the radial direction and passing through the
midplane between 20 and 22 cm radii. Initial attempts using radial line
of sight gave skewed distributions without a shift in the wave length for
maximum intensity. This was because of the strong background of un-
shifted light within the accelerator. It was eliminated by using a par-
tially masked aperture to exclude all light near the midplane within the
accelerator when the optical axis was tilted 20 degrees.

The initial fill mass between 16 and 20 cm radius is $4.4 \times 10^{-7}$ kg.
It was estimated that 25% of this mass is expelled by the early pressure
gradient force. Assuming all of the mass is expelled, the remainder is
ejected by the subsequent electromagnetic force at $9.1 \times 10^3$ N-sec im-
pulse (Figure 38). The results listed in Table 3 are then determined.
The pressure gradient effect contributes almost half as much impulse as
the electromagnetic force in the outer region.

The detailed study of the current sheet collision and plasma accelera-
ation in the two flat spiral coil accelerator has provided a good understand-
ing of its operation. From an initial neutral fill density of $1.6 \times 10^{22}/M^3$,
ion densities of the order of $3 \times 10^{23}/M^3$ were developed first in a very
thin annular sheet by the collision and later near the axis by the subsequent
$\theta$-pinch. Plasma conductivities ranged from $10^4$ to $2 \times 10^4$ per $\Omega M$ with

Table 3. Comparison of Radial Mass Expulsion by Thermal and Electromagnetic Forces

| Force | Mass (kg) | Mean Velocity (M/sec) | Impulse (N-seconds) | Kinetic Energy (Joules) | % Bank Energy |
|-------|-----------|------------------------|----------------------|--------------------------|----------------|
| Thermal | $1.1 \times 10^{-7}$ | $3.2 \times 10^4$ | $3.5 \times 10^{-3}$ | 56 | 1.0 |
| Electro-magnetic | $3.3 \times 10^{-7}$ | $2.7 \times 10^4$ | $9 \times 10^{-3}$ | 120 | 2.1 |
| Both | $4.4 \times 10^{-7}$ | $2.8 \times 10^4$ | $12.5 \times 10^{-3}$ | 172 | 3.0 |

corresponding electron temperatures ranging from about 3 ev before collision to 5 ev after collision. The collision launched a pair of Alfvén waves that traveled from the midplane back toward the coils and in the region outside of the neutral radius at 16 cm, a powerful thermal (pressure gradient) stress produced an explosive outward acceleration. These phenomena can be understood in terms of the current sheets commonly encountered in this type of pulsed inductive accelerator. At least in the present accelerator where the acceleration distances were of the order of three times the current sheet thicknesses, the wave-type of magnetic field annihilation acceleration was not observed. For much larger ratios of these lengths (i.e., magnetic Reynold's number), as occur in solar flares the acceleration processes might be qualitatively different. For the present purpose it seemed advisable to continue the investigation with an accelerator designed to enhance the magnetic acceleration observed in the outer region.

## 3.2 TWO-DIMENSIONAL CURRENT ACCELERATOR

The next experiment used a device that could be altered in various ways to enhance the magnetic field component orthogonal to the plasma current. Three coils wound on lucite blocks, shown in Figure 53, were used. The positions of all of the coils could be varied. For the arrangement shown in Figure 53, the large coils contribute little to the self-field required for acceleration. This field component could, however, be enhanced by tilting the large coils outward with the small coil placed at the narrow end, as shown in Figure 54. The reason for tilting the coils
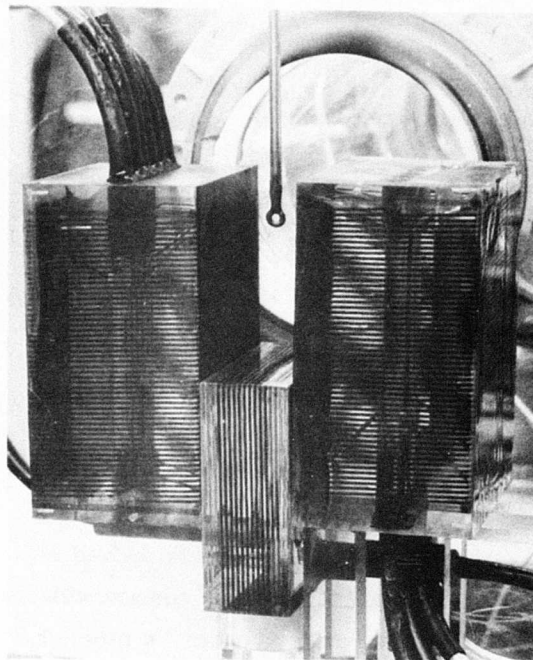
Figure 53. Coil Configuration for Field Annihilation
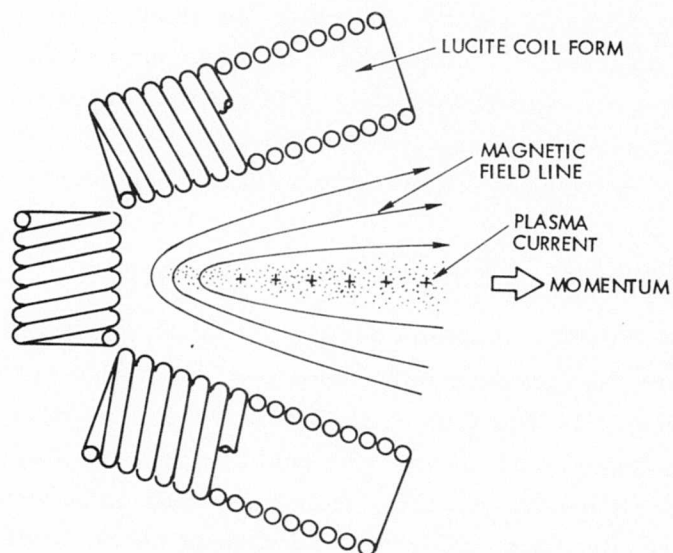Accelerator (Current density probe is
shown in plasma region)



Figure 54. Schematic of Wedge Shaped Accelerator Showing Three
Separate Coils, Plasma and Magnetic Field

is to enhance the orthogonal component of the magnetic field so that the current sustained by the annihilation of the antiparallel axial field as it diffuses into the plasma can produce a greater electromagnetic force.

The coils were enclosed by a sheet of copper wrapped closely around them, as shown in Figure 55, to confine the magnetic fields within the plasma volume. This is illustrated in the cross-sectional view of the complete accelerator shown in Figure 56. The current in each of the large coils induces a countercurrent that flows in the copper sheet and through the plasma. Thus, in spite of the fact that the current passing through the plasma terminates on metal surfaces, this device is an impulsive inductive accelerator. Current is switched into the coils by a spark gap, and the current passing through the plasma runs in closed paths around the coils. These paths comprise the plasma plus the metal sheets wrapped closely around the outside of the device.

As in all such devices, the plasma current sheets form near the coil surfaces and move away under the action of the electromagnetic forces. The time rate of inductance increase related to this motion is the useful load impedance in ohms of the accelerator circuit.
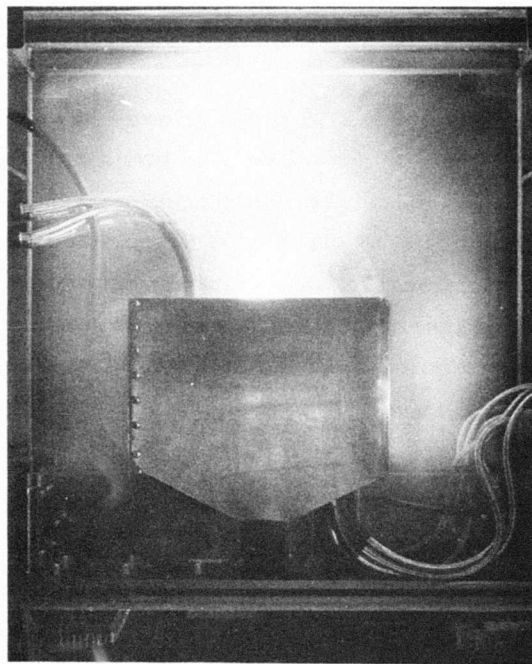


Figure 55. Photograph of Field Annihilation Accelerator During Firing (Three-Coil Configuration)

PLASMA
CURRENT

COIL
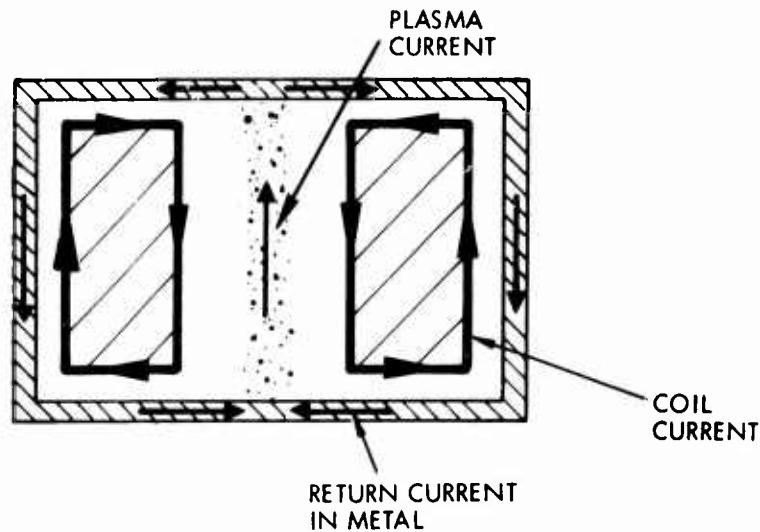CURRENT

RETURN CURRENT
IN METAL

Figure 56.   View Looking into Accelerator Exit
Showing Currents in Coil, Plasma
and Metal Enclosure

The orthogonal magnetic field component has been calculated and is shown in Figures 57 through 59 for a range of coil separations and tilt angles. The field is expressed in dimensionless form by using the axial length of the accelerator, $X_m$, and circuit current, $I_c$. This is the total current running along any one of the walls and it is the same for each of the walls.

The upper and lower coils in these figures have six 16-gauge wires connected in parallel making a total of nine turns each over the axial length of the coil. The unshielded inductance of each coil is 6 $\mu$Henrys. When the outer surface of the coil is closely covered by a sheet of metal, the inductance is a function of x, the distance between the coil and the plasma, as shown in Figure 60. For a current sheet velocity away from the surface of 1.5 cm/$\mu$sec, the motional impedance caused by the motion for a single coil is

$$Z = \frac{dL}{dx}\frac{dx}{dt} = (0.75 \times 10^{-6})\, 1.5 \times 10^{6}$$

$$= 1.1 \text{ ohms}$$

where L is the inductance of the coil when the plate (which simulates the plasma current sheet) is at the distance x.
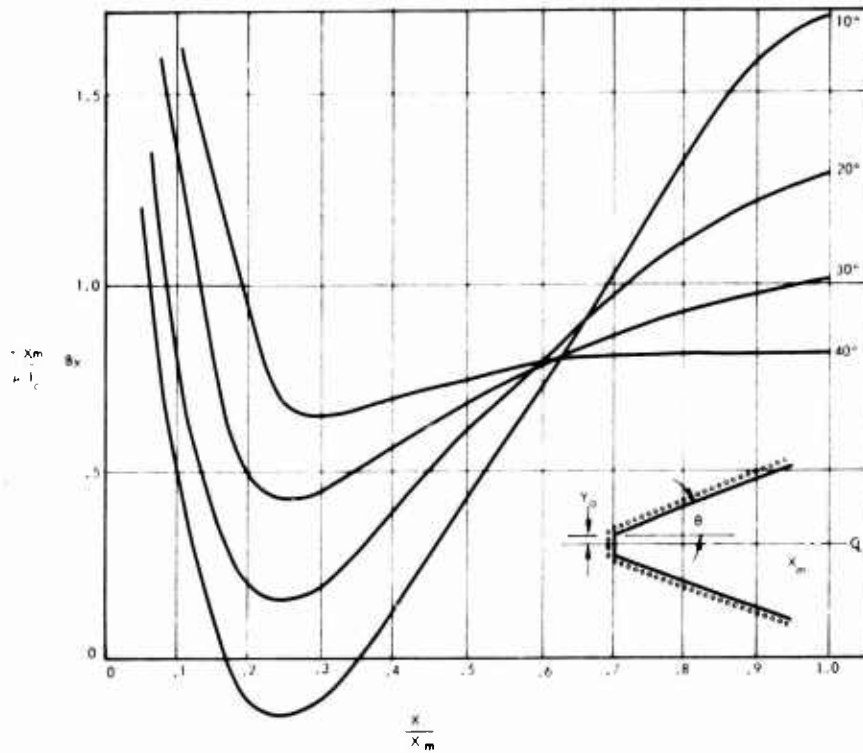
Figure 57.  Orthogonal Magnetic Field on Axis of Field
Annihilation Accelerator ($y_o/X_m$ = 0.05)
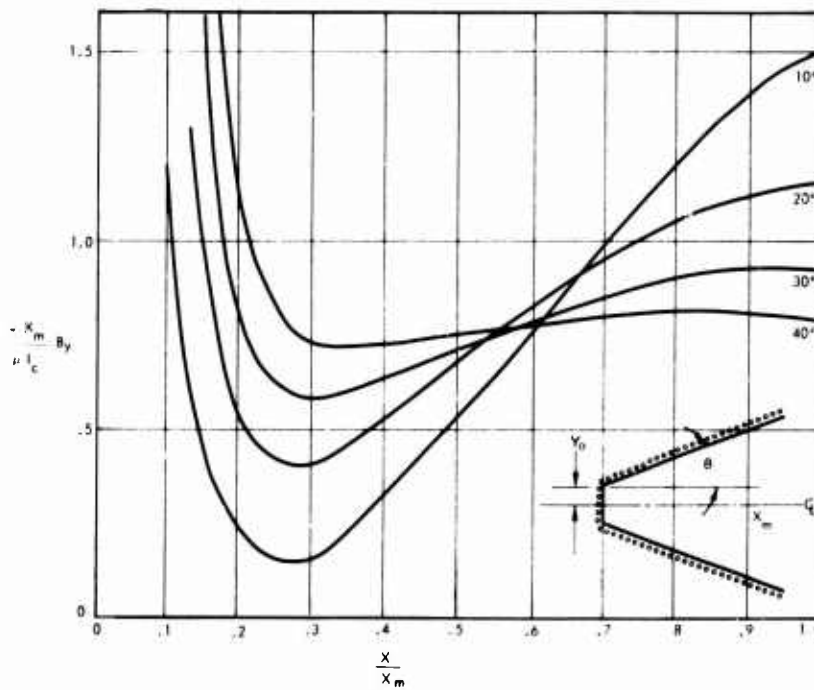


Figure 58.  Orthogonal Magnetic Field on Axis of Field
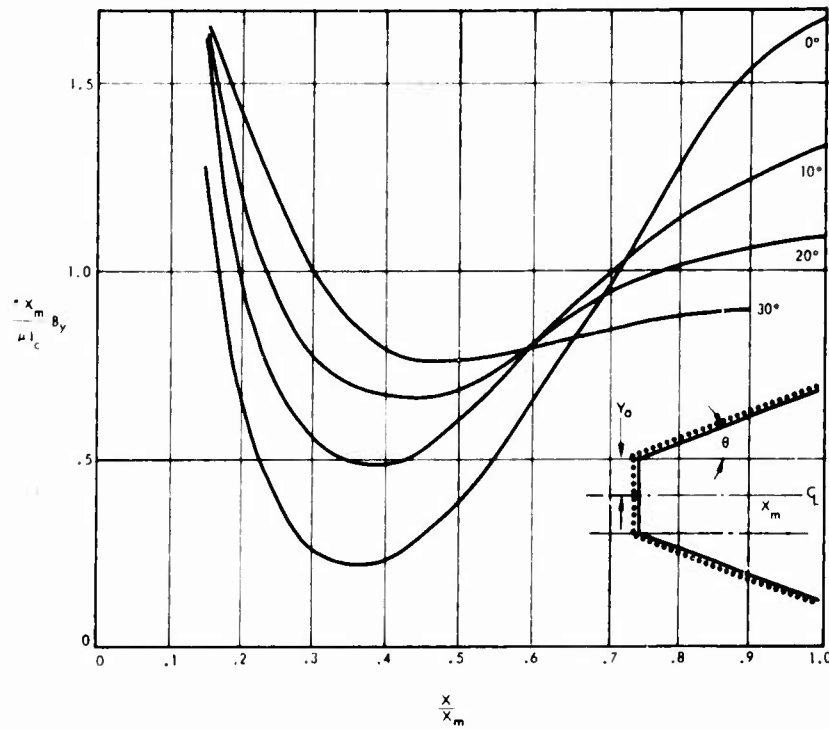Annihilation Accelerator ($y_o/X_m$ = 0.01)

Figure 59. Orthogonal Magnetic Field on Axis of Field
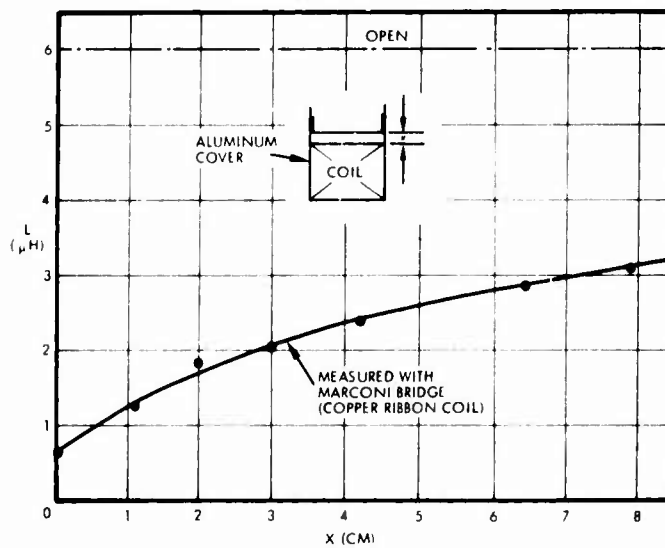Annihilation Accelerator ($y_o/X_m$ = 0.20)



Figure 60. Inductance vs Simulated Plasma Distance for
Large Rectangular Coil

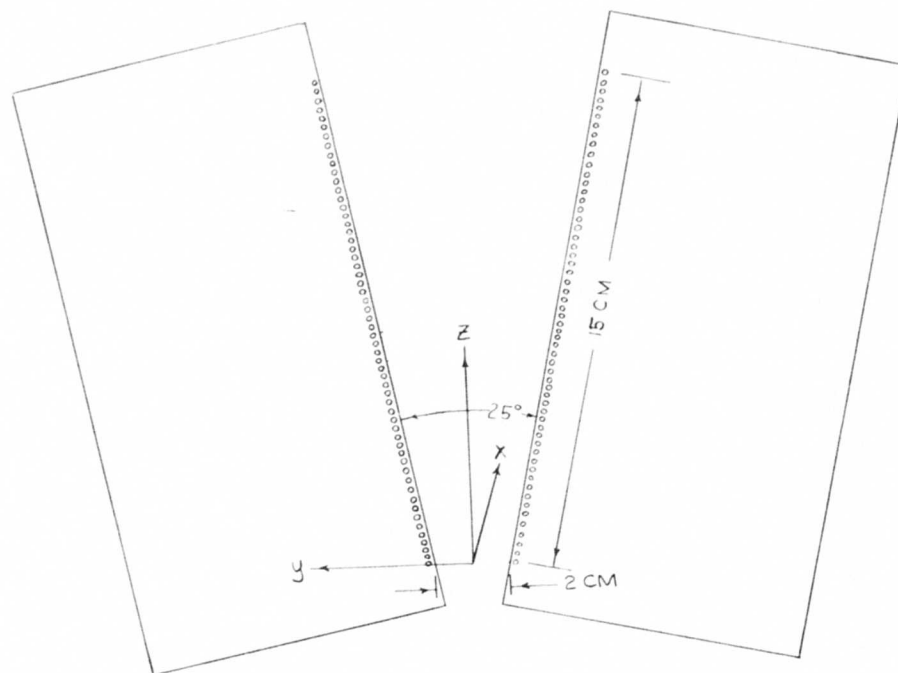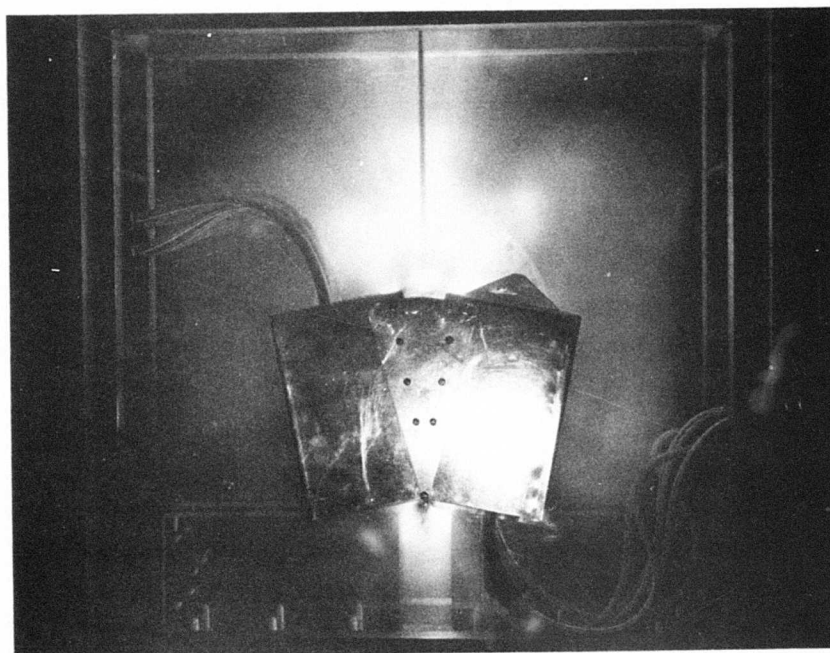Figure 61.   Accelerator Geometry and Coordinate Axes



Figure 62.   Photograph of Field Annihilation Accelerator During
Firing (Two-Coil Configuration)

67

Two 4.5 $\mu$F capacitors at 10 kv were connected to each of the coils. For a mean circuit inductance of about 2 $\mu$Henrys, this gives a maximum circuit current of

$$I_m = V \sqrt{\frac{C}{L}} = 10^4 \sqrt{\frac{9 \times 10^{-6}}{2 \times 10^{-6}}} = 2.13 \ 10^4 \text{ amp}$$

Since the coil has nine turns, $I_c = 9 \ I_m = 190,000$ amps. For a unit value of the dimensionless field shown in Figures 57 through 59, i.e.,

$$\frac{\pi X_m B_y}{\mu I_c} = 1.0$$

and for a 15-cm long coil $(x_m = 0.15 \text{ M})$

$$B_y = \frac{\mu I_c}{\pi x_m} (1.0)$$

$$= \frac{4 \pi \ 10^{-7} (190,000)}{\pi (0.15)} = 0.5 \text{ Weber/M}^2$$

which is comparable to the vacuum magnetic fields encountered in the flat spiral coil accelerators.

Quantitative experiments were carried out with the two large coils tilted as shown in Figure 61. The accelerator is shown during operation in Figure 62. This figure also shows one of the probes that was mounted above the accelerator on a traversing mechanism that could be moved along the three coordinate axes. Lateral traverses showed uniform conditions over about 80% of the length of the coils. Consequently, all measurements were made midway between the side plates, with Y and Z in Figure 61 as the only space variables.

Conventional miniature probes were used to measure the plasma current density and magnetic fields. The Rogowsky probe (mentioned in Figure 21 and shown in Figure 52) provided a direct reading of current density averaged over the middiameter of the toroidal probe coil. An overall check on probe calibration and the Rogowsky technique was made for this accelerator by independently determining the current density from the curl-H relationship which, because of the relatively weak orthogonal fields, depended only on the slope of the antiparallel Z field components in the Y direction, i.e.,

$$j_x = \frac{1}{\mu} \frac{\partial B_z}{\partial Y}$$

As can be seen in Figure 63, the agreement is good for the first 5 μsec, after which the probe reading is too low, as is also shown in Figure 21. Thus, impulse in the Z direction, computed from $j_x$ measured by the Rogowsky probe and $B_z$ from a magnetic field probe, is a little conservative.
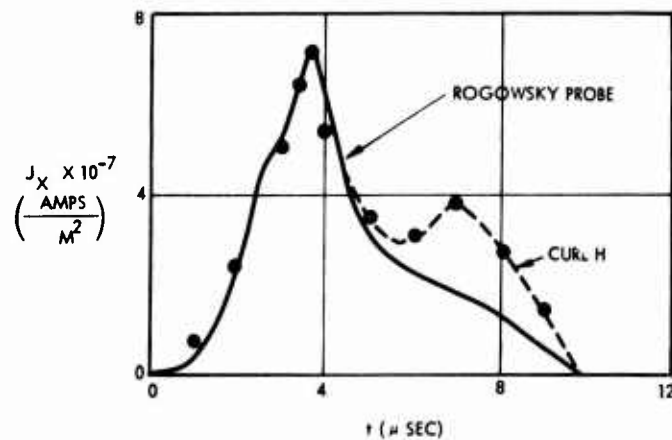


Figure 63. Comparison of $j_x$ from Rogowsky and Magnetic Field Probes (z = 6 cm, y = 0)

Figure 64 shows the first step in computing efficiency from the probe data. The current and field probe measurements for different Z positions are multiplied together and plotted against time. Each of the resulting curves is equivalent to an oscilloscope trace that would be obtained with a force density probe if such a thing existed. The symbols
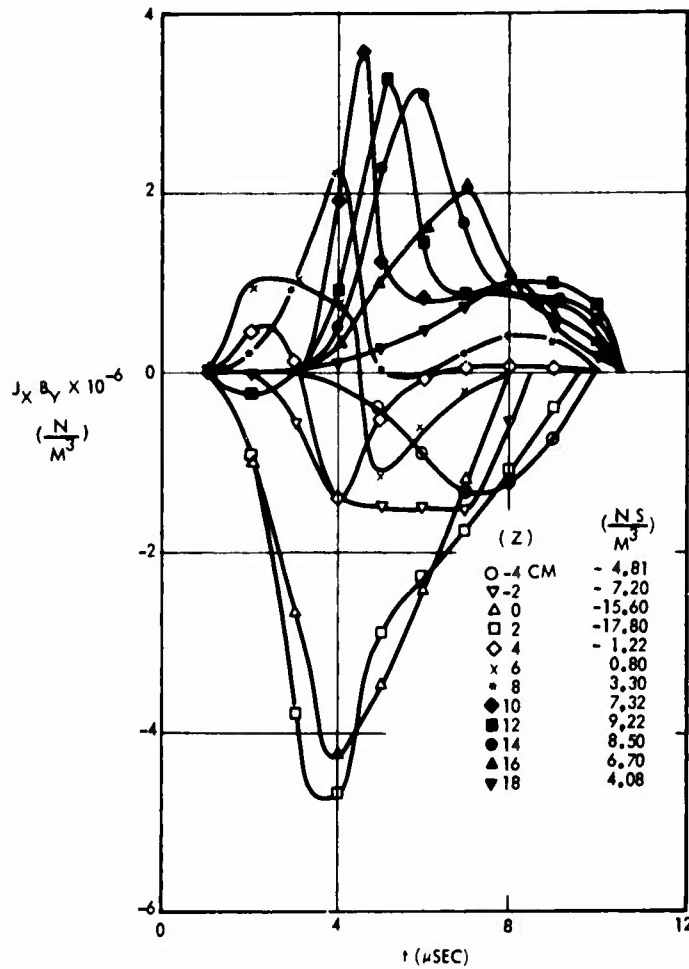
Figure 64. Force Density vs Time at Different Axial
Stations (Midplane)

identify the Z positions as well as the times for points read from the
oscilloscope traces of $j_x$ and $B_y$. The area under each curve is the
impulse density for that Z position. These values are then plotted
against Z to give the distribution of impulse density over the length of
the accelerator as shown in Figure 65. The length of the coil is also
indicated in the figure. The acceleration force is negative up to Z = 5 cm
with a negative maximum at 2 cm. The positive maximum occurs at
about 13 cm and the useful force extends 6 cm beyond the end of the
accelerator.

Figure 65 represents an upper limit on impulse in that the probe
measurements along the Z axis (Figure 64) were assumed to act over the
entire cross-sectional area at each Z location. Even with this assumption
the efficiency is low.

70
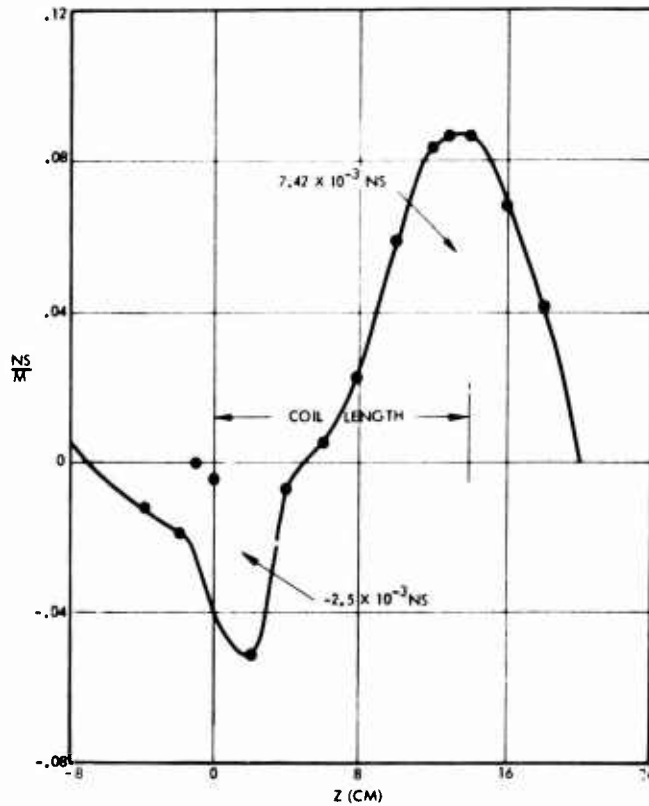
Figure 65. Axial Impulse Density Distribution

The efficiency is written again as

$$\eta = \frac{\frac{1}{2}mv^2}{\frac{1}{2}CV_o^2} = \frac{(\Delta I)^2}{2 J_o m}$$

where m is propellant mass, v is plasma velocity, C is capacitance, $V_o$ is initial capacitor voltage, $\Delta I$ is the impulse bit (mv) and $J_o$ is the energy initially stored in the capacitor. For this experiment the capacitance was 18 $\mu$F and $V_o$ was 10 kv. The total mass of argon in the volume between the coils was $1.1 \times 10^{-6}$ kg (corresponding to 0.5 torr of argon). Thus, the efficiency based on the net impulse of $4.92 \times 10^{-3}$ N-seconds (Figure 65) was

$$\eta = \frac{(4.92 \times 10^{-3})^2}{2(900)(1.1 \times 10^{-6})} = 1.2\%$$

at an $I_{sp}$ of

$$I_{sp} = \frac{\Delta I}{mg} = 447 \text{ seconds}$$

If all of the impulses were included instead of the net value only, then

$$\eta = \frac{(9.93 \times 10^{-3})^2}{2(900)(1.1 \times 10^{-6})} = 5.0\%$$

at an $I_{sp}$ of 900 seconds. Even at this ratio of $\eta$ to $I_{sp}$, the efficiency projected at the same slope to 1500 seconds $I_{sp}$, for example, would be only 8.3% as compared to the average of 15% shown in Figure 1.

Probe traverses were also run in the Y direction at Z stations of 2 and 12 cm to determine the deviation between the Y-averaged impulse density and the midplane value at y = 0. The average value was 54% for the 2 cm station and 87% for the 12 cm position. Thus, the above conclusions based on the assumption of constant force density over the cross section are valid.

The experimental studies of fairly diamagnetic plasmas accelerated by the pressure of an expanding magnetic field have shown that high current densities (of the order of 10,000 amps/cm$^2$) and good conductivity (better than 10$^4$ per $\Omega$M) are readily achieved. In the field annihilation geometry even better performance is seen as far as plasma current sheet properties are concerned. But the conversion of the field energy to kinetic energy is consistently poor for both accelerators.

The fundamental difficulty with the field annihilation accelerator appears to arise from the high conductivity of the current sheet. This can be seen by referring to Figure 66 which shows the time history of the plasma current density and the magnetic field components at Z = 12 cm on the midplane, where relatively strong acceleration was observed.

At the midplane, $B_z$ = 0 by symmetry and the rapid buildup of $B_z$ in the Y direction seen in the lower trace reflects the diamagnetic property of the current sheet. It is the upper two traces in Figure 66 ($j_x$ and

1 μs/cm
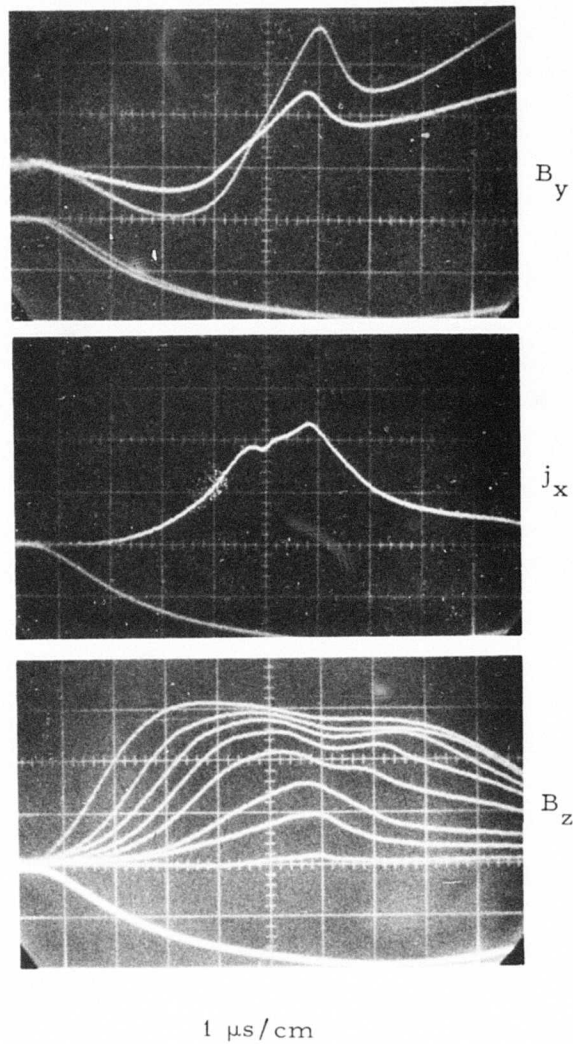
z = 12 cm

Figure 66.  Comparison of Orthogonal Magnetic Field $B_y$ and
Plasma Current Density $j_x$ at x = y = 0 and z
= 12 cm During Current Pulse. $B_z$ is also
shown for 0.5 cm increments from y = 0 to
y = 3.5 cm at x = 0 and z = 12 cm.

73

$B_y$) that show why high conductivity results in poor efficiency for the field annihilation accelerator (the two $B_y$ traces are an overlay of two shots at different oscilloscope gains). A local peak in both the orthogonal field and the current density occurs at 6 μsec and the corresponding acceleration is a maximum. The vacuum field corresponding to this accelerator geometry only arrives after 7 μsec when the plasma current density is rapidly decaying. After 4 to 5 μsec a strong plasma current has developed, but the orthogonal field remains excluded because of the low diffusion speed of that field relative to the highly conductive plasma mass. Thus, the high conductivity prevents the vacuum field from entering the plasma when the current is large and the orthogonal field arising from the vacuum field of the accelerator coil geometry cannot be effective. The argument is different for a single coil accelerator. There the inefficiency is due to the conductivity not being high enough to limit diffusion of the orthogonal field (which also drives the current in that geometry).

# SECTION IV

## PULSED BIAS FIELD EXPERIMENTS

A simple argument has been formulated to show the dependence of efficiency, for a self-field accelerator, on the diffusion limited force density. The current density j at any point

$$j = \sigma \, (E - vB)$$

where $\sigma$ is plasma conductivity, E is electric field parallel to j, v is plasma velocity and B is magnetic field perpendicular to the direction of motion.

Thus

$$E = \frac{j}{\sigma} + \, vB$$

and the input power density at the local point under consideration is

$$j \, E = \frac{j^2}{\sigma} + \, (j \, B) \, v \tag{6}$$

It is equal to the sum of the local ohmic heating and the product of the j B force times the plasma velocity. The latter term is the rate of work done on the plasma. This consists of the work of deformation plus the increase of kinetic energy. At one extreme, the "slug model" regards the accelerating mass as rigid; at the other extreme the "snowplow model" assumes impact acceleration in which the work of deformation is equal to the kinetic energy gained. The ratio of the two terms on the right side of Equation (6) is simply the magnetic Reynolds number for the accelerator. This is seen by writing the current density in terms of the Curl of H,

$$j = \frac{1}{\mu} \, \frac{B}{\delta} \tag{7}$$

where $\delta$ is the current layer thickness. Then from Equations (6) and (7) the ratio of the work term to the dissipation is

$$\frac{vB\sigma}{j} = \frac{vB\sigma\mu\delta}{B} = \mu\sigma\delta v$$

This is the ratio of the mass velocity to the magnetic field diffusion speed, which is the magnetic Reynolds number. When this ratio is of the order of 1 to 3, from 50 to 25% of the power goes into ohmic dissipation.

In the bias field concept, the magnetic field in Equation (6) is the bias field $B_b$, which is perpendicular to the acceleration direction z, while that in Equation (7) $B_z$ is parallel to the acceleration direction. The ratio of the work term to the dissipation term is then

$$\mu\sigma\delta v \ \frac{B_b}{B_z} \ = \ \frac{B_b}{B_z} \ R_N$$

The effective Reynolds number is then increased by the ratio of the bias field to the field whose diffusion drives the plasma current.

## 4.1 BIAS FIELD WITH TWO-DIMENSIONAL CURRENT ACCELERATOR

The bias field concept was tested by adding a pair of bias field coils to the two-dimensional current accelerator. The field coil geometry is shown in Figure 67. Five concentric coils were wound in grooves machined in nylon blocks. They were then encapsulated in urethane and covered with a 5-mil sheet of Mylar. As shown in Figure 68, these bias coil blocks were placed against the active faces of the two large accelerator coils. Before construction of these coils, it was verified that a good plasma discharge could be produced in spite of the greatly increased separation between the current drive coils and the plasma. Figure 69 shows the measured bias field values for a range of capacitor voltages.

The field and current configurations for this experiment are shown in Figure 70. The parallel accelerator current sheets produce the antiparallel fields across the plasma current sheet; the gradient of this field is essentially the current density. The bias field acting to the left interacts with the plasma current to produce the upward acceleration force.

Figure 71 shows both the circuit current and the plasma current density for a 10-kv accelerator capacitor voltage and a static fill density of 350 millitorr of argon. A bias field circuit capacitance of 10 μF was used with a 5Ω series-connected damping resistor to prevent ringing.
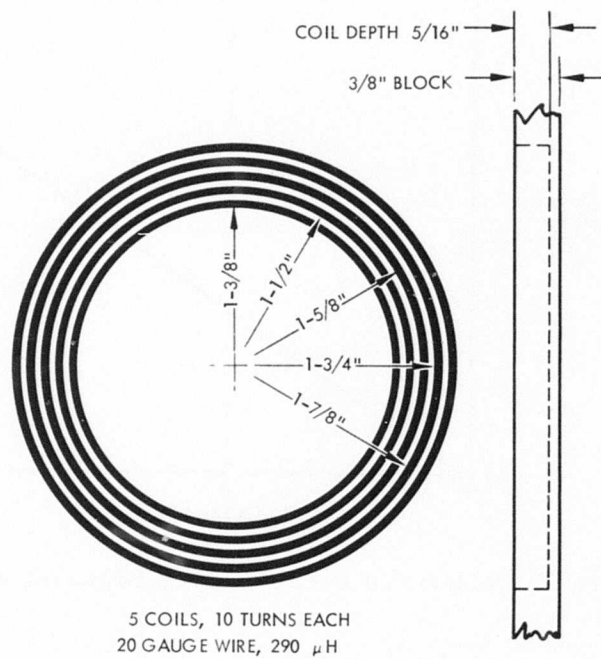
76

COIL DEPTH 5/16"

3/8" BLOCK

1-3/8"

1-1/2"

1-5/8"

1-3/4"

1-7/8"

5 COILS, 10 TURNS EACH
20 GAUGE WIRE, 290 $\mu$H
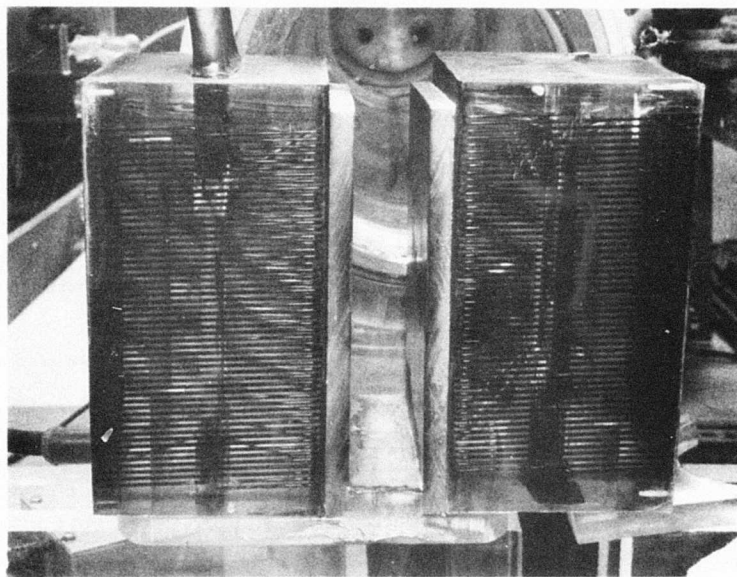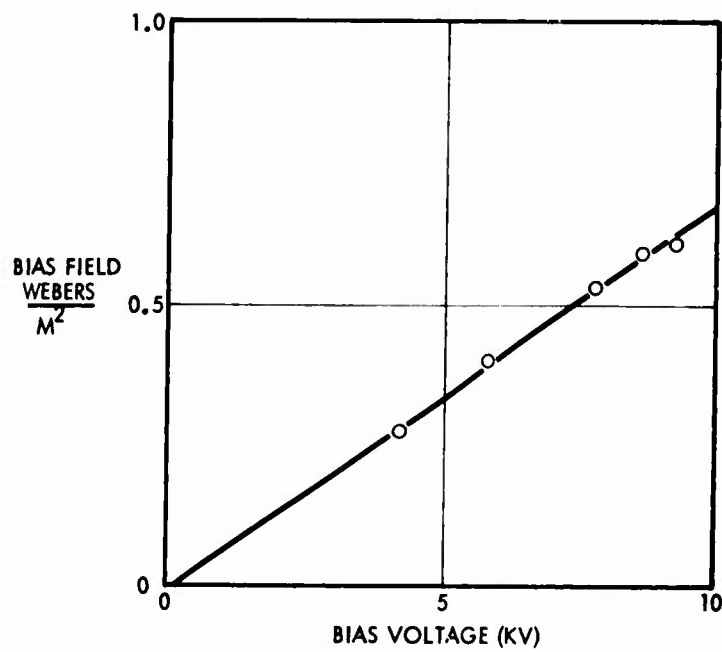
Figure 67.  Bias Coil Geometry



Figure 68.  Photograph of Accelerator Coils
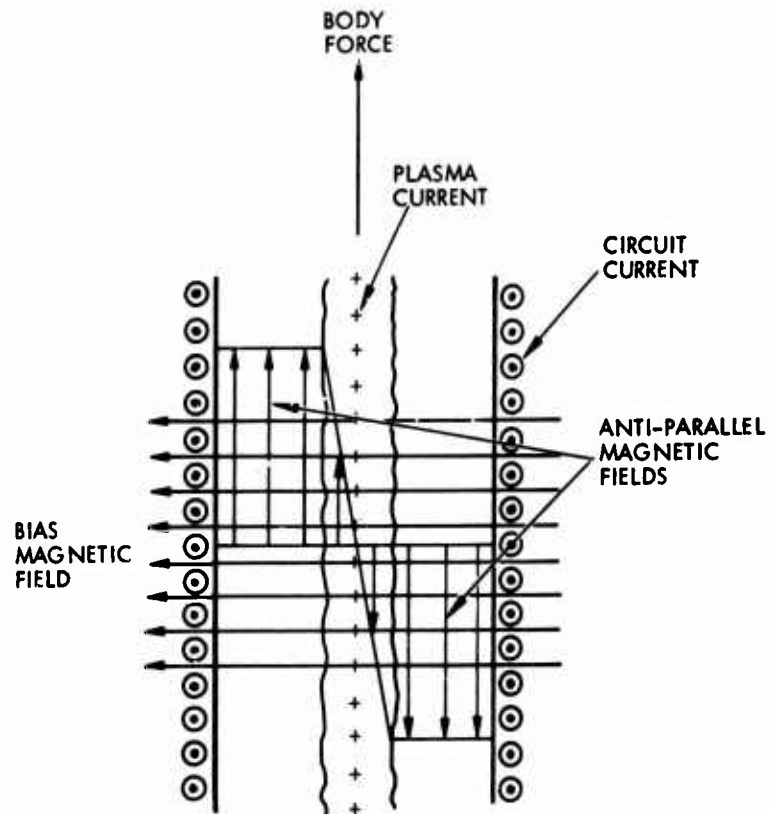
77

Figure 69. Measured Bias Field for Different Voltages



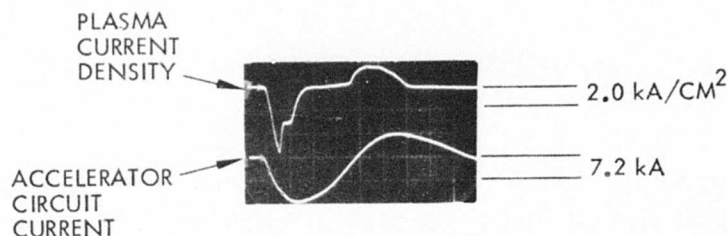Figure 70. Current and Field Configuration in Accelerator

PLASMA
CURRENT
DENSITY

2.0 kA/CM$^2$

ACCELERATOR
CIRCUIT
CURRENT

7.2 kA

Figure 71.   Circuit Current and Plasma Current Density vs Time
at Midplane (350 m torr argon,  sweep 5 μsec/cm)

For a bias capacitor voltage of 10 kv, the stored energy was 500 joules
and for the same voltage the accelerator capacitors stored 900 joules.
Using the bias field of 0.67 Webers/M$^2$ from Figure 69 and the plasma
current density from Figure 71, the force density near the center of the
bias coil and midway between the accelerator coils varies with time as
shown in Figure 72.   The integrated impulse density was 142 Ns/M$^3$.   If
the volume over which this impulse density exists was limited to the inner
diameter of the bias coil and a typical current layer thickness of 1 cm
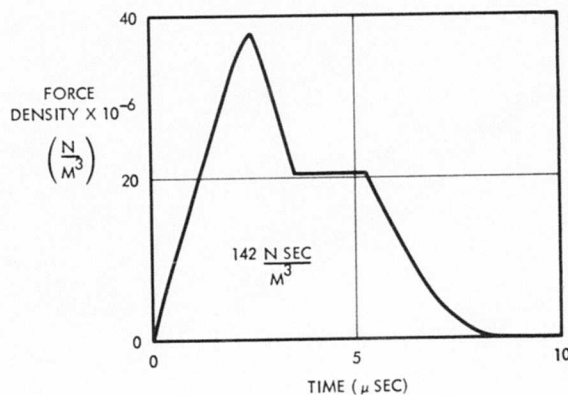were used, then

$$\Delta I = 0.069 \text{ NS}$$



Figure 72.   Time Variation of Force Density at Midplane
(350 m torr argon)

79

and with the conservative assumption that $J_o$ represents the energy stored in both capacitors,

$$\frac{\eta}{I_{sp}} = \frac{g\,\Delta I}{2\,J_o} = \left(\frac{g}{2}\right)\left(\frac{0.069}{1400}\right) = 2.4 \times 10^{-4}/\text{sec}$$

If the impulse estimated in this simplified manner were applied to a mass large enough to limit the $I_{sp}$ to 2500 seconds, the efficiency would be 60%.

## 4.2 COAXIAL ACCELERATORS

The coaxial geometry is naturally suited to a practical thruster. Figure 73 shows the plasma current drive coil concept. As in all of the previous two coil accelerators, the plasma current is driven by diffusion of antiparallel magnetic fields into the current sheet. In the coaxial geometry these fields are developed outside of the inner coil and inside of the outer coil. The antiparallel fields are not present in the vacuum
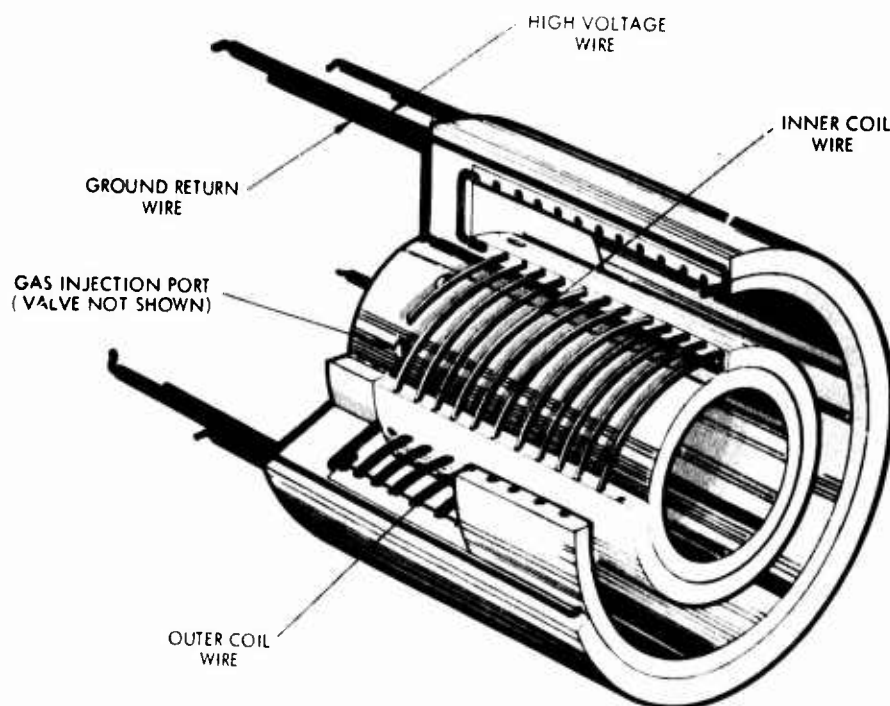


Figure 73. Perspective Showing Field Annihilation Current Drive Coils

80

fields of these coils but result from the combination of those fields with the fields associated with the plasma current. Thus diamagnetic current sheets must form close to coil surfaces early in the discharge for the coaxial coils to be an effective current generator. The development of such a discharge is one of the practical problems of the coaxial accelerator.

Another practical problem is to shape the magnetic fields in the plasma volume such that the average mass motion will be axial only. There are two parts to this problem. One is that the normal $\theta$-pinch force of the outer coil be balanced by the inverse $\theta$-pinch force of the inner coil so as to prevent radial drift of the plasma. The other is that the bias field be essentially radial.

Two axially symmetric, bias field accelerators were built and tested, both using coaxial current drive coils and an additional set of coaxial coils to produce the radial bias field. One of them used solenoidal coils with a steadily increasing wire spacing to produce a nearly uniform radial fringing field in the plasma region, while the other used four coils arranged to produce a "cusp" bias field. The bias circuits were much slower than the drive circuits in both cases so that the bias field was fully developed before firing the drive circuit. To prevent large voltages being induced in the bias coils by the fast transients in the drive coils, shorted turn shields were placed close to the bias coils.

The first axially symmetric, bias-field accelerator, designated as Mark I, had a plasma volume 1 cm wide by 6 cm long with a midradius of 5 cm. The coil arrangement is shown in Figure 74. The current drive coils are uniformly spaced but a constantly increasing spacing is used for the bias field coils; the spacing ratio of adjacent turns is a constant such that the spacing of the last pair of wires is ten times that of the first pair. The plasma volume is offset as shown to use a region of the fringing fields of the bias coil where the radial component is reasonably uniform and the axial component is small compared to the radial one.

The individual coils are shown in the exploded view of Figure 75. The inner shield can be seen but the outer one is not because it was used to support the outer bias coil during winding. The assembled accelerator
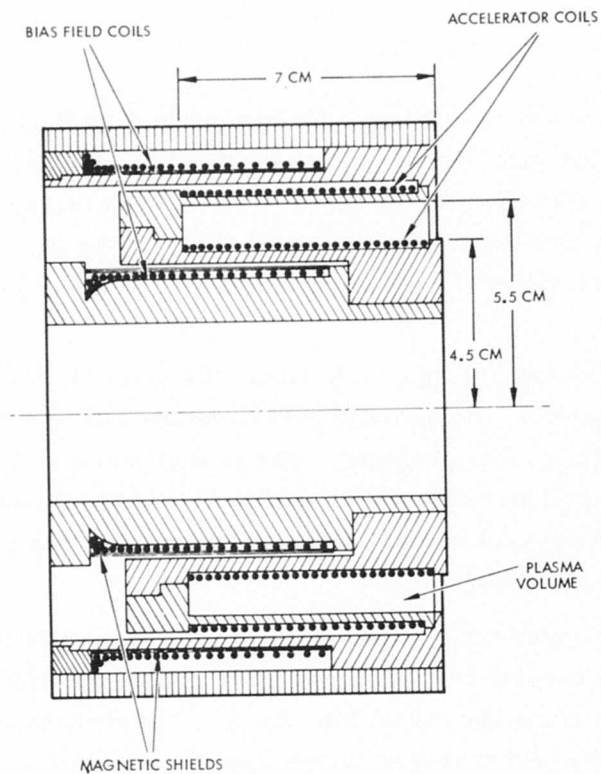
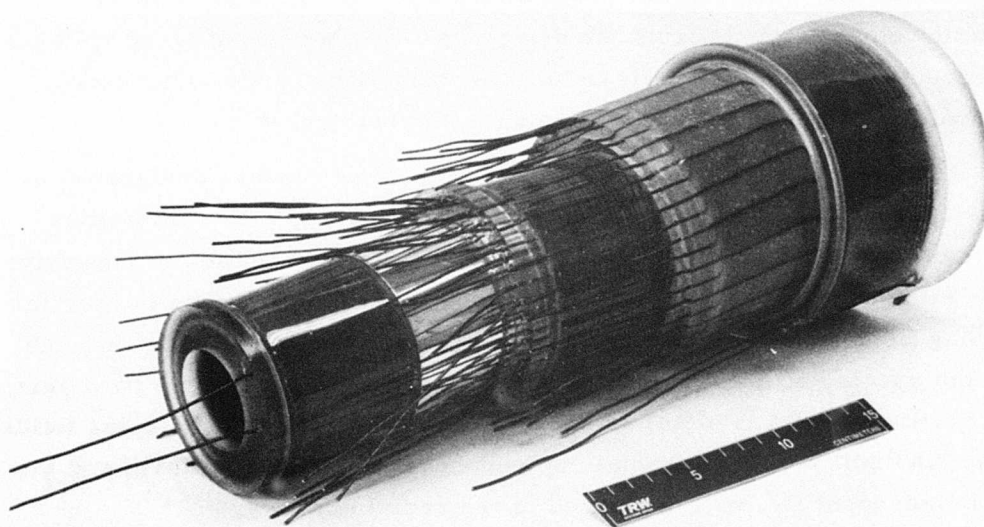Figure 74. Cross-Sectional View of Axisymmetric Accelerator



Figure 75. Exploded View Showing Bias and Drive Coils
and Shield Assembly Positions

is shown in Figure 76. The second accelerator, Mark II is shown in Figure 77. A photograph of the accelerator firing is shown in Figure 78. Shown in these photographs is a cross-shaped arrangement of four thin sheets of epoxy-fiberglass that serve to interrupt the plasma current as the plasma leaves the region of uniform radial bias field. Rogowsky probe measurements showed that this technique worked well. The annular space occupied by plasma is 2 cm wide by 3 cm long with a mean radius of 4 cm. The inner and outer bias coil radii are 2.5 and 5.5 cm and their axial separation is 6 cm. The plasma volume is centered axially and radially between the bias coils.

The long, narrow slot of the Mark I accelerator was found to be impractical because of severe probe interference with the current sheet. Also, in this accelerator the inner and outer drive coils had the same number of turns (one turn each). This may have resulted in a radially inward motion of the plasma during acceleration because of the greater inward "pinch" force from the outer drive coil as compared to the outer "inverse pinch" force from the inner drive coil. These difficulties were overcome in the Mark II design by using the wider and shorter slot and by using two turns for the inner coil with one turn, as before, for the outer coil. Probe measurements showed the axial magnetic field to be zero, at the mid-radius, at the time of maximum current.

A peculiarity of the discharge was observed during probe measurements with the Mark II accelerator which appears to indicate that an inductively applied bias magnetic field is not feasible. Figure 79 shows oscilloscope traces of the radial magnetic field at 5 cm radius for several axial positions. The circuit current (lower trace) is also shown. Zero lines for both traces were recorded for convenience. The initial bias field of 0.29 Webers/$M^2$ can be seen before the discharge starts. It is seen that the bias field is reduced nearly to zero at the time of maximum accelerator current, near the closed end of the accelerator, and it is increased to more than twice the initial bias value at the accelerator exit. This effect is caused by the current pulse induced in the shorted turn shields when the accelerator is fired. This current pulse prevents the magnetic fields from the accelerator drive coils from coupling into the bias field coils, as intended. However these closed loop currents are
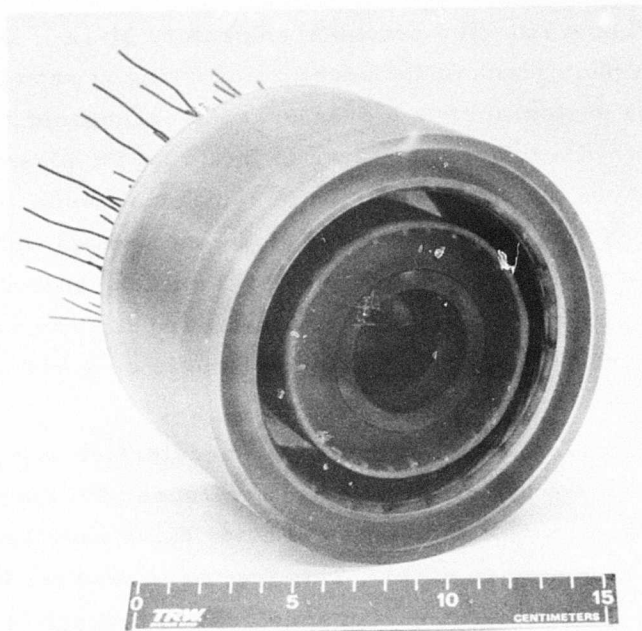
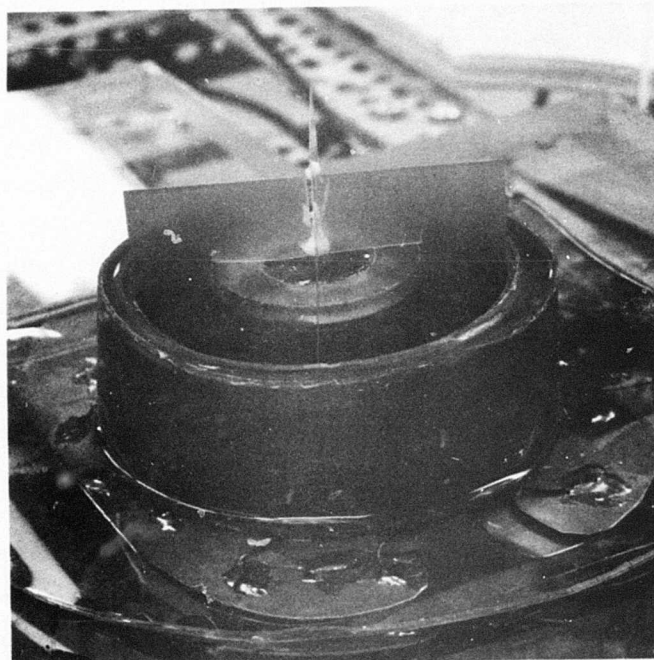Figure 76. Photograph of Completely Assembled Thruster



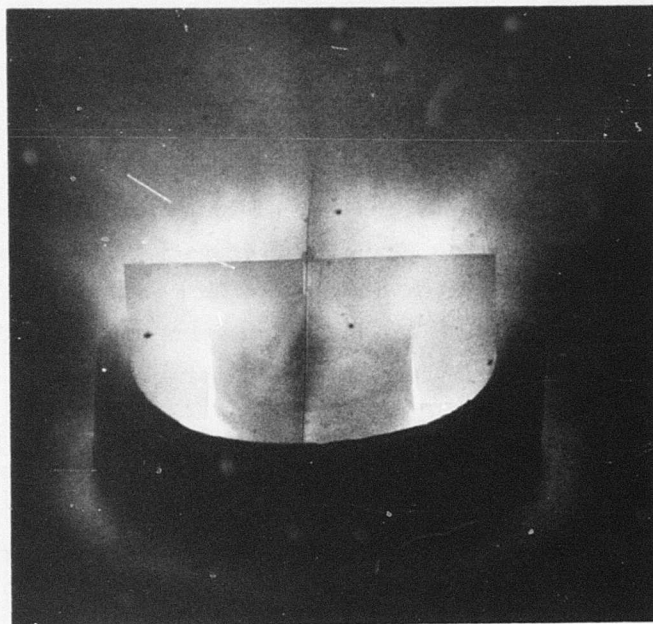Figure 77. Photograph of Mark II Accelerator

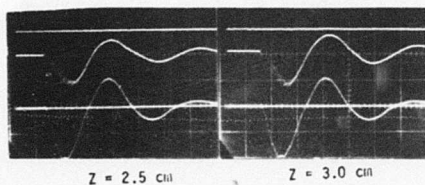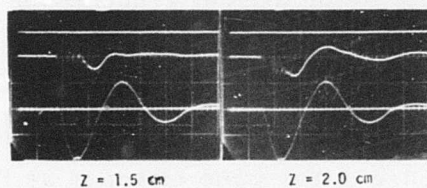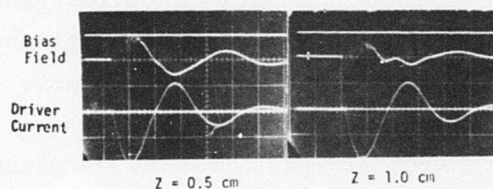Figure 78.   Photograph of Mark II Accelerator Firing



Figure 79

Radial Magnetic Field at 5-cm
Radius in Mark II Accelerator
for Different Axial Positions
(Initial Bias Field = 0.29 W/M$^2$,
I$_{max}$ = 3900 amps, 2 $\mu$sec/cm)

strong enough and close enough to the plasma volume to have a first order effect on the radial magnetic field while the plasma current is running.

Figure 80 shows the axial distribution of the first half-cycle maxima of current density, bias magnetic field and force density. The static fill density was $1/2$ torr of argon; a $2 \mu F$ capacitor charged to $15$ kv was used in the accelerator circuit ($225$ joules). This figure shows that the shield currents not only had a large effect on the radial magnetic field, but also strongly affected the plasma current as well. Thus the plasma current was large where the field was low and low (even reversed at the exit) where the field was large.

The reason for this coupling effect can be seen by referring to the schematic of the currents and magnetic fields of the Mark II accelerator in Figure 81. The drive coils produce the plasma current shown and the bias coils produce the outward directed magnetic field $B_r$. The pulsed currents in the shorted turn shields have the polarity shown, i.e., they have the same direction as the plasma current. The incremental radial fields caused by these currents, $\Delta B_r$ in the figure, oppose the bias field at the closed end and aid it at the open end. This effect is readily apparent when it is recognized that all currents induced by the accelerator coil current must be in the opposite direction as the coil current. Another equally apparent observation is that each pair of concentric shield coils acts like a flat coil accelerator which drives the plasma away from it by inducing a plasma current counter to its own current. Thus the transient fields induced by the shield currents produce an electric field opposite to that induced by the drive coil electric field, thereby reducing the plasma current density.

The Mark I accelerator configuration, shown in Figure 82, is also affected adversely by its shield currents although the details are slightly different. Again, the shield currents are in the same direction as the plasma current and therefore induce an opposing electric field. The $\Delta B_r$ effect is opposite to that in the Mark II accelerator. The radial field is increased near the closed end and reduced near the open end.

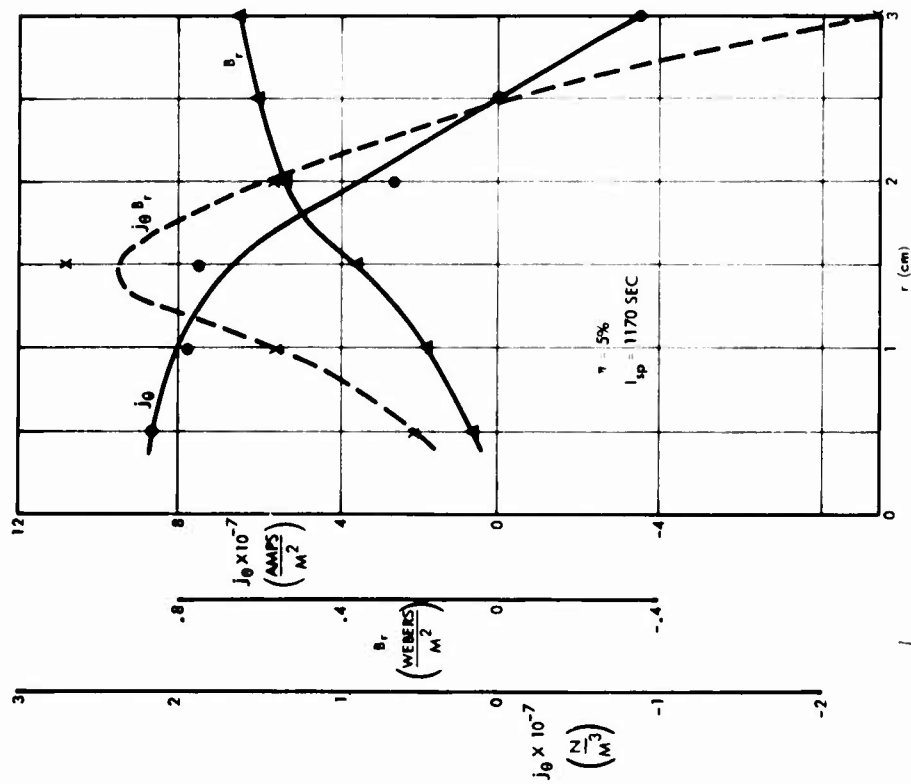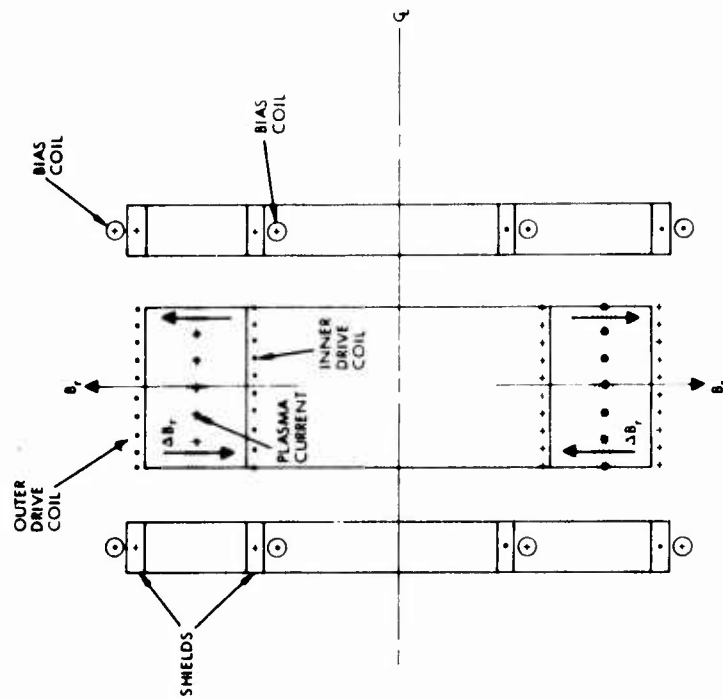Figure 81. Schematic of Currents and Magnetic Fields in Cusp Bias Field Accelerator – Mark II



Figure 80. Axial Variation of Current Density and Radial Magnetic Field Maxima and Force Density – Mark II
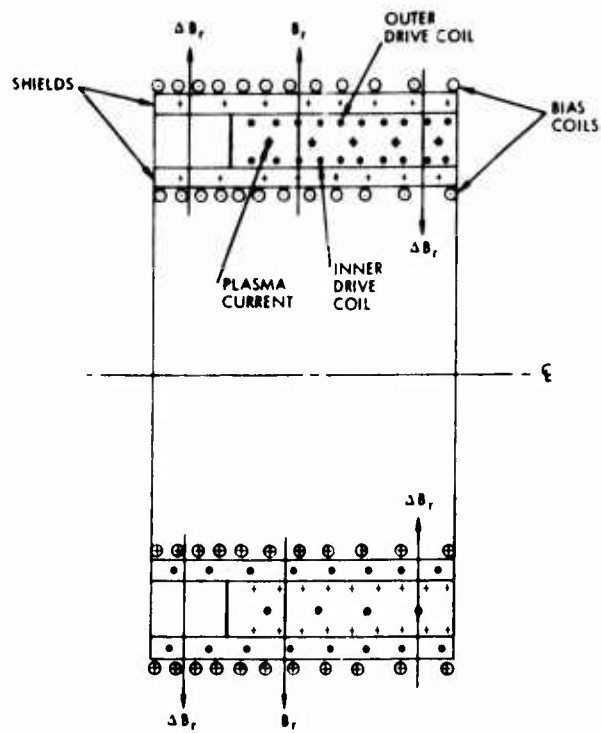
Figure 82. Schematic of Currents and Magnetic Fields
in Fringing Bias Field Accelerator — Mark I

# SECTION V

## CONCLUSIONS

1. For the plasma accelerators studied in this program, having an argon fill density of 0.5 torr and a magnetic Reynolds number of the order of 3, acceleration by the direct conversion of magnetic field energy to plasma kinetic energy was not observed.

2. Electron temperatures as high as 5 eV were produced for short periods, with corresponding plasma conductivities of $2 \times 10^4$ per $\Omega M$. Good agreement between measured conductivity and classical theory (scattering by Coulomb collisions only) was found.

3. The current sheet collision developed an 18-fold increase in ion density that bounced back to launch magnetoacoustic waves back toward the drive coils. Just outside of the neutral line, at 80% of the coil radius, a strong density gradient developed due to differential arrival times that produced a large velocity early in the collision.

4. Acceleration by self-fields alone was inefficient in all of the devices studied. This was shown to be an unavoidable consequence of the low magnetic Reynolds number of the small scale accelerators of interest for electric propulsion.

5. Efficient acceleration was demonstrated for a configuration having orthogonal bias field and drive field coils.

6. Attempts to adapt a pulsed bias field to a coaxial accelerator geometry were not successful because of currents induced by the drive coils in the shield rings that were required to decouple the coaxial bias and drive coils.

7. Some new technique is needed to supply a strong bias magnetic field before high efficiency plasma acceleration can be achieved in a practical thruster.

## REFERENCES

1. C. R. Collett, "A 7700 Hour Endurance Test of a 30-cm Kaufman Thruster," AIAA Paper 75-366, March 1975.

2. H. J. King, et al, "Low Voltage 30-cm Ion thruster Development," NASA CR-134731, October 1974.

3. D. J. Connolly and R. J. Sovil, "Performance of Radiation-Cooled Magnetoplasmadynamic Arc Thrusters," NASA TM X-1908, October 1969.

4. R. H. Lovberg, Personal Communication.

5. D. Palumbo, Personal Communication.

6. R. Vondra, Personal Communication.

7. C. Lee Dailey, et al, "Pulsed Plasma Propulsion Technology," AFRPL-TR-73-81, July 1973.

8. C. L. Dailey and R. H. Lovberg, "Current Sheet Structure in an Inductive-Impulsive Plasma Accelerator," AIAA Journal, Vol. 10, No. 2, pp 125-129, February 1972.

9. H. E. Petschek, "Magnetic Field Annihilation," Proceedings AAS-NASA Symposium on Physics of Solar Flares, NASA p 50, 1965.

10. A. Bratenahl and C. M. Yeates, "Experimental Study of Magnetic Flux Transfer at the Hyperbolic Neutral Point," Phys. Fluids, Vol. 13, No. 11, pp 2696-2709, 1970.

11. H. R. Griem, Plasma Spectroscopy, McGraw-Hill, New York, San Francisco, Toronto and London, 1964, pp 145.

12. W. L. Wiese, M. W. Smith and B. M. Miles, "Atomic Transition Probabilities," Part II, Natn. Bur. Stand. (1969), pp 203.

13. W. L. Wiese, in Plasma Diagnostic Techniques, edited by R. H. Huddlestone and S. L. Leonard, Academic Press, New York, London, 1965, pp 302.

14. H. R. Griem, Phys. Rev. Lett., 10, pp 509, 1966.

15. L. Spitzer, "Physics of Fully Ionized Gases," Interscience, New York, London, 1962, pp 139.